UNIVERSITAT POLITÈCNICA DE CATALUNYA BARCELONATECH

Mathematical modelling of diffusion processes at the nanoscale

Helena Ribera Ponsa

Mathematical modelling of diffusion processes at the nanoscale

Helena Ribera Ponsa

Supervised by Prof. Dr. Tim Myers

Submitted in fullfillment of the requirements
for the degree of Doctor in Philosophy in Applied Mathematics
in the Facultat de Matemàtiques i Estadística
at the Universitat Politècnica de Catalunya.

December 2017, Barcelona, Spain.

Acknowledgments

First and foremost, I would like to thank my supervisor Tim Myers. He has always been keen on helping me, whether it had to do with work or otherwise. I cannot appreciate enough his expertise and patience with me. His sense of humour has always made me smile through this long adventure. I have become not only a better mathematician, but a better person as well. I feel very lucky to have been able to work alongside him for the past few years, and I sincerly hope that our paths keep on crossing in the next many years.

I would like to thank Brian Wetton for taking me in at the Institute of Applied Mathematics for three months. His enthusiasm never wore off and many new ideas came to life in just a short period of time thanks to that. He also gave me the opportunity to move to the other side of the world for a short while, which proved to be an amazing experience.

On a personal note, I would like to thank Vinnie, for being the best mate I could ever have hoped to find during my PhD journey. He has not only been the very best of friends, but he has always been keen on helping me with my work. Your kindness and sense of humour have made this journey a lot better. Honestly, thank you man.

I would also like to thank the people in the CRM. Claudia, por ser la mejor compañía que hubiese podido encontrar en el grupo y por hacer mi vida un poco mejor, tanto dentro como fuera del despacho. Grazie mille! Víctor, el meu company d'esquaix i l'altra meitat del millor grup de música de la història. Mil mercès per fer que els dies al CRM passesin de manera més entretinguda. Néstor, gràcies per totes les *risses* que he hem fet literalment des del primer dia que vas arribar. Gemma, merci per tots els quilòmetres que hem fet. Estic ja preparada per la propera cursa! Finalment, gràcies Marc per haver estat allà en tots els moments de crisi i pànic durant els últims dos anys.

També agraïr a tots els que porten amb mi tant de temps, i que durant aquests últims

tres anys han sigut una font de suport i distracció d'un valor incalculable. Gràcies Andrea, Eric, Ivan, Laura, Marc i Marc.

També agraïr als meus pares el seu suport incondicional, sense el qual no hagués arribat mai aquí.

Finally, I want to thank "la Caixa" Foundation for funding this PhD thesis.

Outline

The main body of this thesis is based on the research papers published since I started my PhD in October 2014. This thesis is split into two parts. Part I deals with the Stefan problem in various geometries and in different formulations. Part II is focussed on the Kirkendall effect. The papers listed below, from 1 to 4, correspond to the Chapters 3, 4, 6, 7 respectively. Chapter 1 is an introduction to those topics. Chapter 2 is a review on techniques to solve the Stefan problem. We also present the mathematical derivation of the Stefan problem. Chapter 5 presents a simplified one-phase reduction of the model presented in Chapter 4 and uses the techniques and results from 3 to solve it. Chapter 8 contains the conclusions.

1. H. Ribera, T. G. Myers. *Optimising the heat balance integral method in spherical and cylindrical Stefan problems.* Submitted to Heat and Mass Transfer, 2017. *Impact factor: 1.233.*

2. H. Ribera, T. G. Myers. *A mathematical model for nanoparticle melting with size-dependent latent heat and melt temperature.* Microfluidics and Nanofluidics 20(11):147, 2016. *Impact factor: 2.537.*

3. H. Ribera, B. Wetton, T. G. Myers. *Mathematical model for substitutional binary diffusion in solids.* Submitted to Applied Mathematical Modelling, December 2017. *Impact factor: 2.35.* Manuscript Reference number: APM-D-17-03147.

4. H. Ribera, B. Wetton, T. G. Myers. *Cellular automaton model and simulations for substitutional binary diffusion in solids.* Submitted to Journal of Cellular Automata, December 2017. *Impact factor: 0.698.*

Abstract

Nanoparticles have a wide variety of applications in fields such as biology, medicine, optics, or energy production. Many properties, and the function they carry out, depend on size and/or matter distribution within the particle. In this thesis we study diffusion processes during nanoparticle evolution and develop appropriate models with the aim of being able to optimise their functions according to the needs of industry. Two distinct diffusion processes are studied in detail throughout this thesis: phase change and atomic interdiffusion. To do this we employ various mathematical techniques. The list includes asymptotic analysis, the Heat Balance Integral Method (HBIM), the opTimal HBIM (TIM), similarity variables, separation of variables and numerical methods.

In Chapters 3, 4 and 5 we focus on the phase change problem, also termed the Stefan problem. In Chapter 3 we explore the application of the Heat Balance Integral Method to Stefan problems in spherical and cylindrical coordinates. Working with a reduced one-phase model, we use the standard version of this method and one designed to minimise the error. Furthermore, we define coordinate transformations with the aim of improving their accuracy. We compare the results obtained against numerical and perturbation solutions. It is shown that, whilst the results for the cylindrical problem are not excellent, for the spherical case it is possible to obtain highly accurate approximate solutions. In Chapter 4 we present a model for the melting of a spherical nanoparticle that differs from previous ones. This model includes the size dependence of the latent heat and a cooling condition at the boundary (as opposed to the fixed temperature condition used in previous studies). The latent heat variation is modelled by a new relation, which matches experimental data better than previous models. A novel form of Stefan condition is used to determine the position of the melt front. This condition takes into account the latent heat variation, the energy

required to create new surface and the kinetic energy of the displaced fluid layer. Other features that the model includes are melting point depression and density change in the different phases. A semi-implicit numerical scheme is developed to solve the problem. For large Stefan numbers it is compared against the perturbation solution. Agreement between the approximate and numerical solutions is excellent. Results show faster melting times than previous theoretical models, primarily due to latent heat variation. It is also shown that the previously used fixed temperature boundary condition led to faster melting rates at early times, however it also magnified the effect of kinetic energy, which subsequently slowed down the process. Chapter 5 links the previous two chapters; we use the optimal exponents found in Chapter 3 in the approximate solution for a simplified one-phase reduction of the model presented in Chapter 4. We study different outer boundary conditions, and then compare the solution given by the TIM with numerical and perturbation solutions for the same problem. Results indicate that the TIM is more accurate than the first order perturbation for all cases studied.

In Chapters 6 and 7 we shift our focus to binary diffusion in solids. In Chapter 6 we detail the mechanisms that drive substitutional binary diffusion via vacancy exchange, and derive appropriate governing equations. Our focus is on the one-dimensional case with insulated boundary conditions. We are able to make analytical progress by reducing the expressions for the concentration-dependent diffusion coefficients for different limiting cases related to the ratio of diffusion rates between species. After carrying out an asymptotic analysis of the problem, and obtaining analytical solutions, we compare them against a numerical solution. We find that these reductions are in excellent agreement in the limiting cases. Moreover, they are valid, within 10%, to the general solution. In Chapter 7 we develop a cellular automata (CA) model to study the problem presented in the previous chapter. Using a very simple state of change rule we are able to define an asynchronous CA model that shows excellent agreement when compared to the solution of the continuum model derived in Chapter 6. This is proven further by taking the continuum limit of the CA model presented and showing that the governing equations are the same as the ones rigorously derived before, for one of the limiting cases. This provides us with a new, simple method to study and model binary diffusion in solids. Further, since the computational expense of the CA model increases with the number of cells, this approach is best suited to

small materials samples such as nanoparticles.

The main body of the thesis, Chapters 3, 4, 6 and 7, correspond to papers submitted to research journals in 2017. Chapter 4 has already been published.

Resum

Les nanopartícules tenen un gran ventall d'aplicacions en diversos camps com la biologia, la medicina, l'òptica o la producció d'energia. Moltes propietats, així com la seva funcionalitat, depenen de la grandària i/o la distribució de matèria dins la partícula. En aquesta tesi estudiem processos de difusió relacionats amb l'evolució de nanopartícules i desenvolupem models amb l'objectiu d'optimitzar les seves funcions d'acord amb les necessitats de la indústria. Estudiarem en detall dos models ben distingits al llarg d'aquesta tesi: el canvi de fase i la interdifusió atòmica. Per fer-ho, utilitzarem diverses tècniques matemàtiques, tals com anàlisi asimptòtica, el Heat Balance Integral Method (HBIM), el opTimal HBIM (TIM), variables de similitud, separació de variables i mètodes numèrics.

En els Capítols 3, 4 i 5 ens centrem en el problema de canvi de fase, també anomenat el problema de Stefan. En el Capítol 3 explorem l'aplicació del Heat Balance Integral Method als problemes de Stefen en coordenades esfèriques i cilíndriques. Treballant amb un model reduït d'una fase, utilitzem la versió estàndard d'aquest mètode i una versió dissenyada per minimitzar l'error. A més a més, definim transformacions de coordenades amb l'objectiu de millorar la precisió. Comparem els resultats obtinguts amb solucions numèriques i de pertorbació. Mostrem que, mentre que els resultats pel problema cilíndric no són excel·lents, pel cas esfèric és possible obtenir solucions aproximades altament precises. En el Capítol 4 presentem un model diferent als anteriors per descriure la fusió d'una nanopartícula esfèrica. Aquest model inclou una definició de calor latent que depèn de la mida de la nanopartícula i una condició de refredament de Newton a la frontera (al contrari de la condició de temperatura fixa d'estudis anteriors). Modelem la variació de la calor latent amb una nova relació que coincideix amb dades experimentals millor que models anteriors. Utilitzem una nova condició de Stefan per determinar la posició de la interfície.

Aquesta condició té en compte la variació de la calor latent, l'energia necessària per a crear nova superfície i l'energia cinètica de la capa de líquid desplaçada. Altres característiques que inclou el model són la depressió del punt de fusió i canvi de la densitat en les diferents fases. Desenvolupem també un mètode numèric semi-implícit per solucionar el problema. Per nombres de Stefan grans, el comparem amb la solució de pertorbació. La concordància entre les solucions numèriques i aproximades és excel·lent. Els resultats mostren temps de fusió més ràpids que en models teòrics previs, principalment a causa de la variació de calor latent. També mostrem que la condició de temperatura fixa a la frontera resultava en temps de fusió més ràpids per temps inicials; tot i així magnificava l'efecte de l'energia cinètica que, conseqüentment, feia que el procés fos més lent. En el Capítol 5 enllacem els dos capítols anteriors; utilitzem els exponents òptims que hem trobat en el Capítol 3 per la solució aproximada al model reduït i d'una fase del Capítol 4. Estudiem dues condicions de frontera i comparem la solució del mètode TIM amb la solució numèrica i de pertorbació del mateix problema. Els resultats indiquen que el TIM és més precís que la pertorbació de primer order per tots els casos estudiats.

En els Capítols 6 i 7 canviem el focus del nostre estudi a la difusió binària en sòlids. En el Capítol 6 detallem els mecanismes que controlen la difusió binària mitjançant intercanvi de vacants, i posteriorment derivem les equacions que governen el model. El nostre focus és el cas unidimensional amb condicions de frontera d'aïllament. Hem sigut capaços de progressar analíticament reduïnt les expressions dels coeficients de difusió (que depenen de la concentració) per casos límits relacionats amb la ràtio dels índexs de difusió entre les dues espècies. Després d'obtenir solucions analítiques mitjançant una anàlisi asimptòtica del problema les comparem amb la solució numèrica. Les reduccions que hem fet al problema concorden de manera excel·lent en els casos límit. A més a més, són vàlides amb un marge d'error del 10% a la solució general del problema. En el Capítol 7 desenvolupem un model autòmat cel·lular (CA, en anglès) per estudiar el problema presentat en el capítol anterior. Utilitzant una norma de canvi d'estat molt simple som capaços de definir un model CA asíncron que mostra un acord excel·lent quan el comparem amb la solució del model continu derivat en el Capítol 6. Demostrem endemés aquest fet prenent el límit continu del model CA i observant que les equacions governants que resulten són les matexies que les que hem derivat prèviament de manera rigorosa per un dels casos límit. Amb això tenim un

mètode nou i simple per a estudiar difusió binària en sòlids. A més a més, com que el cost computacional del model CA incrementa amb el nombre de cel·les, aquest enfocament va millor per estudiar mostres de material petites, com poden ser les nanopartícules.

El cos principal de la tesi, Capítols 3, 4, 6 i 7, corresponen a articles enviats a revistes d'investigació durant el 2017. El Capítol 4 ja ha estat publicat.

Contents

List of Figures

List of Tables

1 | Introduction

The phase change problem is found in many natural and industrial processes, from lava solidification, sublimation of spacecraft heat shields, formation of dew, boiling water in a kettle, to ice-cream manufacture. The mathematical formulation to describe this type of phenomena is termed the Stefan problem, after the Austrian physicist Josef Stefan. Stefan developed the formulation with the aim of describing the solid-liquid phase change during ice formation in the Arctic seas [100].

A Stefan problem is a boundary value problem for a partial differential equation (PDE) in which the boundary position is dependent on time and must therefore be determined as part of the solution. For the specific case of a solid liquid change the mathematical formulation involves heat equations to describe the temperature in the solid and liquid phases and a condition at the solid-liquid interface that describes the position of the moving boundary, termed the Stefan condition. The first part of this thesis is devoted to the Stefan problem, with the primary aim of describing the melting process of spherical nanoparticles.

A range of solution methods have been used to solve the Stefan problem. Similarity transformations, where independent variables are grouped in such a way as to reduce the number of independent variables in a PDE system, lead to a variety of exact solutions of Stefan problems subject to various boundary conditions. However, only a very small number of these are of any practical use. Perhaps the most common approximate solution technique for solving Stefan problems is the perturbation method. This gives accurate solutions for large Stefan number β (the ratio of the latent heat to the specific heat times the change in temperature) and converges to the exact solution as $\beta \to \infty$. However, large β is not always physically realistic. In [3, Chap 2.1] a number of realistic examples of the phase change of water, copper, paraffin wax and silicon dioxide are provided which shows $\beta \in [2 \times 10^{-3}, 8.3]$.

They also state that for some families of non-metallic solids such as waxes β may be large but for metals typical values of β are of the order $0.1-1$. For silicates β may be very small. So clearly the limit of large β is not always of practical interest. Small β perturbation solutions exist but are significantly more complex to evaluate beyond the leading order. This motivates the use of the Heat Balance Integral Method (HBIM), [38]. This is an approximate solution method primarily applied to thermal and phase change problems. It has become popular largely due to its simplicity. For example, when solving a single heat equation the method permits the governing partial differential equation to be transformed to a first order ordinary differential equation, which may often be solved analytically.

The HBIM has been criticised for a lack of accuracy and also the *ad hoc* choice of an approximating function. This motivated the development of the opTimal Integral Method, or TIM. The TIM minimises the least-squares error between the approximation and the exact solution, so removing the arbitrary choice of approximating function and significantly reducing errors. In [64] it is shown that this form of improved HBIM is more accurate than the second order perturbation for practically useful values of β.

Numerical solutions are necessary in parameter regimes where the approximate solutions are invalid. They also provide an important check on the approximate solutions. In Chapter 2 we give more details on all of the above solution methods.

The prime motivation for this thesis is the study of diffusion and phase change at the nanoscale. An important part of this field involves spherical nanoparticles and nanowires. For this reason in Chapter 3 we extend the HBIM and the TIM to spherical and cylindrical geometries.

One of the main reasons why nanoparticles have been studied so widely is that they behave differently to their bulk counterparts, due to the large ratio of surface to volume atoms. Examples include enhanced mechanical strength, enhanced solar radiation absorption and superparamagnetism. In the context of melting it is well-known that the melt temperature and the latent heat decrease with decreasing particle size [13, 50]. Only one mathematical paper has addressed this issue [8]. Another issue that is typically neglected is the density jump between phases. This has been addressed in [31]. In these studies, and the vast majority of other mathematical papers, a fixed temperature boundary condition is imposed. In reality this is almost impossible to achieve. In the corresponding mathematical

model it leads to an initial infinite melt rate and when density difference is included, initial infinite kinetic energy, both of which are obviously unrealistic and lead to significant errors in the melt times. A more sensible condition is Newton cooling, in which the gradient of the temperature at the boundary is proportional to the difference between the temperature of the particle and that of the environment. In Chapter 4 we focus on solving the spherical Stefan problem for the melting of nanoparticles, and include all the features mentioned here, thus presenting a very realistic, novel model for melting at the nanoscale. In Chapter 5, we apply the TIM method developed in Chapter 3 to a simplified one-phase reduction of the model presented in Chapter 4.

For many applications involving nanoparticles the distribution of matter in the particle is key to their functionality. An important example are hollow nanoparticles [37]. The large fraction of void space in them allows drugs, cosmetics and DNA to be encapsulated and then released in a controlled manner. Other uses of the hollow space in particles has been to modulate the refractive index, lower the density, increase the active area for catalysis, and to expand the array of imaging markers suitable for early detection of cancer [55]. The synthesis of hollow nanoparticles is based on different physical phenomena such as galvanic replacement, Ostwald ripening, layer-by-layer assembly and the Kirkendall effect. The latter is the focus of the second part of this thesis.

The Kirkendall effect is the observed motion of the boundary layer between two metals due to the difference between the diffusion rates of the metal atoms. Its name comes from the American chemist and metallurgist Ernest Kirkendall. He and his student, Alice Smigelskas, designed an experiment to try to explain behaviour observed by Pfeil [82], who noted that small particles of foreign matter that fell on the surface of oxidising steel were buried until they disappeared. This seemed to indicate that the diffusion rate of iron and oxygen were different, which was against the common belief at the time. Kirkendall and Smigelskas' experiment was published in a paper in 1947 [99] and not only did it prove that different atomic species have different diffusion rates, but also that diffusion occurred via vacancy exchange (Figure 1.1(c)) instead of via substitutional or ring mechanisms (Figure 1.1(a), (b)).

In principle, crystalline solids should have a perfect crystal structure. However, the arrangement of atoms in these materials is not perfect, so the regular patterns are interrupted

by crystallographic defects; a particular type are point defects, which means that they only occur at a single lattice point. Vacancy defects are one case of point defects. They are lattice sites that should be occupied in a perfect crystal but for some reason are not. Kirkendall's experiment proved that these empty spaces are necessary to allow diffusion within the crystal lattice. An atom neighbouring a vacancy site can exchange its position with the vacancy, thus making the empty lattice space move as well.

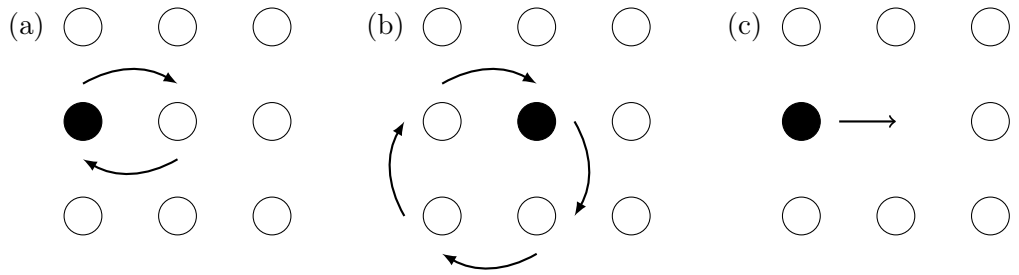

Figure 1.1: Different diffusion mechanisms. (a) Direct exchange mechanism; (b) Ring mechanism; (c) Vacancy mechanism.

Kirkendall's experiment [99] had the following set up. A bar of brass (30% copper and 70% zinc) was covered with molybdenum (Mo) wires on its top and bottom surface and later electroplated with pure copper. Then, enough heat to permit atomic diffusion was applied to the block at different times. They studied the position of the Mo wires, and were able to observe that they had moved towards the center of the block. See Figure 1.2. If the diffusion rate of both copper and zinc were the same, the amount of copper transferred from the copper part towards the brass part and the amount of zinc transferred from the brass part to the copper one should be the same, so the Mo wires should not move from their original position. Since the wires moved towards the brass they concluded that zinc has a faster diffusion rate than copper. To compensate this difference in diffusion rates, the interface of brass/copper shifts, which results in a net vacancy flow and can lead to an accumulation of vacancy sites, creating voids during solid binary diffusion. This is important because in metals, it can result in deterioration of their mechanical, thermal and electrical properties.

The first example of using the Kirkendall effect to create hollow structures was by Aldinger [2]. Starting with spherical beryllium particles of average radius 33.5 μm he was

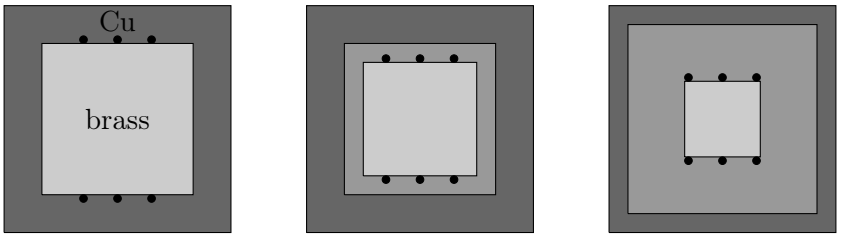

Figure 1.2: Sketch of the original experiment by Kirkendall and Smigelskas.

able to produce hollow beryllium-nickel and beryllium-cobalt particles which would increase their volume from 8% to 262% times their original one. Hollow nanocrystals were first created by Yin *et al.* [115]. They started with cobalt nanocrystals, which upon reaction in solution with oxygen and either sulfur or selenium led to the formation of hollow nanocrystals that had a central void of 40-70% the size of the initial particle. Their process was based on the dominant outer diffusion of Co, which generated a single void in each nanoparticle. Gao *et al.* [33] were able to create hollow nanowires with a unique morphology (interconnected hollow nanocrystals) via what they call a *magnetic guiding* strategy. Gonzalez *et al.* [37] were able to synthesise different shapes of nanostructures such as spheres, cubes and tubes at room temperature. Their process started with galvanic replacement, which created a structure with an Ag layer sandwiched between two Au layers. After this they used the Kirkendall effect to create cavities that coalesced into the one created by galvanic replacement.

In Chapter 6 we rigorously derive a mathematical model for binary interdiffusion. We use the model in a test-case, a one-dimensional insulated bar, in order to understand the physical parameters that affect the Kirkendall effect and the movement of vacancy sites. Some particular cases are studied in order to provide analytical progress to the field. In Chapter 7 we develop a cellular automaton model to describe the phenomenon. We present a particular set of rules that lead to a continuum model that agrees with the mathematical formulation presented in the previous chapter.

All equations presented in this thesis are based on the validity of the continuum assumption. This has been discussed in detail in [30, 71]. For phase change the limit of validity appears to be around 2-5 nm, depending on the material.

Chapters 3, 4, 6 and 7 of this thesis have already been submitted as journal papers;

Chapter 4 was published in 2016. These papers all include a detailed introduction and bibliography. For this reason a comprehensive review has not been provided in this chapter, instead we move straight on to a description of the Stefan problem and standard solution techniques.

Part I

The Stefan Problem

2 | Formulation and techniques for the Stefan problem

To illustrate the Stefan problem we now consider the classic example of the melting of a one-dimensional bar. Consider a semi-finite solid occupying $x \geq 0$. The phase change is driven by a fixed temperature heat source at the boundary $x = 0$. At the moving boundary, that is, the melt front, the temperature is set to be that of melting, denoted by T_m^*. See Figure 2.1 for a sketch of the situation. The governing equations are

$$c_l \rho_l \frac{\partial T}{\partial t} = k_l \frac{\partial^2 T}{\partial x^2}, \qquad 0 < x < s(t), \tag{2.1}$$

$$c_s \rho_s \frac{\partial \theta}{\partial t} = k_s \frac{\partial^2 \theta}{\partial x^2}, \qquad s(t) < x < \infty, \tag{2.2}$$

where T and θ denote the temperatures of the liquid and solid, respectively, $s(t)$ is the position of the moving boundary, and ρ_i, c_i and k_i are the densities, specific heats and conductivities, respectively. The index notation $i = s$, l refers to the solid or liquid phases, respectively. The energy balance (Stefan condition) at the boundary is given by

$$\rho_l L_m^* \frac{\mathrm{d}s}{\mathrm{d}t} = \left.\frac{\partial \theta}{\partial x}\right|_{x=s(t)} - \left.\frac{\partial T}{\partial x}\right|_{x=s(t)}, \tag{2.3}$$

where L_m^* denotes the latent heat. Finally, the boundary conditions may be written as

$$T(s(t), t) = \theta(s(t), t) = T_m^*, \tag{2.4}$$

$$T(0, t) = T_H, \tag{2.5}$$

$$\theta\big|_{x \to \infty} = T_H, \tag{2.6}$$

where $T_H > T_m^*$ is the temperature at the boundary that drives the melting process. At the initial time $t = 0$ the liquid phase does not exist and so $s(0) = 0$. Despite criticising

the boundary condition (2.5) in the introduction we apply it here since it permits an exact solution against which we can verify the approximate and numerical solutions. Also because it is the standard entry point into the study of Stefan problems.

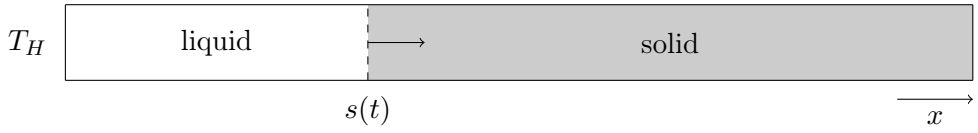

Figure 2.1: Sketch of the one-dimensional Stefan problem.

A standard simplification of the problem defined by (2.1)-(2.5) consists in assuming that one of the phases is at the melt temperature T_m^*, thus reducing the problem to a single heat equation. Since we omit one of the phases, this simplification is known as the one-phase Stefan problem. It may be written as

$$c_l\rho_l\frac{\partial T}{\partial t} = k_l\frac{\partial^2 T}{\partial x^2}, \qquad 0 < x < s(t), \tag{2.7}$$

$$\rho_l L_m\frac{\mathrm{d}s}{\mathrm{d}t} = -k_l\frac{\partial T}{\partial x}\bigg|_{x=s(t)}, \tag{2.8}$$

$$T(s(t),t) = T_m^*, \qquad T(0,t) = T_H, \qquad s(0) = 0. \tag{2.9}$$

This problem may also be solved exactly.

Many analytical and numerical approximate methods have been used to solve the Stefan problem when no exact analytical solution can be found [40]. In the following sections we will describe some of these methods and compare with the exact solutions when possible. The methods will then be extended to the different problems presented throughout the thesis.

We now define appropriate nondimensional variables in order to simplify and generalise the problem. This will also help identify large or small parameters that might be useful for the solution techniques. The standard scaling is

$$\hat{T} = \frac{T - T_m^*}{\Delta T}, \qquad \hat{t} = \frac{k_l}{c_l\rho_l L^2}t, \qquad \hat{x} = \frac{x}{L}, \qquad \hat{s} = \frac{s}{L}, \tag{2.10}$$

where $\Delta T = T_H - T_m^*$ and L is unknown. The one-dimensional, one-phase Stefan problem becomes (dropping the hat notation)

$$\frac{\partial T}{\partial t} = \frac{\partial^2 T}{\partial x^2}, \qquad 0 < x < s(t), \tag{2.11}$$

$$\beta \frac{\mathrm{d}s}{\mathrm{d}t} = -\left.\frac{\partial T}{\partial x}\right|_{x=s(t)}, \tag{2.12}$$

$$T(s(t),t) = 0, \qquad T(0,t) = 1, \tag{2.13}$$

where $\beta = L_m^*/(c_l \Delta T)$ is the Stefan number. Note, the Stefan number is often also written as $c_l \Delta T / L_m^*$. Here we follow the definition of [32] where $\beta = L_m^*/(c_l \Delta T)$ is the coefficient of the melting rate since this seems a more physically intuitive definition.

2.1 Solution techniques

In this section we will describe some of the most common solution techniques used to solve the classical Stefan problem. When possible, they will be used in later sections to solve different versions of the phase change problem.

2.1.1 Similarity variables

Similarity transformations are a powerful technique to solve partial differential equations. The key step is to introduce what is referred to as a similarity variable, which, if chosen appropriately, reduces the order of the PDE. For our problem (2.11)-(2.13) we define the standard diffusion similarity variable $\xi = x/\sqrt{t}$, and consider $F(\xi) = T(x,t)$. We have

$$\frac{\partial T}{\partial t} = \frac{\partial \xi}{\partial t}\frac{\mathrm{d}F}{\mathrm{d}\xi} = -\frac{1}{2}\frac{x}{t^{3/2}}F', \qquad \frac{\partial^2 T}{\partial x^2} = \left(\frac{\partial \xi}{\partial x}\right)^2 \frac{\mathrm{d}^2 F}{\mathrm{d}\xi^2} = \frac{1}{t}F'', \tag{2.14}$$

which upon substituting into (2.11), gives

$$\frac{\mathrm{d}^2 F}{\mathrm{d}\xi^2} = -\frac{\xi}{2}\frac{\mathrm{d}F}{\mathrm{d}\xi}. \tag{2.15}$$

This has solution

$$F(\xi) = C_1 + C_2 \mathrm{erf}\left(\frac{\xi}{2}\right). \tag{2.16}$$

Applying boundary conditions (2.13) leads to

$$C_1 = 1, \qquad C_2 = -\frac{1}{\mathrm{erf}\left(\frac{s(t)}{2\sqrt{t}}\right)}. \tag{2.17}$$

For C_2 to be constant requires

$$s(t) = 2\lambda\sqrt{t}, \tag{2.18}$$

for some constant λ.

The Stefan condition is

$$\beta \frac{\mathrm{d}s}{\mathrm{d}t} = -\frac{\partial T}{\partial x}\bigg|_{x=s} = -\frac{1}{\sqrt{t}} \frac{\mathrm{d}F}{\mathrm{d}\xi}\bigg|_{\xi=s/(2\sqrt{t})}. \tag{2.19}$$

Substituting for $s = 2\lambda\sqrt{t}$ leads to a transcendental equation to determine λ

$$\beta\sqrt{\pi}\lambda e^{\lambda^2}\mathrm{erf}(\lambda) = 1. \tag{2.20}$$

Thus, we have fully defined the solution to the problem,

$$T(x,t) = 1 - \frac{\mathrm{erf}\left(\frac{\xi}{2}\right)}{\mathrm{erf}\left(\frac{s(t)}{2\sqrt{t}}\right)}, \qquad s = 2\lambda\sqrt{t}, \tag{2.21}$$

where λ satisfies (2.20). This is termed the Neumann solution

2.1.2 Perturbation solution

Perturbation theory is used in problems that involve a small parameter $\epsilon \ll 1$ to find approximate analytical solutions. A perturbation solution consists of a power series in ϵ. In the problem defined by equations (2.11)-(2.13), when $\beta \gg 1$, we can define a parameter $\epsilon = 1/\beta \ll 1$. The large β limit corresponds to slow melting (when compared to heat transfer) and so, to observe the evolution of the melting front it is standard to rescale time such that $\tau = t/\beta = \epsilon t$. The governing equation then becomes

$$\epsilon \frac{\partial T}{\partial \tau} = \frac{\partial^2 T}{\partial x^2}, \qquad 0 < x < s(\tau). \tag{2.22}$$

The Stefan condition is

$$\frac{\mathrm{d}s}{\mathrm{d}\tau} = -\frac{\partial T}{\partial x}\bigg|_{x=s(\tau)}. \tag{2.23}$$

We now look for a solution for the liquid temperature $T = T_0 + \epsilon T_1 + \epsilon^2 T_2 + \cdots$. Upon substituting into equation (2.22) we get

$$\epsilon \frac{\partial T_0}{\partial \tau} + \epsilon^2 \frac{\partial T_1}{\partial \tau} + \cdots = \frac{\partial^2 T_0}{\partial x^2} + \epsilon \frac{\partial^2 T_1}{\partial x^2} \cdots, \tag{2.24}$$

with boundary conditions

$$T_0(0,\tau) + \epsilon T_1(0,\tau) + \cdots = 1, \qquad T_0(s,\tau) + \epsilon T_1(s,\tau) + \cdots = 0. \tag{2.25}$$

To first order in ϵ Stefan condition is

$$\frac{\mathrm{d}s}{\mathrm{d}\tau} = -\frac{\partial T_0}{\partial x}\bigg|_{x=s(\tau)} - \epsilon \frac{\partial T_1}{\partial x}\bigg|_{x=s(\tau)}. \tag{2.26}$$

Note, we could also expand s in terms of ϵ. However this involves extra calculations without any increase in accuracy.

Equation (2.24) yields the following system at different orders of ϵ

$$\mathcal{O}(\epsilon^0): \qquad 0 = \frac{\partial^2 T_0}{\partial x^2}, \tag{2.27}$$

$$\mathcal{O}(\epsilon^1): \qquad \frac{\partial T_0}{\partial \tau} = \frac{\partial^2 T_1}{\partial x^2}, \tag{2.28}$$

$$\mathcal{O}(\epsilon^2): \qquad \frac{\partial T_1}{\partial \tau} = \frac{\partial^2 T_2}{\partial x^2}, \tag{2.29}$$

$$\vdots$$

The boundary conditions (2.25) give

$$T_0(0,\tau) = 1, \qquad T_0(s,\tau) = 0, \tag{2.30}$$

$$T_n(0,\tau) = 0, \qquad T_n(s,\tau) = 0, \qquad \text{for all } n \geq 1. \tag{2.31}$$

Applying the boundary conditions above leads to

$$T_0 = 1 - \frac{x}{s}, \qquad T_1 = \frac{1}{6}\left(\frac{x^3}{s^2} - x\right)\frac{\mathrm{d}s}{\mathrm{d}\tau}, \qquad \ldots \tag{2.32}$$

Substituting the approximate solution T to first order into the Stefan condition (2.26), we find that

$$\frac{\mathrm{d}s}{\mathrm{d}\tau} = -\left(-\frac{1}{s} + \epsilon \frac{1}{3}\frac{\mathrm{d}s}{\mathrm{d}\tau}\right), \tag{2.33}$$

which leads to

$$s(\tau) = \sqrt{\frac{6\tau}{3+\epsilon}} = \sqrt{2\tau}\left(1 - \frac{\epsilon}{6} + \cdots\right). \tag{2.34}$$

To continue the series is not straightforward since the second order version of (2.33) involves $s_{\tau\tau}$ and so a further initial condition is needed. This may be avoided using a boundary fixing transformation at the start of the analysis [18, 62].

2.1.3 Heat Balance Integral Method (HBIM)

The Heat Balance Integral Method (HBIM) is an approximation technique for solving thermal problems [38]. There are three key steps in using this method:

1. definition of the heat penetration depth $\delta(t)$, such that when $x > \delta(t)$ the temperature rise above the initial value is negligible;

2. specify an approximating function for the temperature, most commonly a quadratic, and apply boundary conditions to determine all unknown coefficients in terms of the unknown penetration depth;

3. integration of the governing equation over the corresponding domain to obtain the *heat balance integral*, which usually yields an ordinary differential equation for δ.

Consider the problem defined by equations (2.11)-(2.13). We extend the method described above to deal with the one-phase Stefan problem. The temperature in the domain $x \in [0,\, s(t)]$ is assumed to take on a quadratic form

$$T(x,t) = a_0 + a_1\left(1 - \frac{x}{s}\right) + a_2\left(1 - \frac{x}{s}\right)^2. \tag{2.35}$$

Applying both boundary conditions leads to $a_0 = 0$ and $a_2 = 1 - a_1$ and so

$$T(x,t) = a_1\left(1 - \frac{x}{s}\right) + (1 - a_1)\left(1 - \frac{x}{s}\right)^2. \tag{2.36}$$

The Stefan condition (2.12) gives

$$\beta\frac{\mathrm{d}s}{\mathrm{d}t} = -\left.\frac{\partial T}{\partial x}\right|_{x=s} = \frac{a_1}{s}, \tag{2.37}$$

hence we may define $a_1 = \beta s s_t$. We now integrate the heat equation (2.11) over $x \in [0, s(t)]$,

$$\int_0^{s(t)} \frac{\partial T}{\partial t}\,\mathrm{d}x = \frac{\mathrm{d}}{\mathrm{d}t}\int_0^{s(t)} T(x,t)\,\mathrm{d}x = \int_0^{s(t)} \frac{\partial^2 T}{\partial x^2}\,\mathrm{d}x = \left.\frac{\partial T}{\partial x}\right|_{x=s} - \left.\frac{\partial T}{\partial x}\right|_{x=0}, \tag{2.38}$$

where the first equality comes from applying Leibniz theorem and $T(s,t) = 0$. Now,

$$\int_0^{s(t)} T(x,t)\,\mathrm{d}x = \left[a_1\left(x - \frac{x^2}{2s}\right) - \frac{s}{3}(1 - a_1)\left(1 - \frac{x}{s}\right)^3\right]_{x=0}^{x=s} = \left(\frac{a_1}{2} + \frac{1 - a_1}{3}\right)s. \tag{2.39}$$

Assuming a_1 is constant (we will verify this later) and taking the derivative with respect to time, we obtain

$$\frac{\mathrm{d}}{\mathrm{d}t}\int_0^{s(t)} T(x,t)\,\mathrm{d}x = \left(\frac{a_1}{2} + \frac{1 - a_1}{3}\right)\frac{\mathrm{d}s}{\mathrm{d}t}. \tag{2.40}$$

On the other hand, we see trivially via (2.35) that

$$\left.\frac{\partial T}{\partial x}\right|_{x=s} - \left.\frac{\partial T}{\partial x}\right|_{x=0} = \frac{2(1 - a_1)}{s}. \tag{2.41}$$

Equating equations (2.40) and (2.41) yields

$$\frac{2+a_1}{6}\frac{\mathrm{d}s}{\mathrm{d}t} = \frac{2(1-a_1)}{s}. \tag{2.42}$$

Upon substituting in the equation above $a_1 = \beta s s_t$ we obtain

$$s\frac{\mathrm{d}s}{\mathrm{d}t} = \frac{1}{\beta}\left(-(1+6\beta) \pm \sqrt{1+24\beta+36\beta}\right). \tag{2.43}$$

Since $s(t) > 0$ we require the positive solution. Using the initial condition $s(0) = 0$, we find that

$$s(t) = \sqrt{\frac{\left(-2(1+6\beta) + \sqrt{24\beta+1+36\beta^2}\right)t}{\beta}}, \tag{2.44}$$

Note, since $s \propto \sqrt{t}$, as stated earlier $a_1 = \beta s s_t$ is constant. The solution is now complete, the temperature is specified by equation (2.36) and $s(t)$ by (2.44).

The accuracy of the standard HBIM method as presented has been questioned [73]. The greatest drawback with the method is the choice of the approximating function, and the key question is *what is the best choice for n?* where n is the order of the approximating polynomial. In many published works either an exact or a numerical solution is known, and n is chosen to match those solutions, which leads to the question as to why look for an approximate solution when you already have an exact one. The opTimal Integral Method (TIM) was developed to address these issues. This method provides a measure of the error without knowledge of an exact solution, and it significantly improves accuracy, for certain boundary conditions by orders of magnitude [69, 73].

2.1.4 The opTimal Integral Method (TIM)

The TIM introduces an unknown constant exponent into the polynomial approximation (2.35) and so the temperature is now taken as

$$T(x,t) = b_0 + b_1\left(1-\frac{x}{s}\right) + b_2\left(1-\frac{x}{s}\right)^n. \tag{2.45}$$

The boundary conditions lead to $b_0 = 0$ and $b_2 = 1 - b_1$ as before. The key of this method is that n is chosen to minimise a least squares error defined as [69]

$$E_n(n,t) = \int_0^{s(t)} \left(\frac{\partial T}{\partial t} - \frac{\partial^2 T}{\partial x^2}\right)^2 \mathrm{d}x. \tag{2.46}$$

If T is an exact solution, $E_n = 0$, otherwise we expect $E_n > 0$. This method allows us to quantify the accuracy without knowledge of the exact solution.

Similar to the standard HBIM the Stefan condition (2.13) yields $b_1 = \beta s s_t$, and so provided that b_1 is constant,

$$s(t) = \sqrt{\frac{2b_1 t}{\beta}}. \tag{2.47}$$

Since $t \geq 0$ and $\beta > 0$, we require that $b_1 > 0$ to ensure $s \geq 0$. Via the heat balance integral (2.38), we obtain

$$\frac{b_1(2 + (n-1)b_1)}{2(n+1)\beta} = n(1 - b_1), \tag{2.48}$$

which gives a quadratic equation to determine b_1 as a function of n and β. Substituting the temperature profile (2.45) into the error function (2.46) we obtain

$$\begin{aligned} E_n(n,t) = &\frac{b_1^2 s_t^2}{3s} + \frac{n(1-b_1)^2 s_t^2}{(4n^2-1)s} + \frac{4b_1(1-b_1)s_t}{(n+1)(n+2)s} + \frac{n^2(n-1)^2(1-b_1)^2}{(2n-3)s^3} \\ &- \frac{n^2(1-b_1)^2 s_t}{(2n-1)s^2} - \frac{2b_1(1-b_1)s_t}{s^2}. \end{aligned} \tag{2.49}$$

The denominators in the above expression indicate infinite error for $n = 1/2$, 1, $3/2$, so we will neglect these values. Substituting for $s \propto \sqrt{t}$ and $s_t \propto 1/\sqrt{t}$ it becomes clear that $E_n = e_n t^{-3/2}$, and the minimum value of e_n depends only on n and β. This dependence of E_n indicates that the error decreases as time increases, so the method is expected to be more accurate in later times. In Figure 2.2 we show the curve for e_n for different β. From the graph (Figure 2.2) we see that the optimal n, i.e., the one that minimises e_n, varies slowly with β. For large β the value of n tends to a constant. Here the graph indicates $n \simeq 1.77$ for $\beta = 5$, 10. For smaller n it is slightly higher. For practical purposes we could simply set $n = 1.78$ for all β. This value is obviously close to $n = 2$. This may partially explain the success of the HBIM. The most common problem takes an n value close to the optimal, so yielding accurate results. However this is not the case when different boundary conditions are applied and then n is significantly different to 2, see [73].

2.1.5 Numerical methods

Moving boundary problems can be difficult to deal with numerically, so it is usually useful to immobilise the boundary. In the problem defined by (2.11)-(2.13) the transformation

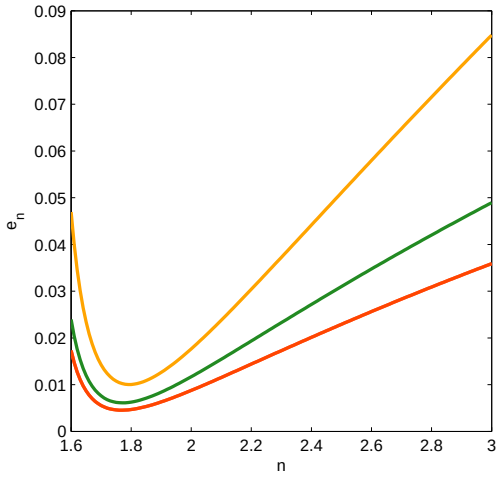

Figure 2.2: e_n for $\beta = 1,\ 5,\ 10$ (yellow, green and orange, respectively).

$\eta = x/s(t)$ fixes the boundary while the governing equations become

$$s^2\frac{\partial T}{\partial t} = \eta s\frac{\mathrm{d}s}{\mathrm{d}t}\frac{\partial T}{\partial \eta} + \frac{\partial^2 T}{\partial \eta^2}, \qquad 0 < x < 1, \tag{2.50}$$

$$\beta\frac{\mathrm{d}s}{\mathrm{d}t} = -\frac{1}{s}\frac{\partial T}{\partial \eta}\bigg|_{\eta=1}, \tag{2.51}$$

$$T(1,t) = 0, \qquad T(0,t) = 1. \tag{2.52}$$

To obtain a numerical solution there are still a few more steps to be carried out. First of all, we discretise the domain into I equally spaced points of length $\Delta\eta$, and time into N equally spaced points of length Δt. In Figure 2.3 we choose $\Delta\eta = 0.01$ and $\Delta t = 0.0005$. Now we discretise the derivatives in equation (2.51) such as

$$\frac{\partial T}{\partial t} = \frac{T_i^{n+1} - T_i^n}{\Delta t}, \qquad \frac{\partial T}{\partial \eta} = \frac{T_{i+1}^{n+1} - T_{i-1}^{n+1}}{2\Delta\eta}, \qquad \frac{\partial^2 T}{\partial \eta^2} = \frac{T_{i+1}^{n+1} - 2T_i^{n+1} + T_{i-1}^{n+1}}{\Delta\eta^2}, \tag{2.53}$$

where the i subscript denotes the i-th space-point, and the n superscript denotes the n-th time-point. Substituting these discretisations into equation (2.51) we obtain

$$-(s^n)^2 T_i^n = \nu\eta_i(s_t)^n\left(T_{i+1}^{n+1} - T_{i-1}^{n+1}\right) + \delta\left(T_{i+1}^{n+1} - 2T_i^{n+1} + T_{i-1}^{n+1}\right) - (s^n)^2 T_i^{n+1}, \tag{2.54}$$

where $\nu = \Delta t/(2\Delta\eta)$ and $\delta = \Delta t/(\Delta\eta^2)$. We can rewrite the equation above as

$$a_i^n T_{i-1}^{n+1} + b^n T_i^{n+1} + c_i^n T_{i+1}^{n+1} = d^n T_i^n, \tag{2.55}$$

where

$$a_i^n = -\nu\eta_i(s_t)^n + \delta, \qquad b^n = -2\delta - (s^n)^2, \tag{2.56}$$

$$c_i^n = \nu\eta_i(s_t)^n + \delta, \qquad d_i^n = -(s^n)^2 T_i^n. \tag{2.57}$$

Boundary conditions (2.52) lead to $T_I^n = 0$ and $T_1^n = 1$, respectively, for $n = 1, \ldots, N$. This allows us to write the following system,

$$\begin{pmatrix} 1 & 0 & 0 & 0 & \cdots & 0 & 0 & 0 & 0 \\ a_2^n & b^n & c_2^n & 0 & \cdots & 0 & 0 & 0 & 0 \\ 0 & a_3^n & b^n & c_3^n & \cdots & 0 & 0 & 0 & 0 \\ \vdots & \vdots & \vdots & \vdots & \cdots & \vdots & \vdots & \vdots & \vdots \\ 0 & 0 & 0 & 0 & \cdots & a_{I-2}^n & b^n & c_{I-2}^n & 0 \\ 0 & 0 & 0 & 0 & \cdots & 0 & a_{I-1}^n & b^n & c_{I-1}^n \\ 0 & 0 & 0 & 0 & \cdots & 0 & 0 & 0 & 1 \end{pmatrix} \begin{pmatrix} T_1^{n+1} \\ T_2^{n+1} \\ T_3^{n+1} \\ \vdots \\ T_{I-2}^{n+1} \\ T_{I-1}^{n+1} \\ T_I^{n+1} \end{pmatrix} = \begin{pmatrix} 1 \\ d_2^n \\ d_3^n \\ \vdots \\ d_{I-2}^n \\ d_{I-1}^n \\ 0 \end{pmatrix}.$$

This system is solved at every time step $n = 1, \ldots, N-1$. The Stefan condition (2.51) may be discretised as follows

$$\beta\frac{s^{n+1} - s^n}{\Delta t} = -\frac{1}{s^n}\frac{3T_I^{n+1} - 4T_{I-1}^{n+1} + T_{I-2}^{n+1}}{2\Delta\eta}. \tag{2.58}$$

Trivially,

$$s^{n+1} = -\frac{\nu}{\beta s^n}\left(3T_I^{n+1} - 4T_{I-1}^{n+1} + T_{I-2}^{n+1}\right) + s^n, \tag{2.59}$$

which allows us to find the position of the melt front at every time step $n = 1, \ldots, N-1$.

We still need an initial condition for T_i^1, which is often an issue in numerical solutions because the liquid phase does not exist at $t = 0$. We know from the exact solution (2.18) that $s = 2\lambda t^{1/2}$. Upon substituting this expression into (2.50)

$$t\frac{\partial T}{\partial t} = 2\eta\lambda^2\frac{\partial T}{\partial \eta} + \frac{\partial^2 T}{\partial \eta^2}. \tag{2.60}$$

This indicates that in the limit $t \to 0$ the governing equation tends to

$$2\eta\lambda^2\frac{\partial T}{\partial \eta} + \frac{\partial^2 T}{\partial \eta^2} = 0. \tag{2.61}$$

Applying boundary conditions (2.52) yields $T(\eta, t) = 1 - \frac{\operatorname{erf}(\lambda\eta)}{\operatorname{erf}(\lambda)}$, for $t \ll 1$ and λ given by equation (2.20). Hence as an initial condition we may take $T_i^1 = 1 - \frac{\operatorname{erf}(\lambda\eta_i)}{\operatorname{erf}(\lambda)}$. We now have the numerical solution fully defined.

In Figure 2.3 we show the results for the one-phase, one-dimensional problem given by equations (2.11)-(2.13) using all the solution techniques presented throughout this section. Figure 2.3(a) shows the results for the case $\beta = 1$. In general all solutions show excellent agreement although differences become more obvious as t increases. The numerical solution is indistinguishable from the exact solution at this scale. At $t = 10$, the perturbation solution has an error of 0.0124%; the HBIM, 0.0265%; the TIM ($n = 1.79$), 0.0148%; the numerical solution, 5.01×10^{-5}%. Figure 2.3(b) shows the results for the case $\beta = 5$. Now the agreement is better in all cases. At $t = 10$, the perturbation solution has an error of 7.76×10^{-4}%; the HBIM, 0.0075%; the TIM ($n = 1.77$), 0.0044%; the numerical solution, 4.83×10^{-5}%.

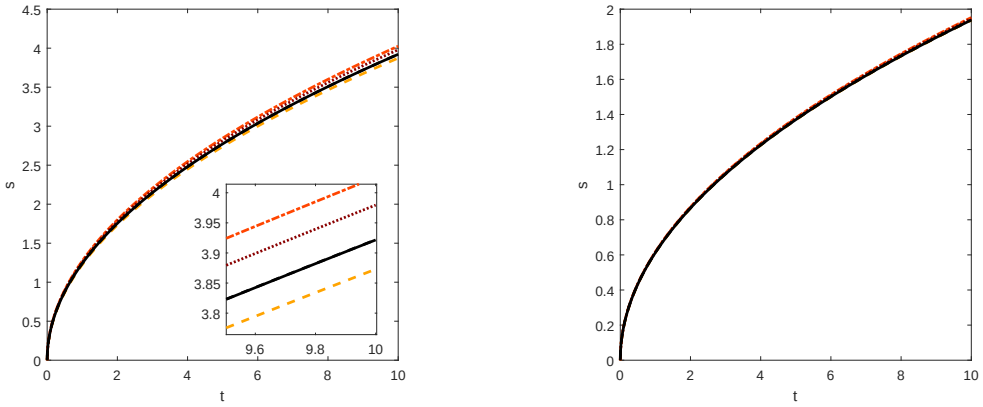

(a) $\beta = 1$. **(b)** $\beta = 5$.

Figure 2.3: Different solutions for the one-phase, one-dimensional Stefan problem. Exact solution (black, solid), perturbation to first order (yellow, dashed), HBIM (orange, dash-dotted), TIM (maroon, dotted), numerical (black, dashed) which is indistinguishable from the exact solution.

2.2 Spherical melting

The Stefan problem at the nanoscale has been studied extensively, its importance relying on the fact that nanoparticles are used in a wide variety of applications involving high temperatures, such as in medicine, in drug and gene delivery [36, 85] or targeting [35]; in optics [1]; in biology, in fluorescent biological labels [12], in the separation and purification of biological molecules and cells [65]; in energy production and storage [17]; in the creation of

materials with modified properties [23, 39]. Understanding this process can help us explain how they behave in their associated applications. In the subsequent chapters we consider spherical melting and so now discuss the appropriate problem formulation.

Standard assumptions when working with the Stefan problem include constant melt temperature, constant latent heat, constant solid-liquid surface tension, and constant and equal densities in both liquid and solid phases, see [3, 21, 40]. The standard formulation is

$$\rho_l c_l \frac{\partial T}{\partial t} = k_l \frac{1}{r^2}\frac{\partial}{\partial r}\left(r^2 \frac{\partial T}{\partial r}\right), \qquad R(t) < r < R_0, \tag{2.62}$$

$$\rho_s c_s \frac{\partial \theta}{\partial t} = k_s \frac{1}{r^2}\frac{\partial}{\partial r}\left(r^2 \frac{\partial \theta}{\partial r}\right), \qquad 0 < r < R(t), \tag{2.63}$$

where T is the temperature of the liquid, θ is the temeprature of the solid, ρ_i, k_i, c_i denote the density, the thermal conductivity and the heat capacity, respectively. Subscript $i = s,\, l$ indicate solid or liquid, respectively. Finally, R_0 denotes the initial particle radius and $R(t)$ is the interface between solid and liquid. Standard boundary conditions are

$$T(R_0, t) = T_H, \quad T(R, t) = \theta(R, t) = T_m^*, \quad \theta_r(0, t) = 0. \tag{2.64}$$

The Stefan condition balances energy conducted through the phases with that released by the phase change

$$\rho_s L_m^* \frac{\mathrm{d}R}{\mathrm{d}t} = k_s \left.\frac{\partial \theta}{\partial r}\right|_{r=R} - k_l \left.\frac{\partial T}{\partial r}\right|_{r=R}, \tag{2.65}$$

where L_m^* is the bulk latent heat.

This formulation has proved effective at studying macroscale Stefan problems, however, at the nanoscale various assumptions involved in its derivation become invalid. In the following section we will discuss a number of necessary modifications.

2.2.1 Extensions to this formulation

We will now provide general expressions that lead to the equations for the standard problem (2.62)-(2.65), but that will be a helpful tool to extend the formulation into more appropriate models. To simplify the analysis, a number of assumptions will be made: gravity and viscous effects are negligible; spherical symmetry is imposed; each phase is incompressible. Bird, Stewart and Lightfoot [10] write down a simplified energy balance,

$$\frac{\partial}{\partial t}\left[\rho\left(I + \frac{v^2}{2}\right)\right] = -\nabla \cdot \left[\rho \mathbf{v}\left(I + \frac{v^2}{2}\right) + \mathbf{q} + P\mathbf{v}\right], \tag{2.66}$$

where ρ is the density, I the internal energy per unit mass, $\mathbf{v}$ the velocity, $v = |\mathbf{v}|$, the conductive heat flux $\mathbf{q} = -k\nabla T$, and P is the pressure. This states that the gain of energy per unit volume depends on energy flow by convection and conduction, and the rate of work done by pressure. Under the same assumptions, conservation of mechanical energy is given by

$$\frac{\partial}{\partial t}\left(\frac{\rho v^2}{2}\right) + \nabla \cdot \left(\frac{\rho v^2 \mathbf{v}}{2} + P\mathbf{v}\right) - P\nabla \cdot \mathbf{v} = 0. \tag{2.67}$$

When the density is constant in each phase, the heat capacity at constant volume c_V and the heat capacity at constant pressure c_P can be assumed to be the same since we may neglect thermal expansion, so from now on we do not distinguish between the two and write the heat capacity as c. Now, under the same assumption, we find an expression that relates the time derivative of the internal energy to that of the temperature [10],

$$\frac{\mathrm{d}I}{\mathrm{d}t} = c\frac{\mathrm{d}T}{\mathrm{d}t}. \tag{2.68}$$

Subtracting (2.67) from (2.66), and using the relation in (2.68), we may write

$$\rho c\left(\frac{\partial T}{\partial t} + \mathbf{v} \cdot \nabla T\right) = \nabla \cdot (k\nabla T). \tag{2.69}$$

All versions of the heat equation analysed in the thesis stem from the above equation.

To obtain the Stefan condition, the energy conservation across the solid-liquid interface $s(t)$ needs to be studied. The Rankine-Hugoniot condition states that

$$\frac{\partial f}{\partial t} + \nabla \cdot g = 0 \qquad \Rightarrow \qquad [f]_-^+ s_t = [\mathbf{g} \cdot \mathbf{n}]_-^+, \tag{2.70}$$

where $\mathbf{n}$ is the unit normal and f, $\mathbf{g}$ are functions evaluated at either side of $s(t)$. Let

$$f = \rho\left(I + \frac{v^2}{2}\right), \qquad \mathbf{g} \cdot \mathbf{n} = \rho v\left(I + \frac{v^2}{2}\right) + \mathbf{q}. \tag{2.71}$$

The specific enthalpy h may defined as

$$\begin{aligned} h &= c_l(T - T_m^*) + L_m && \text{in the liquid,} \\ &= c_s(\theta - T_m^*) && \text{in the solid.} \end{aligned}$$

Note, the internal energy is just $I = h - P/\rho$. Then we can apply the Rankine-Hugoniot condition to equation (2.66) to obtain

$$\begin{aligned} &\left\{\rho_l\left[\left(c_l\left(T(s,t) - T_m^*\right) + L_m - \frac{P_l}{\rho_l} + \frac{v^2}{2}\right)\right] - \rho_s c_s\left(\theta(s,t) - T_m^*\right)\right\} s_t = \\ &\rho_l v\left[c_l\left(T(s,t) - T_m^*\right) + L_m - \frac{P_l}{\rho_l} + \frac{v^2}{2}\right] - k_l \nabla T\big|_{x=s} + P_l v + k_s \nabla\theta\big|_{x=s}. \end{aligned} \tag{2.72}$$

All versions of the Stefan condition analysed in the thesis result from the equation above.

To retrieve the original Stefan problem given by equations (2.1)-(2.2), we take $\nabla = \partial/\partial x$, neglect pressure effects and assume that the phases are stationary. Then if we impose $T(s,t) = \theta(s,t) = T_m^*$ equation (2.72) reduces to (2.3).

A more realistic model in spherical coordinates is presented in [31]. In it, melting point depression is taken into account. Experimental results of Buffat and Borel [13] report a decrease in the melt temperature of approximately 500 K below the bulk melt temperature for gold nanoparticles with radii of the order of 1 nm. David *et al.* [20] show decreases of 70 K and 200 K in tin and lead nanoparticles, respectively. Liu *et al.* [54] show a decrease of a 10% in melt temperatures of antianginal drugs. Shim *et al.* [97] report molecular dynamics (MD) simulations that show a decrease of 800 K (∼60%) of gold nanoparticles of radius 0.8 nm. This results in taking the melting point temperature T_m as a function of the melt front $R(t)$. The theoretical studies of McCue *et al.* [60], Wu *et al.* [111, 110], Font and Myers [30], Back *et al.* [7, 6] include melting point depression. In [31] they also consider change in densities between phases. Thus, the liquid velocity v is no longer taken to be zero and in the spherically symmetric system has the form

$$v = \frac{r^2}{R^2}\left(1 - \frac{\rho_s}{\rho_l}\right) R_t. \tag{2.73}$$

These assumptions, and neglecting pressure effects again, transform (2.69) (for both liquid and solid phases) into

$$\rho_l c_l \left(\frac{\partial T}{\partial t} + \frac{r^2}{R^2}\left(1 - \frac{\rho_s}{\rho_l}\right)\frac{\mathrm{d}R}{\mathrm{d}t}\frac{\partial T}{\partial r}\right) = k_l \frac{1}{r^2}\frac{\partial}{\partial r}\left(r^2 \frac{\partial T}{\partial r}\right), \qquad R(t) < r < R_b, \tag{2.74}$$

$$\rho_s c_s \frac{\partial \theta}{\partial t} = k_s \frac{1}{r^2}\frac{\partial}{\partial r}\left(r^2 \frac{\partial \theta}{\partial r}\right), \qquad 0 < r < R(t), \tag{2.75}$$

whilst the Stefan condition (2.72) is now

$$\rho_s \left[(c_l - c_s)\left(T_m(t) - T_m^*\right) + L_m + \frac{v^2}{2}\right] R_t = k_s \nabla\big|_{r=R} - k_l \nabla T\big|_{r=R}. \tag{2.76}$$

The boundary conditions are $T(s,t) = \theta(s,t) = T_m(t)$ and $T(R_b,t) = T_H$. Note that now there is an additional moving boundary R_b due to the fact that because both phases have a different density a volume expansion occurs. This form of the Stefan problem is examined in [30, 31].

Size-dependent latent heat

An effect of the high ratio of surface to volume atoms in nanoparticles is the size-dependent latent heat. Molecular dynamics (MD) simulations and experiments have demonstrated a decrease in latent heat with a decrease in radius. Lai *et al.* [50] presented the first calorimetry measurements of the melting process of nanometer-sized tin particles, ranging from $5 - 50$ nm in diameter. They found a reduction of up to 70% from the bulk latent heat for the smaller sized particles. Jiang *et al.* [46] improved the measurement technique to find even greater reductions. Using a thin-film scanning calorimetry technique similar behaviour was observed by Zhang *et al.* [117] in a study of the melting behaviour of $0.1 - 10$ nm-thick discontinuous indium films made from ensembles of nanostructures. In the MD studies of Bachels *et al.* [5] the melt temperature of 1.4 nm radius tin particles is 25% lower than the bulk value while the latent heat is 45% lower. Ercolessi *et al.* [25], Lim *et al.* [53] and Delogu [22] have carried out MD studies on gold, lead and copper clusters, all showing the same qualitative behaviour. For this reason, in Chapter 4 a variable latent heat will be included in the model.

The thesis of Back [8, §7.1-7.4] includes size-dependent latent heat, using the formula provided by Lai *et al.* [50] in the standard energy balance. However, Lai's formula [50] underestimates the value of latent heat near bulk values. Other formulations [98, 112] do not match experimental data. In Chapter 4 we propose an exponential fit to the data for tin nanoparticles which tends to the correct bulk value and agrees very well with experimental data down to around $R = 8$ nm. Another problem with the study in Back [8, §7.1-7.4] is in the energy balance at the interface between the two phases, which we discuss below.

New Stefan condition

The error in Back [8, §7.1-7.4] is that the Stefan condition is based on an implicit assumption that the latent heat is released at the bulk melt temperature, which is incorrect. Recently, Myers [70] proposed a new formulation for the Stefan condition. This new derivation stems from the definition of latent heat, which is *the jump in specific enthalpy at the phase change temperature*, that is, $L_m(t) = (h_l - h_s)\big|_{\theta=T=T_m(t)}$. This effectively means that in equation (2.76) T_m^* should be replaced by $T_m(t)$. Further, pressure variation at the nanoscale can be

significant. This leads to the final form of the Stefan condition

$$\rho_s \left[L_m(t) + \frac{2\sigma_{sl}}{\rho_s R} + \frac{v^2}{2} \right] R_t = k_s \nabla\theta\big|_{r=R} - k_l \nabla T\big|_{r=R}. \tag{2.77}$$

Newton cooling boundary condition

The fixed temperature boundary condition $T(R_b, t) = T_H$ is equivalent to specifying perfectly efficient heat transfer from the surrounding material, that is the heat transfer coefficient is infinite. Consider a particle initially at some temperature below the melt temperature. At $t = 0$ the infinite heat transfer instantaneously raises the boundary temperature to T_H, which results in an infinite temperature gradient and so, according to the Stefan condition, an infinite boundary velocity. Clearly this is unrealistic, so in this thesis we will generally employ a Newton cooling condition at the outer boundary which states that the energy transferred to the particle is proportional to the temperature difference between the particle surface and the surrounding material,

$$-k_l \frac{\partial T}{\partial r}\bigg|_{r=R_b} = h(T(R_b, t) - T_H), \tag{2.78}$$

where h is the heat transfer coefficient. The fixed temperature boundary condition of previous studies is the limit of equation (2.78) as $h \to \infty$. Of course this cannot be achieved physically and there exists a limit to the heat transfer beyond which the material would be vaporised. The highest possible value for h which still permits thermodynamic stability is

$$h_{\max} = \frac{q_{\max}}{\Delta T}, \qquad q_{\max} = \rho_s u v_s, \tag{2.79}$$

where u is the internal energy and v_s is the speed of second sound in the material, see [28, 47].

3 | Optimising the heat balance integral method in spherical and cylindrical Stefan problems

---

H. Ribera, T. G. Myers, M. M. MacDevette
Optimising the heat balance integral method in spherical and cylindrical Stefan problems
Submitted to Heat and Mass Transfer
Impact factor: 1.233

Abstract

The Heat Balance Integral Method (HBIM) is generally applied to one-dimensional Cartesian heat flow and Stefan problems. The main reason for this being that solutions in spherical and cylindrical coordinates are less accurate than in Cartesian. Consequently, in this paper we examine the application of the HBIM to Stefan problems in spherical and cylindrical coordinates, with the aim of improving accuracy. The standard version as well as one designed to minimise errors will be applied on the original and transformed system. Results are compared against numerical and perturbation solutions. It is shown that for the spherical case it is possible to obtain highly accurate approximate solutions (more accurate than the first order perturbation for realistic values of the Stefan number). For the cylindrical problem the results are significantly less accurate.

3.1 Introduction

The Heat Balance Integral Method (HBIM) is an approximate solution method primarily applied to thermal and phase change problems. It has become popular largely due to its simplicity. For example, when solving a single heat equation the method permits the governing partial differential equation to be transformed to a first order ordinary differential equation, which may often be solved analytically. It is particularly useful in solving Stefan problems, where there exist very few practically useful solutions and generally numerics are required.

The HBIM was developed by Goodman [38] and is most commonly applied to problems in a Cartesian geometry. However, there exist many situations where an approximate solution method in cylindrical or spherical coordinates is required. Spherical Stefan problems are described in the context of the Earth cooling in [90], they are also important in industrial applications such as paint pigments, polishing materials and laser cladding [41, 49]. Recently there has been great interest in the melting process at the nanoscale. Studies on spherical nanoparticle melting are often motivated by the development of new materials, although there are many important applications in medicine and drug delivery, see [84, 94, 30]. Phase change in cylindrical geometries is of interest in everyday applications such as icicle growth and melting, and certain thermal storage systems [96]. At the microscale solidification in a cylindrical geometry has been studied in the context of phase change microvalves and cryopreservation [76, 77]. At the nanoscale there exists great interest in the formation or melting of nanowires, see [84, 113, 28]. Consequently, there is a clear need to develop solution techniques to complement this interest in thermal and melting problems in spherical and cylindrical geometries.

The Cartesian version of the HBIM is described in detail in a number of texts [86, 92, 108, 56], while there are less published works dealing with the spherical or cylindrical versions [105, 16, 14]. Hill [40] summarizes techniques for analytical and series solutions for one-dimensional Stefan problems, including that of the HBIM in cylindrical and spherical coordinates. Ren [86] studies Cartesian and spherical geometries subject to a specified solidification front velocity and compares results for both one and two phase problems against numerics. In [78] a modified form of HBIM is applied to a spherically symmetric

domain to determine the thermal conductivity of a nanofluid.

Various authors use the HBIM as the basis for a numerical scheme. In a series of papers Bell looked into subdividing the spatial and dependent variables in planar and cylindrical geometries, see [9, 61]. This is analogous to a numerical marching scheme on the heat balance equations whose accuracy increases with increased number of subdivisions. Caldwell and Chiu [15] extended this method, working with cylindrical and spherical geometries. Their solution shows some inaccuracies for small Stefan numbers and has non-physical oscillations for coarse grids. In a separate paper they detail the necessary starting solution for their scheme. In [68, 109] linear profiles are employed in the subdivision. This requires an increase in the number of subregions to improve accuracy. Mitchell [61] uses a boundary immobilisation technique together with a standard HBIM profile. This leads to highly accurate solutions with a very small number of subregions. The method does not require a separate small time solution and can be applied to realistic boundary conditions, rather than the fixed temperature condition used in most studies.

Various modifications of the HBIM have appeared in the literature, with the aim of improving the approximation. Sadoun [91] introduced the Refined Integral Method (RIM) which involves integrating the heat equation twice and simplifying the resultant integral via the standard HBIM integral. An alternative approach to the RIM, termed the ARIM, is mentioned in [63] where they point out that the resultant integral form may be simpler to deal with, especially when combined with a zero flux boundary condition. Mitchell and Myers [64, 79] proposed the Combined Integral Method (CIM) which combines both HBIM and RIM. However (for standard boundary conditions) the most accurate formulation comes through the opTimal Integral Method (henceforth termed the TIM), which involves minimising the least squares error when the approximating function is substituted into the heat equation [73, 74].

In the following section we will specify the basic one-dimensional, one-phase Stefan problem, to be used in the remainder of the paper. Studying the one-phase problem reduces the length of the expressions and so simplifies the analysis, making the exposition of the method clearer. We note that the one-phase formulation is known to lose energy when the phase change temperature is variable (such as with melting at the nanoscale or with supercooled fluids [72, 29]). In the following we will avoid this issue by only dealing with fixed phase

change temperature but the method could easily be extended to a variable temperature. In §3.3 we analyse phase change due to a fixed temperature boundary condition since this is the basic condition studied in the majority of papers. However, in reality the fixed temperature boundary condition is physically unrealistic so, in Section 3.4, we study the case of a Newton cooling condition.

3.2 Mathematical modelling

Consider a solid sphere or cylinder of initial radius $R = R_0$ which is at the melt temperature, T_m. At $t = 0$ the outer boundary temperature is increased such that melting begins and progresses inwards until the whole particle has turned to liquid. The liquid occupies the region $R(t) < r < R$, where $R(t)$ denotes the position of the melting front, and has initial condition $R(0) = R_0$. The problem is described by the standard one-phase formulation

$$\rho c \frac{\partial T}{\partial t} = \frac{k}{r^p} \frac{\partial}{\partial r} \left(r^p \frac{\partial T}{\partial r} \right), \qquad R(t) < r < R_0, \tag{3.1}$$

where ρ, c and k denote the density, specific heat and conductivity, respectively. We assume ρ is constant and equal in the solid and liquid phases throughout the melt process (this is not necessary for the analysis, but again we choose this to make the mathematics clearer). The choice $p = 2$ describes the heat equation in spherical coordinates. We may also examine Cartesian and cylindrical geometries by setting $p = 0$, 1, respectively. The position of the interface is determined by the Stefan condition

$$\rho L_m \frac{\mathrm{d}R}{\mathrm{d}t} = -k \frac{\partial T}{\partial r}\bigg|_{r=R}, \tag{3.2}$$

where L_m denotes the latent heat. These equations are subject to the following boundary and initial conditions

$$\begin{gathered} T(R,t) = T_m, \qquad T(r,0) = T_m, \qquad R(0) = R_0, \\ \text{(a)}\ \ T(R_0,t) = T_H, \qquad \text{or} \qquad \text{(b)}\ \ -k \frac{\partial T}{\partial r}\bigg|_{r=R_0} = h(T(1,t) - T_H), \end{gathered} \tag{3.3}$$

where at the outer boundary we will impose either a fixed temperature or Newton cooling condition.

Introducing the nondimensional variables

$$\hat{t} = \frac{k}{\rho c R_0^2} t, \qquad \hat{T} = \frac{T - T_m}{\Delta T}, \qquad \hat{r} = \frac{r}{R_0}, \qquad \hat{R} = \frac{R}{R_0}, \tag{3.4}$$

where $\Delta T = T_H - T_m$, the problem (3.1)-(3.3) may be written (dropping the hat notation) as

$$\frac{\partial T}{\partial t} = \frac{1}{r^p}\frac{\partial}{\partial r}\left(r^p \frac{\partial T}{\partial r}\right), \qquad R(t) < r < 1, \tag{3.5}$$

subject to

$$\begin{gathered} T(R,t) = 0, \qquad T(r,0) = 0, \qquad R(0) = 1, \\ \text{(a)}\ \ T(1,t) = 1, \qquad \text{or} \qquad \text{(b)}\ \ \left.\frac{\partial T}{\partial r}\right|_{r=1} = \mathrm{Nu}(1 - T(1,t)), \end{gathered} \tag{3.6}$$

where $\mathrm{Nu} = (R_0 h)/k$ is the Nusselt number. The Stefan condition becomes

$$\beta \frac{\mathrm{d}R}{\mathrm{d}t} = -\left.\frac{\partial T}{\partial r}\right|_{r=R}, \qquad R(0) = 1\,, \tag{3.7}$$

where $\beta = L_m/(c\Delta T)$ is the Stefan number.

3.3 Fixed temperature boundary condition

The most commonly used boundary condition in the mathematical study of Stefan problems is that of a fixed temperature, $T(R_0, t) = T_H > T_m$. Hence in this section we will always apply equation (3.6a) at the boundary. Physically it is unrealistic since it requires an infinite flux at the beginning of the melting process, however the mathematics involved is relatively simple so we begin our analysis with this case and subsequently move on to the more realistic case of a cooling condition.

3.3.1 Spherical Stefan problem

We begin our analysis with a study of the spherical problem in the original coordinate system, defined by equations (3.5)-(3.7) with $p = 2$, and subsequently a transformed system. Results are then compared with a numerical solution.

HBIM formulation

All heat balance methods involve choosing a simple function (usually a polynomial) to approximate the temperature over a finite region [63]. We choose a standard form

$$T(r,t) = a(t)\left(\frac{r-R}{1-R}\right) + b(t)\left(\frac{r-R}{1-R}\right)^n + c(t). \tag{3.8}$$

To follow the original HBIM we now assume $n = 2$. The boundary conditions indicate $c = 0$ and $b = 1 - a$. In the Cartesian case a is a constant, in spherical co-ordinates it turns out to be a function of time. Hence the expression for T involves two unknown functions, $a(t)$ and $R(t)$. The first of the two equations to determine these unknowns is found by substitution of T into the Stefan condition (3.7). This leads to an ordinary differential equation

$$\beta \frac{\mathrm{d}R}{\mathrm{d}t} = -\frac{a}{1-R}\,. \tag{3.9}$$

A second equation, termed the Heat Balance Integral (HBI), comes from integrating the heat equation (3.5) over the region $r \in [R, 1]$,

$$\int_R^1 r^2 \frac{\partial T}{\partial t}\,\mathrm{d}r = \int_R^1 \frac{\partial}{\partial r}\left(r^2 \frac{\partial T}{\partial r}\right)\mathrm{d}r \quad \Rightarrow \quad \frac{\mathrm{d}}{\mathrm{d}t}\int_R^1 r^2 T(r,t)\,\mathrm{d}r = \left.\frac{\partial T}{\partial r}\right|_{r=1} - R^2 \left.\frac{\partial T}{\partial r}\right|_{r=R}. \tag{3.10}$$

Upon substituting the approximating function (3.8) into this expression we obtain

$$\frac{\mathrm{d}}{\mathrm{d}t}\left[\frac{(1-R)\left(\left(24 + \left(n^3 + 6\,n^2 + 11\,n - 18\right)a\right)R^2 + 2\,(1+n)\left(12 + \left(n^2 + 5\,n - 6\right)a\right)R\right)}{(2+n)\,(3+n)\,(1+n)}\right.$$
$$\left.\frac{(1-R)\,(3\,(4 + (n-1)\,a)\,(1+n)\,(2+n))}{(2+n)\,(3+n)\,(1+n)}\right] = -\frac{aR^4}{(1-R)}. \tag{3.11}$$

Since $n = 2$ is constant we may write (3.11) as

$$\frac{\mathrm{d}}{\mathrm{d}t}\left[\frac{1}{20}\,(1-R)\left(\left(\frac{2}{3} + a\right)R^2 + \left(\frac{4a}{3} + 2\right)R + 4 + a\right)\right] = -\frac{aR^4}{(1-R)}. \tag{3.12}$$

The initial condition for the melt front $R(0) = 1$ is known, but the condition for a is not. The classical Neumann solution for Cartesian phase change driven by a constant temperature boundary condition shows $R \sim \sqrt{t}$. The current problem, which describes spherical melting, (3.5)-(3.7), reduces to the Neumann problem provided the melt region is small compared to the radius. Hence, for small times, we may approximate the moving boundary position as

$$R \approx 1 - 2\lambda t^{1/2}, \tag{3.13}$$

where λ is an unknown constant. For the spherical problem this form has been used in [31]. Substituting this, and the derivative of T into the Stefan condition (3.9) determines

$$a \approx \frac{\beta\lambda^2}{2}(1 - 2\lambda t^{1/2}), \tag{3.14}$$

hence,

$$a(0) = \frac{\beta\lambda^2}{2}. \tag{3.15}$$

To find the value for λ we substitute the small time solutions (3.13), (3.15) into the heat balance (3.11), which in the limit $t \to 0$ gives a quadratic for λ^2

$$2\beta(n-1)\lambda^4 + (2\beta n + 2 + 2\beta n^2)\lambda^2 - n^2 - n = 0\ . \tag{3.16}$$

The standard HBIM solution to the Stefan problem is now described by equations (3.9), (3.11) with $n = 2$. The numerical solution of (3.27), (3.11), subject to $R(0) = 1$, $a(0) = \beta\lambda^2/2$ is trivial.

TIM formulation

The standard HBIM of Goodman [38] simply imposed $n = 2$, as in the previous section, although there are many other possibilities, often chosen through knowledge of an exact solution, see [64]. The opTimal Integral Method (TIM) was developed so that n is chosen to improve the accuracy of the standard method without the need for an exact or numerical solution [73, 74]. This involves minimising a least-squares error. Thus a third equation is introduced

$$E_n(r,t) = \int_R^1 \left(\frac{\partial T}{\partial t} - \frac{2}{r}\frac{\partial T}{\partial r} - \frac{\partial^2 T}{\partial r^2} \right)^2 \mathrm{d}r. \tag{3.17}$$

This approach has a number of advantages, the most obvious is that it significantly improves accuracy, for certain boundary conditions by orders of magnitude [73, 74]. It also provides a measure of the error without knowledge of an exact solution. The algebra involved in the integral may be complex, which has been quoted as a drawback [41]. However, it is unnecessary to carry out the algebra every time the method is used. For standard Cartesian thermal problems in a fixed domain: for a constant temperature boundary condition the appropriate value is $n = 2.235$, while for constant flux and Newton cooling boundary conditions $n = 3.584$, see [74]. The Stefan problem with a fixed temperature boundary condition gives $n = 1.79$; with constant flux or a Newton cooling condition, $n = 3.48$.

The TIM formulation is fully specified by equations (3.9), (3.11), (3.17) for the 3 unknowns a, n, R, subject to the temperature profile (3.8).

As in the standard HBIM we solve (3.9) and (3.11) numerically, but now for a range of n. The error E_n is then calculated to determine the minimum value and corresponding value

of n. It turns out that the optimal n varies with β. For $\beta \in [1, 10]$ we find $n \in [1.73, 1.77]$. As we will see later, the average value is accurate over a wide range of β, so effectively with a fixed temperature condition the TIM requires solving the two ODEs (3.9), (3.11) with $n = 1.75$.

Perturbation solution

Perhaps the most popular method for finding approximate solutions to Stefan problems is via the large Stefan number perturbation. This involves assuming that $\beta \gg 1$, although this limit is not always of practical interest: in [3, Chap 2.1] typical parameter values for the phase change of water, copper, paraffin wax and silicon dioxide are provided, these show $\beta \in [2 \times 10^{-3}, 8.3]$ (note their Stefan number $St = 1/\beta$).

The $\beta \gg 1$ limit corresponds to slow melting and requires time to be rescaled such as $\tau = \epsilon t$, where $\epsilon = 1/\beta$. Now the problem statement becomes

$$\epsilon \frac{\partial T}{\partial \tau} = \frac{1}{r^2} \frac{\partial}{\partial r} \left(r \frac{\partial^2 T}{\partial r^2} \right), \qquad R(\tau) < r < 1, \tag{3.18}$$

$$T(R, \tau) = 0, \qquad T(0, \tau) = 1, \tag{3.19}$$

$$\frac{\mathrm{d}R}{\mathrm{d}\tau} = -\frac{\partial T}{\partial r}\bigg|_{r=R}. \tag{3.20}$$

We then approximate the solution for T by a power series in the small parameter ϵ, $T(r, \tau) = T_0 + \epsilon T_1 + \mathcal{O}\left(\epsilon^2\right)$. Applying this expansion to the governing equation (3.18) and grouping terms with the same power of ϵ we find the leading and first order temperatures to be

$$T_0 = \frac{r - R}{r(1 - R)}, \tag{3.21}$$

$$T_1 = -\frac{(r-1)(R-2+r)(R-r)}{6r(1-R)^2} \frac{\mathrm{d}R}{\mathrm{d}\tau}. \tag{3.22}$$

Substituting the first order approximation of T into the Stefan condition (3.20) gives

$$\frac{\mathrm{d}R}{\mathrm{d}\tau} = -\frac{3}{(1-R)(3R+\epsilon)}\ . \tag{3.23}$$

Equation (3.23) can easily be solved via MATLAB's `ode45`, with initial condition $R(0) = 1$. We may also easily integrate this expression to find an implicit solution for R (a cubic equation in R), but when solving the cubic numerically there is a jump in roots so we prefer to use the ODE solver.

Approximate solutions in the transformed system

The equations for the transformed system come from making the change $u = Tr$. The problem then becomes

$$\frac{\partial u}{\partial t} = \frac{\partial^2 u}{\partial r^2}, \qquad R < r < 1, \tag{3.24}$$

$$u(R,t) = 0 = u(r,0), \qquad u(1,t) = 1\ , \qquad R(0) = 1 \tag{3.25}$$

$$\beta R \frac{\mathrm{d}R}{\mathrm{d}t} = -\left.\frac{\partial u}{\partial r}\right|_{r=R}. \tag{3.26}$$

To approximate the temperature over a finite region we choose the standard form of equation (3.8), and replace T by u. The boundary conditions again determine $c = 0$ and $b = 1 - a$. As before we use the Stefan condition and the HBI to define equations for R and a. The Stefan condition gives

$$\beta R \frac{\mathrm{d}R}{\mathrm{d}t} = -\frac{a}{1-R}\,. \tag{3.27}$$

The heat balance integral is

$$\int_R^1 \frac{\partial u}{\partial t}\,\mathrm{d}r = \int_R^1 \frac{\partial^2 u}{\partial r^2}\,\mathrm{d}r \quad \Rightarrow \quad \frac{\mathrm{d}}{\mathrm{d}t}\int_R^1 u(r,t)\,\mathrm{d}r = \left.\frac{\partial u}{\partial r}\right|_{r=1} - \left.\frac{\partial u}{\partial r}\right|_{r=R}. \tag{3.28}$$

Upon substituting the approximating function u into this expression and assuming constant n, we obtain

$$(n-1)(1-R)^2\frac{\mathrm{d}a}{\mathrm{d}t} - (1-R)[(n-1)a+2]\frac{\mathrm{d}R}{\mathrm{d}t} = 2n(n+1)(1-a). \tag{3.29}$$

To find λ we again let $t \to 0$ and substitute into the HBIM (3.28). The solution to the Stefan problem is now described by equations (3.27), (3.29) subject to initial conditions $R(0) = 1$, $a(0) = 2\beta\lambda^2$.

In the transformed system the TIM solution requires finding the value for n that minimises the error

$$E_n(n,t) = \int_R^1 \left(\frac{\partial u}{\partial t} - \frac{\partial^2 u}{\partial r^2}\right)^2 \mathrm{d}r. \tag{3.30}$$

As before we simply solve the ODEs (3.26), (3.29) numerically for a range of n and then determine the value that minimises (3.30). We find that for $\beta \in [1,\ 10]$, $n \in [1.55,\ 1.65]$, so in general we choose $n = 1.6$.

The leading and first order perturbation solutions are

$$u_0 = rT_0, \qquad u_1 = rT_1 \tag{3.31}$$

where T_0, T_1 are given by (3.21), (3.22), and the melt front is described by (3.23). That is, the perturbation solution in the transformed system is identical to that of the original system.

Numerical solution

To ascertain the accuracy of the various solutions we will now formulate a numerical solution. To do this, we employ a finite difference scheme, following the work of Font *et al.* [31]. There are two key steps: the first one consists of changing the temperature variable to $u = rT$; the second involves introducing a new coordinate to immobilise the boundary, $\eta = (r - R)/(1 - R)$. This transforms the problem to

$$(1-R)^2\frac{\partial u}{\partial t} = (1-R)(1-\eta)\frac{\partial u}{\partial \eta}R_t + \frac{\partial^2 u}{\partial \eta^2}, \qquad 0 < r < 1, \tag{3.32}$$

$$u(0,t) = 0, \qquad u(1,t) = 1, \tag{3.33}$$

$$\beta R\frac{\mathrm{d}R}{\mathrm{d}t} = -\frac{1}{1-R}\frac{\partial u}{\partial \eta}\bigg|_{\eta=0}. \tag{3.34}$$

We use standard finite differences to approximate the temperature derivatives,

$$\frac{\partial u}{\partial t} = \frac{u_i^{n+1} - u_i^n}{\Delta t}, \qquad \frac{\partial u}{\partial \eta} = \frac{u_{i+1}^{n+1} - u_{i-1}^{n+1}}{2\Delta\eta}, \qquad \frac{\partial^2 u}{\partial \eta^2} = \frac{u_{i+1}^{n+1} - 2u_i^{n+1} + u_{i-1}^{n+1}}{\Delta\eta^2}, \tag{3.35}$$

where $i = 1, \ldots, J$ and $n = 1, \ldots, N$. Hence we may write

$$u_i^{n+1} = 0, \qquad i = 1, \tag{3.36}$$

$$a_i^n u_{i-1}^{n+1} + b_i^n u_i^{n+1} + c_i^n u_{i+1}^{n+1} = d^n u_i^n, \qquad i = 2, \ldots, J-1, \tag{3.37}$$

$$u_i^{n+1} = 1, \qquad i = J, \tag{3.38}$$

which allows us to write down a matrix system that we solve at every time step n. We determine the position of the melt front via the Stefan condition (3.34) using a three-point backward difference for the partial derivative, and taking the time derivative to be

$$\frac{dR}{dt} = \frac{R^{n+1} - R^n}{\Delta t}. \tag{3.39}$$

Small time analysis

A common difficulty when solving Stefan problems numerically is that the liquid phase does not exist at $t = 0$, however a numerical solution demands initial values. To overcome this

difficulty we look for a small time solution to provide an initial guess within the numerical scheme. As stated earlier, at small times $R = 1 - 2\lambda t^{1/2}$, substituting this into equation (3.32) and letting $t \to 0$ gives

$$\frac{\partial^2 u}{\partial \eta^2} \approx 0. \tag{3.40}$$

Applying the boundary condition (3.33) yields $u(\eta, t) = \eta$. Substituting this expression into the Stefan condition (3.34) allows us to find $\lambda = \sqrt{1/(2\beta)}$. So we start our scheme at some time $t = t_0 \ll 1$, with $u(\eta, t_0) = \eta$ and $R(t_0) = 1 - \sqrt{(2t_0)/\beta}$.

Comparison of results

The most important variable in the Stefan problem is the position of the melt front $R(t)$: the main reason for solving the heat equation is to find the temperature gradient which then drives the phase change. Consequently, in Figure 3.1 we show a comparison of the melt front predictions of the numerical solution (solid line) and the approximate solutions in the original domain for $\beta = 1, 10$. The TIM, the HBIM with $n = 2$ and perturbation solutions are shown as dashed, dash-dotted and dotted lines, respectively. For $\beta = 1$ all solutions are inaccurate. When $\beta = 10$ the perturbation solution is very close to the numerical solution while the other solutions are again inaccurate. In Figure 3.2 we show the equivalent results, but now calculated in the transformed system. For $\beta = 1$ the TIM shows reasonable agreement, with a final melt time some 7% larger than the numerical prediction. The HBIM and perturbation solutions are highly inaccurate. For $\beta = 10$ we expect the large β perturbation to be accurate, and indeed it is much closer to the numerical solution now. However, as is clear from the inset, the TIM is significantly more accurate. This is in keeping with the results of [79] where it is shown that for $\beta \in [0.1, 10]$ their heat balance method is more accurate than the second order small and large β perturbation solutions. For $\beta > 10$ both their heat balance solution and the perturbation are highly accurate, with errors below 0.01%. From these two figures we can conclude that in spherical co-ordinates the most accurate solution is generally obtained via the TIM, that is with $n = 1.6$, in the transformed system.

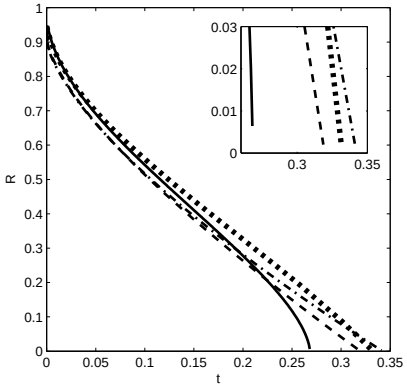

(a) $\beta = 1$.

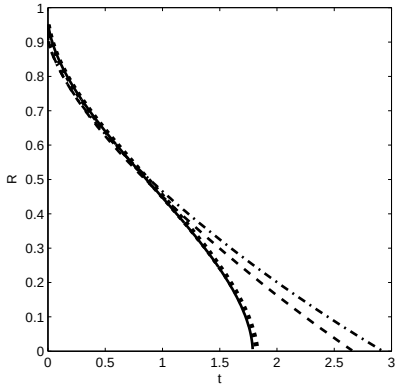

(b) $\beta = 10$.

Figure 3.1: Melting front evolution of a spherical particle in the original system for HBIM (dash-dotted), TIM (dashed), perturbation (dotted) and numerical (solid) solutions for $\beta = 1$, 10.

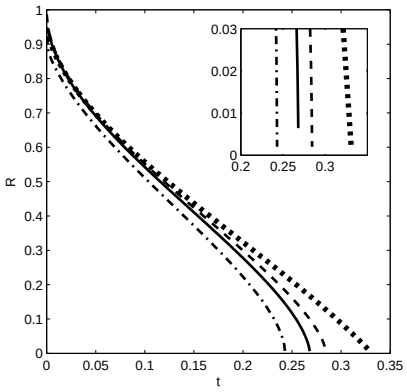

(a) $\beta = 1$.

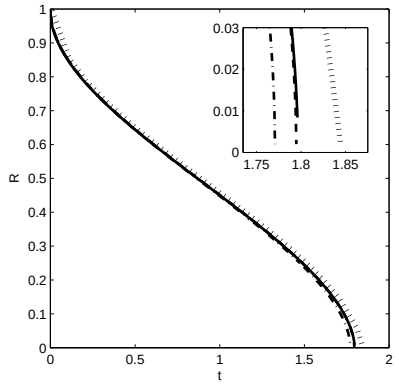

(b) $\beta = 10$.

Figure 3.2: Melting front evolution of a spherical particle in the transformed system for HBIM (dash-dotted), TIM (dashed), perturbation (dotted) and numerical (solid) solutions for various β.

3.3.2 Cylindrical Stefan problem

In this section we focus on the cylindrical Stefan problem. We will follow the methods outlined in the previous section and so will omit much of the detail. Again we first solve the problem in the original system, equations (3.5)-(3.7) taking $p = 1$, and later on provide approximate solutions for a transformed system.

Approximate solutions in the original cylindrical coordinates

We assume a temperature profile of the form (3.8) where $c = 0$ and $b = 1 - a$. The heat balance integral may now be expressed as

$$\frac{\mathrm{d}}{\mathrm{d}t}\int_R^1 rT\,\mathrm{d}r = \left.\frac{\partial T}{\partial r}\right|_{r=1} - R\left.\frac{\partial T}{\partial r}\right|_{r=R}. \tag{3.41}$$

Substituting for T leads to a rather long expression for the ODE, similar to (3.11), so we omit it in this section.

We close the system by inserting the assumed temperature profile (3.8) into the Stefan condition (3.7), to reproduce (3.9). For small times, for a sufficiently thin melt region the governing equations are equivalent to the Cartesian system so again we may write $R \approx 1 - 2\lambda t^{1/2}$, $a \approx \beta\lambda^2/2$. In the limit $t \to 0$ the HBI provides an equation for λ,

$$\frac{n}{2} - \frac{1}{2}\lambda\beta n = \frac{\lambda}{8(n+1)(4+\beta\lambda^2(n-1))}. \tag{3.42}$$

For the standard HBIM we substitute $n = 2$ to determine $\lambda(\beta)$. For the TIM, n is chosen to minimise the error function (calculated using MATLAB)

$$E(n,t) = \int_R^1 \left(\frac{\partial T}{\partial t} - \frac{1}{r}\frac{\partial T}{\partial r} - \frac{\partial^2 T}{\partial r^2}\right)^2 \mathrm{d}r. \tag{3.43}$$

Numerical integration of the above gives $n \in [1.404, 1.6869]$ as the optimal choice for $\beta \in [1, 10]$.

For the perturbation solution we rescale time and expand the temperature in powers of ϵ to find the leading and first order solutions

$$T_0(r,t) = 1 - \frac{\ln(r)}{\ln(R)}, \tag{3.44}$$

$$T_1(r,t) = \frac{((R^2-r^2)\ln(r) + r^2 - 1)\ln(R) + (1-R^2)\ln(r)}{4R\ln(R)^3}\frac{\mathrm{d}R}{\mathrm{d}t}. \tag{3.45}$$

Upon substitution into the Stefan condition, the melt front satisfies

$$\frac{\mathrm{d}R}{\mathrm{d}t} = -\frac{4\beta R\ln(R)^2}{4\beta R^2\ln(R)^3 + 2R^2\ln(R)^2 - 2R^2\ln(R) + (R^2-1)}, \tag{3.46}$$

with $R(0) = 1$.

Approximate solutions in a transformed system

The transformation $u = rT$ does not help in this case. Instead we follow [40, 42] and use the following boundary fixing transformation,

$$\rho = \frac{\ln(r)}{\ln(R)}, \quad \tau = \ln(R), \quad T(r,t) = u(\rho,\tau). \tag{3.47}$$

The cylindrical problem becomes

$$e^{-2\tau\rho}\frac{\partial^2 u}{\partial \rho^2} = \tau\frac{\mathrm{d}\tau}{\mathrm{d}t}\left(\tau\frac{\partial u}{\partial \tau} - \rho\frac{\partial u}{\partial \rho}\right), \quad \rho \in [0,1], \quad \tau < 0 \tag{3.48}$$

$$u(1,\tau) = 1, \quad \text{(a)}\ \ u(0,\tau) = 1 \qquad \tau(0) = 0, \tag{3.49}$$

$$\left.\frac{\partial u}{\partial \rho}\right|_{\rho=1} = -\beta e^{2\tau}\tau\frac{\mathrm{d}\tau}{\mathrm{d}t}\,. \tag{3.50}$$

To remove the t dependence in equation (3.48) we may substitute for τ_t from the Stefan condition.

This transformation complicates the heat equation, with the result that if we leave n unknown the HBI cannot be integrated analytically, hence we cannot specify one of the ODEs for the TIM solution. However, we may still make progress for the particular case $n = 2$.

The quadratic polynomial satisfying boundary conditions (3.49) is

$$u(\rho,\tau) = 1 - (1+a)\rho + a\rho^2. \tag{3.51}$$

where $a = a(\tau)$. The HBI is obtained by integrating the heat equation (3.48) over the domain $\rho \in [0,1]$, after removing the t dependence via the Stefan condition. This leads to

$$\int_0^1 \beta\frac{\partial^2 u}{\partial \rho^2}\,\mathrm{d}\rho = \int_0^1 e^{2\tau(\rho-1)}(a-1)\left[\rho\frac{\partial u}{\partial \rho} - \tau\frac{\partial u}{\partial \tau}\right]\mathrm{d}\rho. \tag{3.52}$$

Applying u from (3.51) leads to the ODE for $a(\tau)$,

$$\frac{\mathrm{d}a}{\mathrm{d}\tau} = \frac{e^{-2\tau}\left(a^2(\tau+2) - 2a - \tau\right) + 8\beta a\tau^3 - 2\tau^2(a-1)^2 + (1+3a^2-4a)\tau + 2a(1-a)}{\tau(a-1)((\tau+1)e^{-2\tau} + \tau - 1)}. \tag{3.53}$$

Note, unlike in previous examples we now only have a single equation to solve for $a(\tau)$, although again we do not know the initial condition. To find the value of $a(0)$ we apply the small time solution $\tau = \ln(R) = \ln\left(1 - 2\lambda t^{1/2}\right)$ to the Stefan condition (3.50). Taking the limit $t \to 0$ gives

$$a(0) = 1 - 2\lambda^2\beta. \tag{3.54}$$

Substituting for a, τ into (3.53) leads to a quadratic for λ,

$$\frac{1}{3}\lambda^4\beta^2 + \left(\frac{\beta}{3} + 2\beta^2\right)\lambda^2 - \beta = 0. \tag{3.55}$$

Now we simply have to solve (3.53) numerically over the range $\tau \in [0, -\infty]$ subject to (3.54). With this transformation the melt front is at $R = e^{\tau}$. Once a is known we can convert from τ to t by solving the Stefan condition (3.50)

$$\frac{\mathrm{d}\tau}{\mathrm{d}t} = -\frac{a-1}{\beta}e^{2\tau}\ , \tag{3.56}$$

In practice we calculate t via the discretisation

$$t_i = t_{i-1} - \frac{\beta\tau_{i-1}e^{2\tau_{i-1}}}{a_{i-1}-1}\left(\tau_i - \tau_{i-1}\right) \tag{3.57}$$

where $t_0 = 0$.

With a large Stefan number we rescale time scale to obtain

$$\epsilon\tau\frac{\mathrm{d}\tau}{\mathrm{d}t}\left(\tau\frac{\partial u}{\partial\tau} - \rho\frac{\partial u}{\partial\rho}\right) = e^{-2\tau\rho}\frac{\partial^2 u}{\partial\rho^2}, \qquad 0 < \rho < 1, \tag{3.58}$$

$$\left.\frac{\partial u}{\partial\rho}\right|_{\rho=1} = -e^{2\tau}\tau\frac{d\tau}{dt}\,. \tag{3.59}$$

subject to (3.49). This leads to

$$u_0 = 1 - \rho, \tag{3.60}$$

$$u_1 = -\frac{(1-\rho\tau)e^{2\rho\tau} + \rho e^{2\tau}(\tau - 1) - 1 + \rho}{4\tau^2}\frac{\mathrm{d}\tau}{\mathrm{d}t}. \tag{3.61}$$

Finally, we find that the melt front is given by the same expression as in (3.46).

Numerical solution

To solve the cylindrical problem numerically we immobilise the boundary as in the spherical case via the coordinate $\eta = (r - R)/(1 - R)$. The governing equations (3.5)-(3.7) transform to

$$(1-R)^2\frac{\partial T}{\partial t} = \left((1-\eta)(1-R)\frac{\mathrm{d}R}{\mathrm{d}t} + \frac{1-R}{\eta(1-R)+R}\right)\frac{\partial T}{\partial\eta} + \frac{\partial^2 T}{\partial\eta^2}, \tag{3.62}$$

$$T(0,t) = 0, \qquad T(1,t) = 1, \tag{3.63}$$

$$\beta(1-R)\frac{\mathrm{d}R}{\mathrm{d}t} = -\left.\frac{\partial T}{\partial\eta}\right|_{\eta=0}. \tag{3.64}$$

We use standard finite differences to approximate the temperature derivatives as in (3.35). As in the spherical case, we can now write

$$T_i^{n+1} = 0, \qquad i = 1, \tag{3.65}$$

$$\hat{a}_i^n T_{i-1}^{n+1} + \hat{b}_i^n T_i^{n+1} + \hat{c}_i^n T_{i+1}^{n+1} = \hat{d}^n T_i^n, \qquad i = 2, \ldots, J-1, \tag{3.66}$$

$$T_i^{n+1} = 1, \qquad i = J, \tag{3.67}$$

which allows us to write down a matrix system that we solve at every time step n. We are able to determine the position of the melt front via the Stefan condition (3.64) using a three-point backward difference for the partial derivative, and taking the time derivative to be (3.39). The small time analysis leads to $R \approx 1 - 2\lambda t^{1/2}$, with $\lambda = \sqrt{1/(2\beta)}$.

Comparison of results

In Figure 3.3 we present the numerical and approximate solutions in the original domain for $\beta = 1$, 10. In this case all the heat balance methods are inaccurate for approximately $R < 0.3$. As expected the perturbation solution is poor for $\beta = 1$ and much more accurate when $\beta = 10$. In both cases the TIM is more accurate than the standard HBIM but neither is sufficiently accurate to justify their use.

In Figure 3.4 we show a comparison of the melt front predictions of the numerical solution (solid line) and the approximate solutions in the transformed domain for various β. The HBIM with $n = 2$ and perturbation solutions are shown as dash-dotted and dotted lines, respectively. At small times all solutions agree well, however as R decreases they begin to diverge. For the case where $\beta = 1$, shown in Figure 3.4a), we see that the HBIM and perturbation both present errors of about 10%. In Figure 3.4b) we present results for $\beta = 10$. Now the solutions are more accurate, with the same error of about 3.5%.

3.4 Newton cooling boundary condition

In practice a fixed temperature boundary condition is difficult to maintain; a fixed flux or Newton cooling condition is more physically realistic [87]. We now focus on the Newton cooling condition, which means using boundary condition (3.3b). Again, since we follow the methods of the previous section we omit most details.

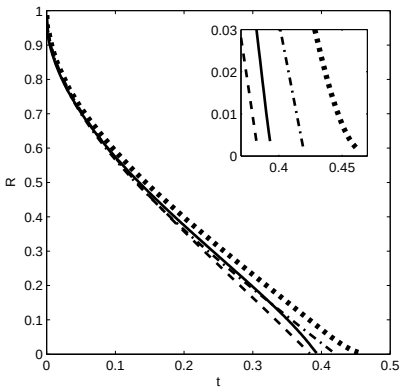

(a) $\beta = 1$.

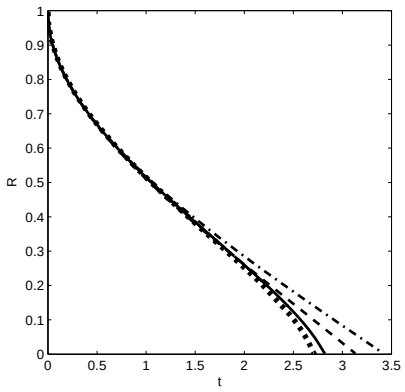

(b) $\beta = 10$.

Figure 3.3: Melting front evolution of a cylindrical particle in the original system for HBIM (dash-dotted), TIM (dashed), perturbation (dotted) and numerical (solid) solutions for various β.

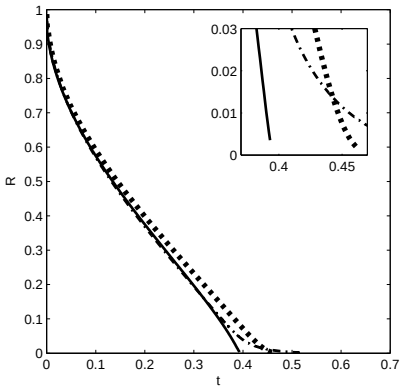

(a) $\beta = 1$.

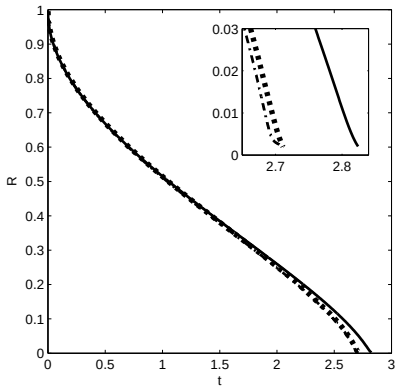

(b) $\beta = 10$.

Figure 3.4: Melting front evolution of a cylindrical particle in the transformed system for HBIM (dash-dotted), perturbation (dotted) and numerical (solid) solutions for various β.

3.4.1 Spherical problem

The problem is specified by (3.5)-(3.6), with $p = 2$, and the Newton cooling boundary condition (b). The polynomial to approximate the temperature T is given by (3.8), but now $c = 0$ and $b = \frac{\mathrm{Nu}(1-R)(a-1)+aR}{(1-\mathrm{Nu})(1-R)-n}$. The heat balance integral is given by (3.11), which

upon substituting for T from (3.8), with the corresponding c and b yields

$$\frac{\mathrm{d}}{\mathrm{d}t}\left[\frac{a}{1-R}\left(\frac{1}{2}-R\right)+\frac{1-R}{n+1}\left(\frac{[-\mathrm{Nu}-a(1-\mathrm{Nu})](1-R)+a}{(1-\mathrm{Nu})(1-R)-n}\right)+\frac{aR^2}{2(1-R)}\right]= \frac{n}{1-R}\left(\frac{[-\mathrm{Nu}-a(1-\mathrm{Nu})](1-R)+a}{(1-\mathrm{Nu})(1-R)-n}\right). \tag{3.68}$$

The second ODE is simply the Stefan condition (3.9).

Small time analysis

At small times R takes the form $R \approx 1-\lambda t$, see [87]. Substituting this into the Stefan condition determines the initial condition for $a \approx \beta\lambda^2 t$. To determine the initial conditions for the numerical solution we substitute both these small time solutions into equation (3.32), and upon letting $t \to 0$, we may write $u_{\eta\eta} \approx 0$. Applying the appropriate boundary conditions yields the small time form for u,

$$u(\eta,t) = -\frac{1-R}{(1-R)(1-\mathrm{Nu})-1}\eta. \tag{3.69}$$

Substituting the above expression for $u(\eta,t)$ into the Stefan condition (3.34) determines $\lambda = \mathrm{Nu}/\beta$.

In contrast to the previous solutions, since $\mathrm{Nu} = R_0 h/k$ there is a dependence on the initial size. The solution by the TIM shows that for $\mathrm{Nu} = 15$ and $\beta \in [1, 10]$, the optimal $n \in [2.7, 3.55]$. For $\mathrm{Nu} = 1$ there is a similarly large variation in n.

The leading and first order solutions for the perturbation are

$$T_0 = \frac{F_1}{r} + F_2, \tag{3.70}$$

$$T_1 = \frac{r^2}{6}\frac{\mathrm{d}F_1}{\mathrm{d}t} + \frac{r}{2}\frac{\mathrm{d}F_2}{\mathrm{d}t} + F_3 + \frac{F_4}{r}, \tag{3.71}$$

where

$$F_1 = \frac{\mathrm{Nu}}{R(1-\mathrm{Nu})+\mathrm{Nu}}, \tag{3.72}$$

$$F_2 = -\frac{\mathrm{Nu}R}{R(1-\mathrm{Nu})+\mathrm{Nu}}, \tag{3.73}$$

$$F_3 = \frac{1-\mathrm{Nu}}{\mathrm{Nu}}\left[\frac{1}{6}\frac{\mathrm{d}F_1}{\mathrm{d}t} + \frac{1}{2}\frac{\mathrm{d}F_2}{\mathrm{d}t} + F_4\right] - \frac{1}{2\mathrm{Nu}}\frac{\mathrm{d}F_1}{\mathrm{d}t} - \frac{1}{\mathrm{Nu}}\frac{\mathrm{d}F_2}{\mathrm{d}t}, \tag{3.74}$$

$$F_4 = -\frac{R}{6R(1-\mathrm{Nu})+6\mathrm{Nu}}\left[(\mathrm{Nu}R^2-2-\mathrm{Nu})\frac{\mathrm{d}F_1}{\mathrm{d}t} + 3(R\mathrm{Nu}-1-\mathrm{Nu})\frac{\mathrm{d}F_2}{\mathrm{d}t}\right]. \tag{3.75}$$

Substituting the first order approximation for T into the Stefan condition leads to

$$\frac{\mathrm{d}R}{\mathrm{d}t} = -\frac{3\mathrm{Nu}\left[(\mathrm{Nu}-1)R-\mathrm{Nu}\right]^2}{\left[3\mathrm{Nu}\left[(\mathrm{Nu}-1)R-\mathrm{Nu}\right]^3 - \epsilon\mathrm{Nu}(1-R)\left(1+\mathrm{Nu}+\mathrm{Nu}^2+(1+\mathrm{Nu}-2\mathrm{Nu}^2)R+(\mathrm{Nu}-1)^2R^2\right)\right]}. \quad (3.76)$$

Equation (3.76) can be solved via MATLAB's `ode45`.

For the transformed system, with $u = Tr$, the polynomial approximation is given by (3.8), with $c = 0$ and $b = \frac{\mathrm{Nu}(1-R)(a-1)+aR}{(1-\mathrm{Nu})(1-R)-n}$ and the heat balance integral is given by equation (3.28). The HBIM solution to the Stefan problem is now described by equation (3.27)for R, and substituting u into (3.28) we obtain an ODE for a. These two equations are subject to the initial conditions stated in the small time analysis. The TIM yields values for n that vary with β and Nu, $n \in [1.63, 1.95]$ (see Table 3.1).

The perturbation solution is the same in the transformed system as in the original. For the numerical solution we employ the same scheme defined in §3.3.1, the only difference is due to the boundary condition, so that for $i = J$, $\left(1-(1-\mathrm{Nu})(1-R^n)\Delta\eta\right)u_i^{n+1} - u_{i-1}^{n+1} = \mathrm{Nu}(1-R^n)\Delta\eta$.

In Figure 3.5 we show two results for $R(t)$ in the original system. As in the previous case we observe that for small β no approximation method is suitable. For $\beta = 10$ the perturbation solution provides reasonable accuracy, which obviously will improve as β increases. In Figure 3.6 we show results in the transformed system. Now the integral methods are clearly superior, providing good agreement in all examples. Interestingly, for the case $\beta = 1$, $\mathrm{Nu} = 1.5$ we can see from the inset that the standard HBIM with $n = 2$ is more accurate than the TIM, with $n = 1.95$, although both are obviously good approximations. The reason behind this is that the TIM is based on a global minimisation of the error in the temperature. This does not guarantee the most accurate temperature gradient at $r = R$. It seems that in this case the standard HBIM better approximates the gradient, $T_r(R,t)$, (at least as $R \to 0$) better than the TIM. However, as may be seen from the other three figures, in general the TIM is most accurate. Approximate values for n are provided in Table 3.1. Note, as $\mathrm{Nu} \to \infty$ the Newton cooling condition tends to the fixed boundary temperature boundary condition and so $n \approx 1.6$ (as predicted previously). For small Nu, $n \approx 1.92$. For simplicity we could take $n = 1.76$ for any Nu, β and find a good approximation. For better accuracy we could derive a function which moves smoothly between the limits (1.6, 1.95) as Nu moves between 0 and ∞.

		TIM exponent
Nu = 1.5	$\beta = 1$	1.95
	$\beta = 10$	1.89
Nu = 15	$\beta = 1$	1.68
	$\beta = 10$	1.63

Table 3.1: TIM exponent for different β and Nu in the transformed system.

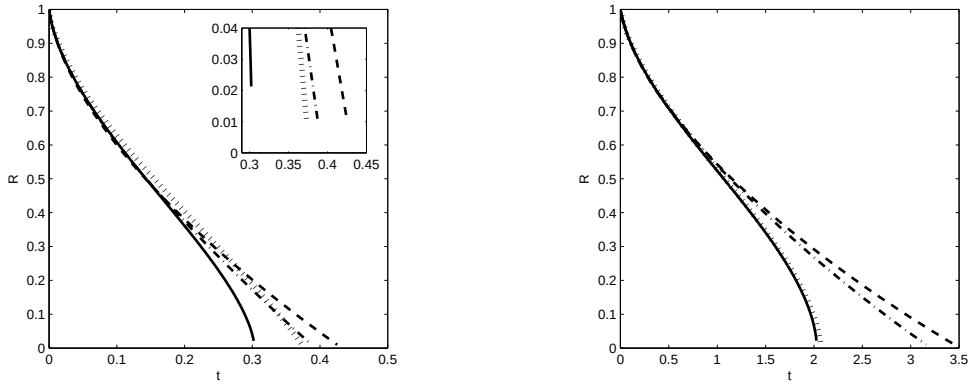

(a) $\beta = 1$, Nu = 15. **(b)** $\beta = 10$, Nu = 15.

Figure 3.5: Melting front evolution of a spherical particle in the original system for HBIM (dash-dotted), TIM (dashed), perturbation (dotted) and numerical (solid) solutions for various β and Nu.

3.4.2 Cylindrical problem

Here we follow the method of §3.3.2. In the original coordinate system we assume that the temperature profile has the form (3.8), with $c = 0$ and $b = \frac{(1+\mathrm{Nu}-\mathrm{Nu}R)a-\mathrm{Nu}(1-R)}{\mathrm{Nu}R-\mathrm{Nu}-n}$. The heat balance integral may be expressed as (3.41). We close the system by applying (3.8) to the Stefan condition. Assuming $R \approx 1 - \lambda t$ at small times, the Stefan condition leads to $a(0) \approx \beta\lambda^2 t$, and taking the limit $t \to 0$ in the HBI yields $\lambda = \mathrm{Nu}/\beta$. Finally, the best n is chosen to minimise the error function (3.43) at the final times. This gives $n \in [2.19, 2.62]$ as the optimal choice for $\beta = 1$, 10, Nu = 15.

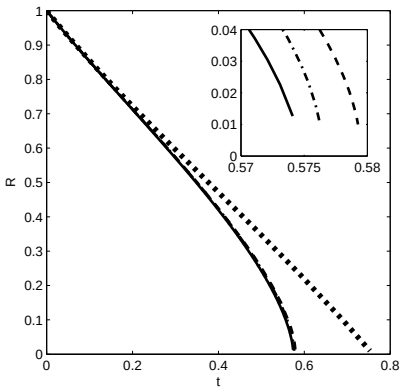

(a) $\beta = 1$, $\mathrm{Nu} = 1.5$.

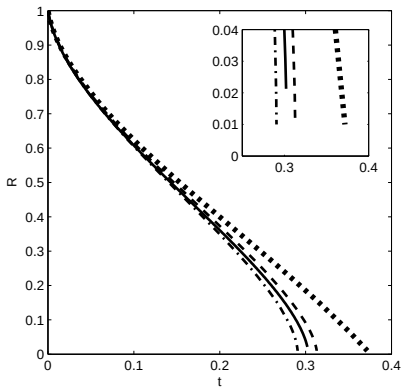

(b) $\beta = 1$, $\mathrm{Nu} = 15$.

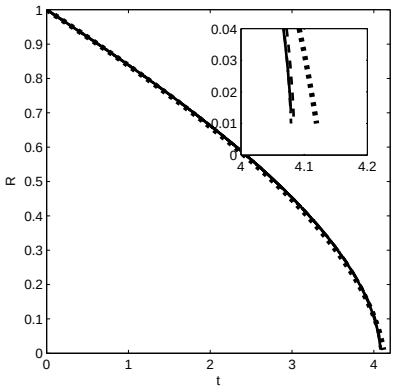

(c) $\beta = 10$, $\mathrm{Nu} = 1.5$.

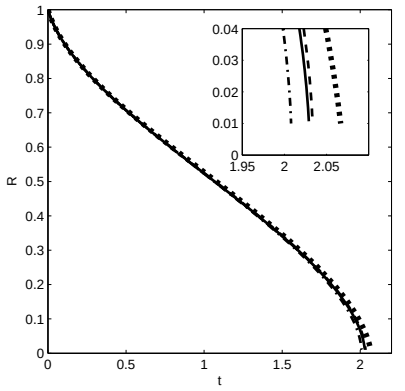

(d) $\beta = 10$, $\mathrm{Nu} = 15$.

Figure 3.6: Melting front evolution of a spherical particle in the transformed system for HBIM (dash-dotted), TIM (dashed), perturbation (dotted) and numerical (solid) solutions for various β and Nu.

The leading and first order perturbation solutions are

$$T_0(r,t) = F_1(t) + F_2(t)\ln(r), \tag{3.77}$$

$$T_1(r,t) = F_3(t)\ln(r) + \frac{r^2}{4}\frac{\mathrm{d}F_1}{\mathrm{d}t} + \frac{r^2}{4}\frac{\mathrm{d}F_2}{\mathrm{d}t}\ln(r) - \frac{r^2}{4}\frac{\mathrm{d}F_2}{\mathrm{d}t} + F_4, \tag{3.78}$$

where

$$F_1(t) = \frac{\mathrm{Nu}\ln(R)}{\mathrm{Nu}\ln(R) - 1}, \tag{3.79}$$

$$F_2(t) = \frac{\mathrm{Nu}}{1 - \mathrm{Nu}\ln(R)}, \tag{3.80}$$

$$F_3(t) = -\frac{1}{4}\frac{\left(R^2\ln(R)\,\mathrm{Nu}^2 + \left(-\mathrm{Nu}-\mathrm{Nu}^2\right)R^2 + 2\,\mathrm{Nu} + \mathrm{Nu}^2 + 2\right)\mathrm{Nu}}{R\left(-1+\mathrm{Nu}\,\ln(R)\right)^3}\frac{\mathrm{d}R}{\mathrm{d}t}, \tag{3.81}$$

$$F_4(t) = \frac{1}{4}\frac{\mathrm{Nu}\,\left(\left(2+2\,\mathrm{Nu}+\mathrm{Nu}\,R^2+\mathrm{Nu}^2\right)\ln(R) - R^2\,(1+\mathrm{Nu})\right)}{R\left(-1+\mathrm{Nu}\,\ln(R)\right)^3}\frac{\mathrm{d}R}{\mathrm{d}t}. \tag{3.82}$$

The melting front is given by

$$\frac{\mathrm{d}R}{\mathrm{d}t} = \frac{4\mathrm{Nu}\left(\ln(R)\,\mathrm{Nu}-1\right)^2}{\left(4\mathrm{Nu}^3\ln(R)^3 - 12\mathrm{Nu}^2\ln(R)^2 + (+12\mathrm{Nu})\ln(R) - 4\right)R}. \tag{3.83}$$

For the transformed system, given by the change of coordinates (3.47), the outer boundary condition is $\left.\frac{\partial u}{\partial \rho}\right|_{\rho=0} = \tau\lambda(1-u(0,\tau))$. The polynomial approximation is given by

$$u(\rho,\tau) = c + \tau\mathrm{Nu}(1-c)\rho - \left(c+\tau\mathrm{Nu}(1-c)\right)\rho^2. \tag{3.84}$$

Then the heat balance integral yields

$$\frac{\mathrm{d}c}{\mathrm{d}\tau} = \frac{-2\left(\tau\mathrm{Nu}(c-1)-2c\right)^2\mathrm{e}^{-2\tau}\left(1/2+\tau^2-\tau\right)\mathrm{e}^{2\tau} + \left(\left(\tau\mathrm{Nu}-2\right)c-\tau\,\mathrm{Nu}\right)^2\mathrm{e}^{-2\,\tau} + 8\beta\tau^3\left(\tau\mathrm{Nu}(c-1)-c\right)}{\left(-\tau\mathrm{Nu}+\tau\mathrm{Nu}c-2c\right)\left(\left(1+\tau^2\mathrm{Nu}+(-2-\mathrm{Nu})\,\tau\right)\mathrm{e}^{2\tau}-1+(2+\mathrm{Nu})\,\tau^2+\tau\mathrm{Nu}\right)\mathrm{e}^{-2\tau}\tau}. \tag{3.85}$$

The small time solution is $c(0) = 1-2\beta\lambda^2$. Now (3.85) is solved numerically using an ODE solver in MATLAB over the range $[0,\,-\infty]$. The corresponding melt front is simply $R = e^{\tau}$. We use (3.57) to convert the interval from τ back to t. For the perturbation solution, we find that the melt front is given by (3.83).

The numerical scheme is the one described in §3.3.2 but equation (3.67) becomes

$$T_J^{n+1} = \left(\mathrm{Nu}(1-R^n)\Delta\eta + 1\right)T_i^{n+1} - T_{i-1}^{n+1} = \mathrm{Nu}(1-R^n)\Delta\eta. \tag{3.86}$$

3.5 Conclusion

The goal of this paper was to improve the accuracy of the HBIM applied to Stefan problems in spherical and cylindrical geometries. To do this we analysed the standard form and the optimised form (TIM), in the original and a transformed co-ordinate system, subject to fixed temperature and Newton cooling boundary conditions. The large Stefan number perturbation solution was also calculated to first order since this is the most common way to approximate solutions to Stefan problems. The accuracy was determined by comparison of the predicted melt front position with a numerical solution for two values of the Stefan

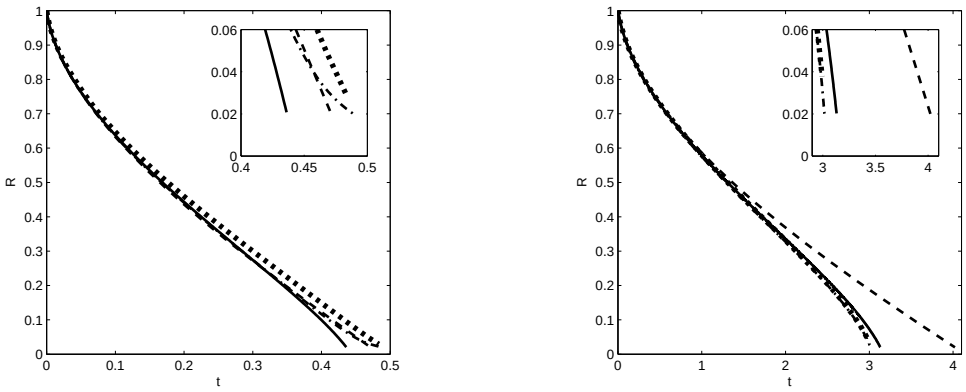

(a) $\beta = 1$, Nu $= 15$. **(b)** $\beta = 10$, Nu $= 15$.

Figure 3.7: Melting front evolution of a cylindrical particle for HBIM in the transformed system (dash-dotted), TIM in the original system (dashed), perturbation (dotted) and numerical (solid) solutions for various β and Nu $= 15$.

number $\beta = 1, 10$. The upper limit for β was chosen since it is a typical maximum value for practical melting problems [3].

First we considered melting due to a fixed temperature boundary condition. For the spherical problem all solutions in the original domain were inaccurate for small β. For large β only the perturbation solution was accurate. However, when the temperature variable was changed to $u = rT$ the solutions improved in accuracy. In particular the TIM gave the most accurate solutions for the β values tested. Even when $\beta = 10$, when we expect the perturbation solution to have an accuracy of $\mathcal{O}(10^{-2})\%$ the TIM was significantly more accurate. The expression for the temperature with the fixed temperature boundary condition takes the form

$$u = a\left(\frac{r-R}{1-R}\right) + b\left(\frac{r-R}{1-R}\right)^n, \tag{3.87}$$

where $b = 1 - a$. For the standard HBIM $n = 2$. For the TIM $n \in [1.55, 1.65]$ varies slightly with β. However, choosing the average value $n = 1.6$ provides more accurate solutions than the other methods. Consequently when studying spherical Stefan problems, with a fixed temperature boundary condition we recommend transforming the temperature variable $T = u/r$ where u is given by (3.87) and $n = 1.6$.

With a Newton cooling condition the conclusions are similar. Firstly, the temperature

must be transformed to $u = rT$. The relation between a and b is more complex and with the TIM the exponent varies with both β and $\mathrm{Nu} = hR_0/k$. For small Nu we found good accuracy with the average $n = 1.92$. For larger Nu (here we tested Nu= 15) we found a smaller value $n = 1.65$, which is obviously tending to the fixed temperature limit $n = 1.6$ (corresponding to $\mathrm{Nu} \to \infty$).

In the case of cylindrical symmetry the results were not so satisfactory. Firstly, the temperature transformation was of no use, instead we used a boundary fixing transformation, which complicated the governing heat equation. Secondly, the TIM proved too complex to be of practical use or appeal. Thirdly, in general accuracy was poor for both boundary conditions. From this part of the study it is difficult to make a conclusive statement. When $\beta = 1$, for a fixed temperature boundary condition the TIM works best in the original system, for the cooling condition it is more accurate than the HBIM and perturbation calculated in the transformed system. For large β it is the worst, while the perturbation is reasonably accurate for the values of Nu examined.

In conclusion then, it appears that the TIM can be used with great accuracy in spherically symmetric melting problems, provided the temperature transformation $u = rT$ is employed. In the cylindrical problem the results are less conclusive and different methods work better for different parameter values. In this case it is hard to make a single recommendation. However, it is possible that a different transformation, either of the temperature or co-ordinates, could change this conclusion.

4 | Nanoparticle melting with variable latent heat and melt temperature

---

H. Ribera, T. G. Myers

A mathematical model for nanoparticle melting with size-dependent latent heat and melt temperature

Microfluidics and Nanofluidics, 20, 147 (2016)

Impact factor: 2.537

Abstract

In this paper we study the melting of a spherical nanoparticle. The model differs from previous ones in that a number of features have been incorporated to match experimental observations. These include the size dependence of the latent heat and a cooling condition at the boundary (as opposed to the fixed temperature condition used in previous studies). Melt temperature variation and density change are also included. The density variation drives the flow of the outer fluid layer. The latent heat variation is modelled by a new relation, which matches experimental data better than previous models. A novel form of Stefan condition is used to determine the position of the melt front. This condition takes into account the latent heat variation, the energy required to create new surface and the kinetic energy of the displaced fluid layer. Results show that melting times can be

significantly faster than predicted by previous theoretical models, for smaller particles this can be around a factor 3. This is primarily due to the latent heat variation. The previously used fixed temperature boundary condition had two opposing effects on melt times: the implied infinite heat transfer led to faster melting but also artificially magnified the effect of kinetic energy, which slowed down the process. We conclude that any future models of nanoparticle melting must be based on the new Stefan condition and account for latent heat variation.

4.1 Introduction

Nanoparticles are currently the focus of extensive research due to their unique properties and their applications in many fields. They are used in medicine, for both diagnosis and drug delivery [67, 114], in biology [93] and in optics [1]. They are also used to increase efficiency in energy production, in the creation of new optoelectronic devices [102] and in materials with modified properties [23, 39]. In many of these applications high temperatures are involved, so it is important to understand how nanoparticles respond to heat and how they behave if a phase change occurs.

Nanoparticles have a high ratio of surface to volume atoms, which makes them behave differently to their bulk counterparts: examples include enhanced mechanical strength; enhanced solar radiation absorption and superparamagnetism. A well-known nanoscale property is the decrease in the phase change temperature with particle size. Buffat and Borel [13] reported a decrease of approximately 500 K below the bulk melt temperature (approximately 60%) for gold nanoparticles with radii a little above 1 nm. Decreases of 70 K and 200 K have been reported for tin and lead nanoparticles [20]. The variation in surface tension with radius has been approximated by the relation $\sigma_{sl} = \sigma^*_{sl}(1 - 2\delta/R)$ [104], where σ_{sl} is the surface tension, the star denotes the bulk value, δ is termed the Tolman length and R is the particle radius. The Tolman length is typically very small: in this paper we will use data for tin with $\delta = 0.373$ nm. This value leads to a decrease in surface tension of approximately 15% from the bulk value for a particle of radius 5 nm and 1% for a particle of radius 100 nm.

Molecular dynamics (MD) simulations and experiments have also demonstrated a de-

crease in latent heat with a decrease in radius. Lai *et al.* [50] presented the first calorimetry measurements of the melting process of nanometer-sized tin particles, ranging from $5 - 50$ nm in diameter. They found a reduction of up to 70% from the bulk latent heat for the smaller sized particles. Jiang *et al.* [46] improved the measurement technique to find even greater reductions. Using a thin-film scanning calorimetry technique similar behaviour was observed by Zhang *et al.* [117] in a study of the melting behaviour of $0.1 - 10$ nm-thick discontinuous indium films made from ensembles of nanostructures. In the MD studies of Bachels *et al.* [5] the melt temperature of 1.4 nm radius tin particles is 25% lower than the bulk value while the latent heat is 45% lower. Ercolessi *et al.* [25], Lim *et al.* [53] and Delogu [22] have carried out MD studies on gold, lead and copper clusters, all showing the same qualitative behaviour.

The mathematical modelling of phase change is termed the Stefan problem. Theoretical studies of Stefan problems involve a number of restrictive assumptions, made primarily for mathematical convenience, and so they really only apply to idealised situations. Standard assumptions include constant thermophysical properties in each phase and the same density in both phases, constant phase change temperature, latent heat and surface tension and also a fixed temperature boundary condition. A number of these assumptions are discussed in [3, Table 1.1]. Melting point depression (where the melt temperature decreases with particle size) was considered in the mathematical studies of [6, 7, 30, 31, 60, 111, 110]. McCue *et al.* [60] propose this as the primary reason for the experimentally observed sudden disappearance of nanoparticles. In all of these studies the outer boundary temperature was taken to be a constant (greater than the melt temperature). Font and Myers [31] included density variation and melting point depression in their model. They demonstrated that melt times increased with density variation and explained this through the energy required to move the liquid. They also demonstrated that a large contribution to this extra energy term came at the beginning of the process, as a result of the unrealistic fixed temperature boundary condition. The effect was most noticeable for small particles, but even as the size was allowed to tend to infinity there was still a 15% discrepancy (for gold at least) from the constant density model results. The thesis of Back [8, §7.1-7.4] confirms this large discrepancy. It also includes a section where the latent heat employed in the standard energy balance is replaced by a size dependent function, using a formula taken from [50]. This leads

to a decrease in melt times. A converse problem, growth of nanoparticles is considered in [24]. They investigate an ice-water system and use the standard Gibbs-Thomson relation, a single value for density, a fixed temperature boundary condition and a Stefan condition taken from models of macroscale melting. Growth and melting of nanowires is considered in [28]. They also employ the standard Gibbs-Thomson relation and a constant density, at the boundary they consider both fixed temperature and cooling conditions. Their Stefan condition accounts for the energy required to make new surface. A significant feature of this work is that it demonstrates that solidification from the outer boundary is a faster process than melting

Experiments and MD simulations have made it clear that both melt temperature and latent heat vary significantly during melting, with latent heat often showing the greatest variation. The surface tension variation is less noticeable. In practice the boundary temperature cannot be instantaneously raised to some constant value. Consequently in this paper we will attempt to extend the previous works to produce a more realistic melting model. Specifically, we will incorporate the variation of latent heat, melt temperature and density and impose a physically realistic boundary condition. One final novelty in this work concerns the form of Stefan condition. Previous studies on nanoparticle melting and the solidification of supercooled melts [72] use an energy balance (the Stefan condition) at the interface between the two phases which is based on an implicit assumption that the latent heat is released at the bulk melt temperature. Obviously this is not correct. In [70] a new form of Stefan condition is derived which involves an "*effective latent heat*", which is the sum of the size dependent latent heat (released at the appropriate melt temperature), the kinetic energy and the energy required to make new surface.

In the following section we will discuss the latent heat and propose a model to describe the variation with particle size. This will then be used in the development of the mathematical model, in Section 4.3. In Section 4.4 we apply an approximate solution method, and verify the accuracy by comparison with the full numerical solution. In the results section we demonstrate the effect of the various new components of the model which, for small particles, can lead to a factor three change in the predicted melt times. All equations are based on the validity of the continuum assumption. This has been discussed in detail in [30, 71]. For phase change the limit of validity appears to be around 2-5 nm, depending on

the material.

4.2 Latent heat variation

The size-dependence of a number of physical properties has often been modelled by functions involving $1/R$. These include the surface tension, the Gibbs-Thomson relation for the melt temperature and the Ostwald-Freundlich equation for a particle's solubility (it is also quoted for surface tension). Consequently, when investigating size-dependent properties at the nanoscale it is standard to start with functions involving $1/R$. Recent investigations into the latent heat variation have led to the following relations.

Lai *et al.* [50] suggest

$$L_m = L_m^* \left(1 - \frac{\delta_t}{R}\right)^3, \tag{4.1}$$

where L_m^* is the bulk latent heat. The constant δ_t was chosen to provide the best fit to their experimental data for melt temperature, for tin they found $\delta_t = 16$ Å. Xiong *et al.* [112] propose

$$L_m = L_m^* \left[1 + \left(1 + \frac{3R_G T_m^*}{2L_m^*}\right)\left(\frac{\pi N_A d^4 T_m^* b}{L_m^*}\right)\frac{1}{2R}\right], \tag{4.2}$$

where T_m^* is the bulk melt temperature, R_G is the gas constant, N_A Avogadro's number, d the atom diameter and b a negative constant that acts as a fitting parameter. Shin *et al.* [98] model the latent heat by

$$L_m = L_m^* - \Delta h_s + \frac{2\sigma_{sl}}{\rho_s R} - \frac{2\sigma_{lv}(\rho_s - \rho_l)}{\rho_l \rho_s (R + \delta_t)}, \tag{4.3}$$

where Δh_s is the change in specific enthalpy, ρ_s, ρ_l are the density of the solid and liquid, σ_{lv} is the liquid-vapour surface tension. The change of the specific enthalpy of the solid is

$$\begin{aligned}\Delta h_s =& \frac{1}{\rho_s}\left(\frac{2\sigma_{sl}}{R} + \frac{2\sigma_{lv}}{R+\delta_t}\right) + \frac{3\sigma_{sl}^*}{\rho_s R} - \frac{12\sigma_{sl}^*\delta}{\rho_s R^2} \\ & - T\left(\left(\frac{2\sigma_{sl}}{R} + \frac{2\sigma_{lv}}{R+\delta_t}\right)\frac{d(1/\rho_s)}{dT} + \frac{3}{\rho_s R}\frac{d\sigma_{sl}^*}{dT} - \frac{12\delta}{\rho_s R^2}\frac{d\sigma_{sl}^*}{dT}\right).\end{aligned} \tag{4.4}$$

For tin nanoparticles they define $\sigma_{sl} = 0.11\sigma_{lv}$ where σ_{sl} is defined by the Tolman relation with $\delta = 3.73 \times 10^{-10}$m and they take δ_t from [50].

In Figure 4.1 we compare the predictions of these relations with experimental data for the latent heat of tin, taken from Lai *et al.* [50]. The necessary parameter values are provided

in Table 4.1. In Xiong *et al.* [112] the fitting parameter b is calculated to provide a best fit with melt temperature data for different metals. They do not give a value for tin, so we performed a least-squares fit to the latent heat data, hence our curve for latent heat variation using their formula is closer to the experimental data than theirs. We determined a value $b = -6.65 \times 10^{30} (\text{m K s}^2)^{-1}$, this is of the order of their quoted values for five other metals. The circles in the figure represent the experimental data, the dashed line that of eq. (4.1), the dotted line that of eq. (4.2) and the dash-dot line that of eq. (4.3). The comparisons for melt temperature variation shown in the graphs of [50, 112] demonstrate excellent agreement with the data, while the latent heat representation is poor, only matching the data points for the three smallest particles. In Figure 4.1 this poor agreement may also be seen. In [98] the results presented for latent heat show good agreement with data, unfortunately we have been unable to reproduce this agreement.

Material	T_m^* (K)	L_m^* (J/kg)	c_s/c_l (J/kg·K)	k_s/k_l (W/m·K)	ρ_s/ρ_l (kg/m^3)	σ_{sl}^* (N/m)
Tin	505	58500	230/268	67/30	7180/6980	0.064

Table 4.1: Thermodynamical parameter values for tin, data taken from [5, 34, 51, 103, 50, 95, 98].

The three previous theoretical models involve a single fitting parameter and so should exhibit some agreement with the data. However, a single fitting parameter restricts the ability of the model to accurately approximate data over a large range. The form of the models also ensures $L_m \to L_m^*$ as $R \to \infty$. A problem common to them all is the speed of decay to the bulk value. For sufficiently large R they may all be expressed in the form

$$L_m(R) = L_m^* \left(1 - \frac{A_1}{R} + \frac{A_2}{R^2} + \cdots\right) \tag{4.5}$$

for various values of A_i. It would appear that this form of polynomial in $1/R$ does not exhibit the correct limiting behaviour. A particularly worrying feature of this observation is that the bulk value is the most reliable one, and the models clearly do not approach the only truly reliable data point correctly. Motivated by the inaccuracy of these models we propose a form that permits more rapid decay for large R,

$$L_m = L_m^* \left(1 - e^{-C\frac{R}{R_c}}\right), \tag{4.6}$$

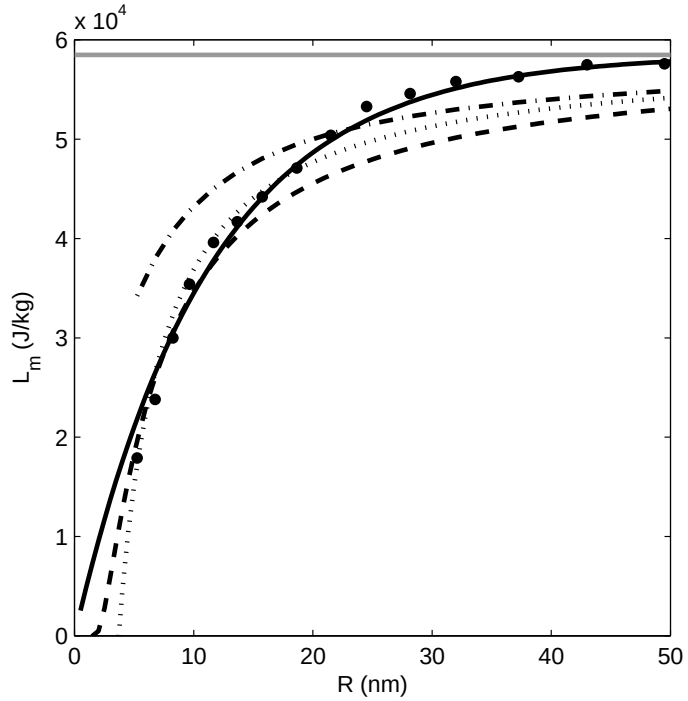

Figure 4.1: Latent heat for a tin nanoparticle as a function of the radius. Lai *et al.* model (equation (4.1)), dashed line. Model proposed by Xiong *et al.* [112] (equation (4.2)), dotted line. Shin *et al.* [98] (equation (4.3)), dash-dotted line. Exponential fit proposed in this paper (equation (4.6)), solid line. Dots are experimental data of Lai *et al.* [50]. Grey horizontal line indicates bulk value.

where the constant C is our fitting parameter. To ensure C takes reasonable values we also introduce the capillary length $R_c = \sigma^*_{sl}/(\rho_s L^*_m)$. The solid curve shown on Figure 4.1 represents our exponential relation, where the value $C = 0.0133$ has been used. This was obtained via a least-squares fit to the data. It is quite clear that the exponential relation is a significant improvement on the other models. For large radii it is the only result that comes close to the experimental data. Below 15 nm three models, the current exponential, Lai's and Xiong's all provide a reasonable fit. Only below around 8 nm does our model show a noticeable deviation from the data. In the following sections we will model nanoparticle melting with sizes varying between 2-100 nm. Consequently we will employ our exponential relation to describe latent heat variation, since this appears to be the only accurate relation for this range of particle radii.

4.3 Mathematical model

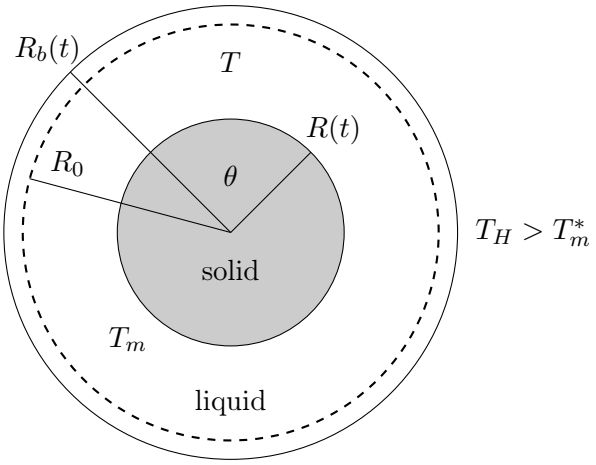

Figure 4.2: Sketch of the problem.

The physical situation considered in this section follows the standard form described in previous papers [30, 31, 60, 111, 110]. A nanoparticle with initial radius R_0 is subjected to an external heat source which results in melting. The melting begins at the outer boundary and progresses inwards until the whole particle has melted. The solid-liquid interface is denoted $R(t)$. Since the liquid and solid densities are different the outer boundary moves, this is denoted $R_b(t)$, where $R_b(0) = R_0$. A sketch of this situation is presented in Figure 4.2. The temperature in each phase is described by the standard heat equations

$$\rho_l c_l \left(\frac{\partial T}{\partial t} + v \frac{\partial T}{\partial r} \right) = k_l \frac{1}{r^2} \frac{\partial}{\partial r} \left(r^2 \frac{\partial T}{\partial r} \right), \qquad R(t) < r < R_b(t), \tag{4.7}$$

$$\rho_s c_s \frac{\partial \theta}{\partial t} = k_s \frac{1}{r^2} \frac{\partial}{\partial r} \left(r^2 \frac{\partial \theta}{\partial r} \right), \qquad 0 < r < R(t), \tag{4.8}$$

where T and θ denote the temperature in the liquid and solid respectively, ρ_i, c_i and k_i are the densities, the specific heats and the conductivities respectively. The index notation $i = s, l$ refers to the solid or liquid phases. The velocity v at which heat is advected in equation (4.7) is given by [31]

$$v = -\frac{R^2}{r^2} (\rho - 1) \frac{dR}{dt}, \tag{4.9}$$

where $\rho = \rho_s / \rho_l$.

The heat equation in the solid must be solved over the region $0 \leq r \leq R(t)$. The position of the melt front, $R(t)$, is determined by the energy balance

$$\left(\rho_s \left[L_m + \frac{v(R,t)^2}{2}\right] + \frac{2\sigma_{sl}^*}{R}\right)\frac{dR}{dt} = k_s \left.\frac{\partial \theta}{\partial r}\right|_{r=R} - k_l \left.\frac{\partial T}{\partial r}\right|_{r=R}. \tag{4.10}$$

This is the Stefan condition derived in [70]. The terms in the brackets on the left hand side represent the (time dependent) latent heat, the kinetic energy and the energy required to create new surface. The rate at which this energy is released, dR/dt, is balanced by the energy conducted through the solid and liquid. Note, the factor in brackets on the left hand side differs significantly to the one used in previous studies on nanoparticle melting, $\rho_s \left(L_m^* + (c_l - c_s)(T_m - T_m^*) + v^2/2\right)$. This latter version of the effective latent heat has been taken as standard when modelling nanoparticle melting and the solidification of supercooled materials (with the exception of [24] who use $\rho_s L_m^*$). It is derived in [27], where they specify latent heat release at the bulk melt temperature T_m^*. Obviously latent heat is released at the appropriate size-dependent melt temperature. In [70] it is shown that the previous form of effective latent heat leads to errors (when compared to experimental data) up to a factor three for particles of the order 5 nm. Hence in the following analysis we employ the relation (4.10).

The governing equations are subject to the boundary conditions

$$-k_l \left.\frac{\partial T}{\partial r}\right|_{r=R_b} = h(T(R_b,t) - T_H), \quad T(R,t) = \theta(R,t) = T_m(t), \quad \theta_r(0,t) = 0\,. \tag{4.11}$$

Note, at the outer boundary we specify a Newton cooling condition which states that the energy transferred to the particle is proportional to the temperature difference between the particle surface and the surrounding material. This is more physically realistic than the fixed temperature boundary condition, $T(R_b,t) = T_H$, which leads to an initial infinite boundary velocity. Following [31] we set the initial solid temperature to the melt temperature $\theta(r,0) = T_m(0)$. This means that we avoid the issue of any initial heating up period, however, as we will see when the problem is non-dimensionalised heat flow is fast in comparison to the melting time-scale so the imposition of any other temperature (below the melt temperature) would have little effect on the results.

The position of the outer boundary may be determined via the velocity relation. Setting $v(R_b) = dR_b/dt$ in equation (4.9) and integrating gives

$$R_b = \left(R_0^3 \rho - R^3(\rho - 1)\right)^{1/3}, \tag{4.12}$$

where $R(0) = R_b(0) = R_0$.

The fixed temperature boundary condition of previous studies is the limit of equation (4.11a) as the heat transfer coefficient $h \to \infty$. Of course this cannot be achieved physically and there exists a limit to the heat transfer beyond which the material would be vaporised. To permit comparison with previous models we therefore choose the highest possible value for h which still permits thermodynamic stability. To do this we set

$$h_{\max} = \frac{q_{\max}}{\Delta T}, \qquad q_{\max} = \rho_s u v_s, \tag{4.13}$$

where u is the internal energy and v_s is the speed of second sound in the material, see [28, 47], ΔT is the temperature scale, here we set $\Delta T = T_H - T_m^*$. A typical order of magnitude for $h_{\max}$ is found by first noting that the speed of second sound may be related to the phonon velocity $v_s = v_p/\sqrt{3}$. We follow [118] and take $v_p = \sqrt{B/\rho_s} \approx 2842\text{m/s}$ (B is the bulk modulus). The internal energy is given approximately by the enthalpy (this is valid under constant pressure, constant density and zero velocity), $u = c_s \Delta T$, consequently $h_{\max} = \rho_s c_s v_s \approx 4.7 \times 10^9$ W/m^2 K. We will use this value in the following calculations since it will give the closest, physically achievable, comparison to previous fixed temperature results.

The melt temperature $T_m(t)$ may be approximated by the Gibbs-Thomson equation [101],

$$T_m(t) = T_m^* \left(1 - \frac{2\sigma_{sl}^*}{\rho_s L_m^* R}\right). \tag{4.14}$$

Note, we use the bulk value σ_{sl}^* since the variation of surface tension is small (in comparison to the latent heat and melt temperature). This could be an obvious extension in subsequent work. Substituting the parameters from Table 4.1 into (4.14) we observe that $T_m(t)$ becomes negative for $R < 0.31$ nm. Taking into account that our model is valid for R where continuum theory holds, that is, $R > 2-5$ nm, the use of this version of the Gibbs-Thomson equation does not represent a problem.

We now scale the model using the dimensionless variables

$$\begin{gathered} \hat{T} = \frac{T - T_m^*}{\Delta T}, \quad \hat{\theta} = \frac{\theta - T_m^*}{\Delta T}, \quad \hat{T}_m = \frac{T_m - T_m^*}{\Delta T}, \quad \hat{L}_m = \frac{L_m}{L_m^*}, \\ \hat{r} = \frac{r}{R_0}, \quad \hat{R} = \frac{R}{R_0}, \quad \hat{R}_b = \frac{R_b}{R_0}, \quad \hat{t} = \frac{k_l}{\rho_l c_l R_0^2} t. \end{gathered} \tag{4.15}$$

This results in the following system (where we have immediately dropped the hat notation)

$$\frac{\partial T}{\partial t} - (\rho - 1)\frac{R^2}{r^2}\frac{dR}{dt}\frac{\partial T}{\partial r} = \frac{1}{r^2}\frac{\partial}{\partial r}\left(r^2\frac{\partial T}{\partial r}\right), \qquad R(t) < r < R_b(t), \tag{4.16}$$

$$\frac{\partial \theta}{\partial t} = \frac{k}{\rho c}\frac{1}{r^2}\frac{\partial}{\partial r}\left(r^2\frac{\partial \theta}{\partial r}\right), \qquad 0 < r < R(t), \tag{4.17}$$

where $R_b = \left(\rho - R^3(\rho - 1)\right)^{1/3}$ and $R_b(0) = R(0) = 1$. The boundary conditions are

$$\left.\frac{\partial T}{\partial r}\right|_{r=R_b} = \Lambda(1 - T(R_b, t)) \ , \qquad T(R,t) = \theta(R,t) = T_m(t) = -\frac{\Gamma}{R} \ , \qquad \theta_r(0,t) = 0, \tag{4.18}$$

where $\Lambda = q_{max}R_0/(\Delta T k_l)$, $\Gamma = \alpha T_m^*/\Delta T$ and $\alpha = 2\sigma_{sl}^*/(\rho_s L_m^* R_0)$. The initial temperature becomes $\theta(r,0) = -\Gamma$. The Stefan condition is

$$\rho\beta\left[L_m(t) + \frac{\alpha}{R}\right]\frac{dR}{dt} + \gamma\left(\frac{dR}{dt}\right)^3 = k\left.\frac{\partial \theta}{\partial r}\right|_{r=R} - \left.\frac{\partial T}{\partial r}\right|_{r=R}, \tag{4.19}$$

where the Stefan number $\beta = L_m^*/(c_l\Delta T)$ and $\gamma = (1-\rho)^2\rho_s\kappa_l^3/(2\Delta T k_l R_0^2)$, where $\kappa_l = k_l/(\rho_l c_l)$ is the thermal diffusivity.

The Stefan number, β, depends on the temperature scale of the process: it is large for a small temperature variation, and small for a large temperature variation. As we are working at the nanoscale, the Stefan number is typically large since, due to melting point depression, only a very small increase above the melt temperature is sufficient to induce complete particle melting.

4.4 Perturbation solution

The beauty of an analytical or approximate analytical solution is that it makes clear the factors driving a physical process in a manner that cannot be achieved by a numerical solution. Consequently we now follow previous researchers in using a perturbation method based on the large Stefan number.

If we consider equation (4.19) and divide through by β then we find $dR/dt \approx 0$ (for sufficiently large β). Physically this tells us that the large Stefan number solution corresponds to slow melting (slow compared to the heat transfer in the material). Since we wish to focus on the melting we therefore rescale time via $\tau = \epsilon t$ where $\epsilon = 1/\beta \ll 1$. The Stefan condition may now be written

$$\rho\left[L_m(t) + \frac{\alpha}{R}\right]\frac{dR}{d\tau} + \gamma\epsilon^3\left(\frac{dR}{d\tau}\right)^3 = k\left.\frac{\partial \theta}{\partial r}\right|_{r=R} - \left.\frac{\partial T}{\partial r}\right|_{r=R}. \tag{4.20}$$

With the new time-scale the time derivatives in the two heat equations, equations (4.16, 4.17), are now multiplied by ϵ. So now, on the time-scale of melting, the heat equations are close to a pseudo-steady state. It is not a true steady-state since the boundary conditions still depend on time. Physically this means that as the melting proceeds, the temperature adjusts so rapidly that it appears to take the appropriate steady-state form. This is the justification for our earlier statement that the initial solid temperature does not have a significant effect on the final results.

To solve the system we can look for an expansion for the temperatures of the form $T = T_0 + \epsilon T_1 + \mathcal{O}(\epsilon^2)$. At order ϵ^0 we find the temperature in the liquid is described by

$$0 = \frac{1}{r^2}\frac{\partial}{\partial r}\left(r^2\frac{\partial T_0}{\partial r}\right) , \qquad \left.\frac{\partial T_0}{\partial r}\right|_{r=R_b} = \Lambda(1 - T_0(R_b,\tau)) , \quad T_0(R,\tau) = -\frac{\Gamma}{R} , \tag{4.21}$$

At order ϵ^1 the temperature is described by

$$\begin{aligned} &\frac{\partial T_0}{\partial \tau} - (\rho-1)\frac{R^2}{r^2}\frac{dR}{d\tau}\frac{dT_0}{dr} = \frac{1}{r^2}\frac{\partial}{\partial r}\left(r^2\frac{\partial T_1}{\partial r}\right) , \qquad \left.\frac{\partial T_1}{\partial r}\right|_{r=R_b} = -\Lambda T_1(R_b,\tau) , \\ &T_1(R,\tau) = 0 . \end{aligned} \tag{4.22}$$

The appropriate solution is

$$T_0(r,\tau) = F_1(\tau) + \frac{F_2(\tau)}{r}, \tag{4.23}$$

$$T_1(r,\tau) = \frac{r^2}{6}\frac{dF_1}{d\tau} + \frac{r}{2}\frac{dF_2}{d\tau} - \frac{F_3(\tau)}{r} + \frac{R^2 R_\tau F_2(\tau)(\rho-1)}{2r^2} + F_4(\tau), \tag{4.24}$$

where

$$F_1(\tau) = \frac{\Gamma(\Lambda R_b - 1) + \Lambda R_b^2}{-R(\Lambda R_b - 1) + \Lambda R_b^2}, \tag{4.25}$$

$$F_2(\tau) = -\Gamma - F_1(\tau)R, \tag{4.26}$$

$$F_3(\tau) = \frac{R_b^2 R}{R - \Lambda R_b R + \Lambda R_b^2}\left[\frac{1}{6}\frac{dF_1}{d\tau}(\Lambda R^2 - \Lambda R_b^2 - 2R_b) + \right. \tag{4.27}$$

$$\left. + \frac{1}{2}\frac{dF_2}{d\tau}(\Lambda R - \Lambda R_b - 1) + \frac{R_\tau F_2(\tau)(\rho-1)}{2}\left(1 - \frac{\Lambda R^2}{R_b^2} + \frac{2R^2}{R_b^3}\right)\right], \tag{4.28}$$

$$F_4(\tau) = -\frac{R^2}{6}\frac{dF_1}{d\tau} - \frac{R}{2}\frac{dF_2}{d\tau} + \frac{F_3(\tau)}{R} - \frac{R_\tau F_2(\tau)(\rho-1)}{2}. \tag{4.29}$$

Note, T_1, F_3, F_4 involve time derivatives of F_1, F_2. Both derivatives may be written in a form $R_\tau \overline{F}_i$ for appropriate functions $\overline{F}_i$ and consequently the same is true for F_3, F_4.

Similarily for the solid temperature we obtain

$$0 = \frac{k}{c}\frac{1}{r^2}\frac{\partial}{\partial r}\left(r^2\frac{\partial \theta_0}{\partial r}\right) , \qquad \left.\frac{\partial \theta_0}{\partial r}\right|_{r=0} = 0 , \quad \theta_0(R,\tau) = -\frac{\Gamma}{R}, \tag{4.30}$$

$$\frac{\partial \theta_0}{\partial \tau} = \frac{k}{\rho c}\frac{1}{r^2}\frac{\partial}{\partial r}\left(r^2\frac{\partial \theta_1}{\partial r}\right) , \qquad \left.\frac{\partial \theta_1}{\partial r}\right|_{r=0} = 0 , \quad \theta_1(R,\tau) = 0 . \tag{4.31}$$

This has solution

$$\theta_0(r,\tau) = -\frac{\Gamma}{R}, \qquad \theta_1(r,\tau) = \frac{\Gamma}{6}\frac{\rho c}{k}\left(\frac{r^2 - R^2}{R^2}\right) R_\tau. \tag{4.32}$$

These expressions may be substituted into the Stefan condition (4.20). Using the relations $F_{i_\tau} = R_\tau \overline{F}_i$, and rearranging, we obtain a cubic equation for speed of the melt front, R_τ,

$$\epsilon^3\gamma\left(\frac{dR}{d\tau}\right)^3 + \left(\rho\left[L_m(t) + \frac{\alpha}{R}\right] + \epsilon\left[\frac{R\overline{F}_1}{3} + \frac{\overline{F}_2}{2} + \frac{\overline{F}_3}{R^2} - \frac{F_2(\rho-1)}{R} - \frac{\Gamma\rho c}{3R}\right]\right)\frac{dR}{d\tau} - \frac{F_2}{R^2} = 0. \tag{4.33}$$

Whilst seemingly complex this formulation should be compared to the original problem, consisting of two partial differential equations for the temperature, coupled to varying melt temperature and latent heat equations all to be solved over two *a priori* unknown time dependent domains.

Since $\epsilon \ll 1$ we can infer a lot about the melting behaviour from the dominant terms,

$$\frac{dR}{d\tau} = \frac{F_2}{\rho R^2}\left[L_m(t) + \frac{\alpha}{R}\right]^{-1} \approx \frac{F_2}{\rho L_m R^2} . \tag{4.34}$$

For most materials the term in square brackets is dominated by $L_m(t)$ (at least for R larger than order 1 nm), hence we have neglected the surface tension term in the approximation. In dimensional form this leads to the initial melt rate

$$\frac{dR}{dt} \approx -\frac{q_m}{\rho_s L_m R_0^2} . \tag{4.35}$$

This equation is obtained by substituting for F_2, setting $R = R_b = 1$ and neglecting surface tension. It states that the initial melt rate is proportional to the heat flux and inversely proportional to the value of latent heat and square of the radius: smaller particles melt at a much faster rate than larger ones. If we had employed the fixed temperature boundary condition there would be a factor $1/(R_0 - R)$ on the right hand side. Since $R(0) = R_0$ this results in an infinite initial melt rate. This term is not present in equation (4.35) showing that the initial melt rate is in fact finite (as should be expected).

However, if we wish to follow the whole evolution process then we must solve the cubic equation (particularly since we expect $dR/d\tau$ to become large near the end of the melting process). This is a simple matter, we used MATLAB routines to solve the cubic and then integrate the resultant first order differential equation for $R(\tau)$, subject to the initial condition $R(0) = 1$. In the following section we will describe the numerical solution method employed for the full problem and then compare with our results for solving the above cubic equation, leading to the conclusion that the cubic equation is sufficiently accurate.

4.5 Numerical solution

To verify the accuracy of the perturbation solution we now describe a numerical scheme to solve the full problem with all terms retained. To do so, we follow the work in Font and Myers [31], so we define $u = rT$ and $v = r\theta$ and immobilise the boundaries on $r \in (R, R_b)$ via $\eta = (r - R)/(1 - R)$ and on $r \in (0, R)$ via $\zeta = r/R$. The problem (4.16)-(4.19) may now be written

$$\frac{\partial u}{\partial t} = -\eta_t \frac{\partial u}{\partial \eta} + \frac{1}{(R_b - R)^2}\frac{\partial^2 u}{\partial \eta^2} - (1-\rho)\frac{R^2}{(\eta(R_b - R) + R)^2}\left(\frac{1}{R_b - R}\frac{\partial u}{\partial \eta} - \frac{u}{\eta(R_b - R) + R}\right)\frac{dR}{dt}, \quad 0 < \eta < 1, \tag{4.36}$$

$$\frac{\partial v}{\partial t} = -\zeta_t \frac{\partial v}{\partial \zeta} + \frac{1}{R^2}\frac{k}{\rho c}\frac{\partial^2 v}{\partial \zeta^2}, \qquad 0 < \zeta < 1. \tag{4.37}$$

The boundary conditions are

$$\begin{aligned} &u(0,t) = -\Gamma, \quad \left.\frac{\partial u}{\partial \eta}\right|_{\eta=1} = u(1,t)\frac{(1-\Lambda R_b)(R_b - R)}{R_b} + \Lambda R_b(R_b - R), \\ &v(0,t) = 0, \quad v(1,t) = -\Gamma\,. \end{aligned} \tag{4.38}$$

The Stefan condition becomes

$$\rho\beta R\left[RL_m(t) + \alpha\right]\frac{dR}{dt} + \gamma R^2\left(\frac{dR}{dt}\right)^3 = k\left.\frac{\partial v}{\partial \zeta}\right|_{\zeta=1} - \frac{R}{R_b - R}\left.\frac{\partial u}{\partial \eta}\right|_{\eta=0} + \Gamma(k-1). \tag{4.39}$$

A semi-implicit finite difference method is used, whereby we solve implicitly for u and v and explicitly for R. The derivatives in (4.36)-(4.39) are approximated by

$$\frac{\partial u}{\partial t} = \frac{u_i^{n+1} - u_i^n}{\Delta t}, \qquad \frac{\partial u}{\partial \eta} = \frac{u_{i+1}^{n+1} - u_{i-1}^{n+1}}{2\Delta\eta}, \qquad \frac{\partial^2 u}{\partial \eta^2} = \frac{u_{i+1}^{n+1} - 2u_i^{n+1} + u_{i-1}^{n+1}}{\Delta\eta^2}, \tag{4.40}$$

where $i = 1, \ldots, J$ and $n = 1, \ldots, N$ and the derivatives for v are defined in the same manner. The position of the melting front is obtained via the Stefan condition (4.39) using a three-point backward difference for the partial derivatives, and taking the time derivative to be

$$\frac{dR}{dt} = \frac{R^{n+1} - R^n}{\Delta t}. \tag{4.41}$$

Finally, we obtain

$$a_i^n u_{i-1}^{n+1} + b_i^n u_i^{n+1} + c_i^n u_{i+1}^{n+1} = d^n u_i^n, \tag{4.42}$$

$$e_i^n v_{i-1}^{n+1} + f^n v_i^{n+1} + g_i^n v_{i+1}^{n+1} = h^n v_i^n, \tag{4.43}$$

for $i = 1, \ldots, J-1$. For $i = J$,

$$\left(1 - \frac{(1 - \Lambda R_b^n)(R_b^n - R^n)\Delta x}{Rb}\right) u_i^{n+1} - u_{i-1}^{n+1} = \Lambda R_b^n (R_b^n - R^n)\Delta x \quad \text{and} \quad v_i = 1. \tag{4.44}$$

Equations (4.42) and (4.43) allow us to write down a matrix system which we solve at each time step n. For a more detailed description of the scheme see [31].

4.5.1 Small time solution

A well-known difficulty encountered when solving Stefan problems numerically is that the liquid phase does not exist at $t = 0$ yet a numerical solution requires initial values. To overcome this in [31] a small time analysis is performed, which shows that as $t \to 0$ the radius takes the form $R \approx 1 - \lambda t^p$ where $p = 3/4$. This leads to an initial infinite velocity, $R_t \sim -t^{-1/4}$, which is a consequence of specifying a fixed temperature boundary condition. For the present problem we use the same form, but leave p unknown. However, since we use a physically realistic boundary condition we do not expect an infinite velocity, which then indicates $p \geq 1$. The imposed form for R leads to $R_b = 1 + (\rho - 1)\lambda t^p$, and so $R_b - R = \lambda \rho t^p$. Substituting these into equation (4.36) we obtain

$$\begin{aligned}(\lambda\rho t^p)^2 \frac{\partial u}{\partial t} &= -(\lambda\rho t^p)^2 \eta_t \frac{\partial u}{\partial \eta} + \frac{\partial^2 u}{\partial \eta^2} \\ &\quad - (1-\rho)\frac{(\lambda\rho t^p)(1-\lambda t^p)^2}{(\lambda\rho t^p(\eta-1)+1)^2}\left(\frac{\partial u}{\partial \eta} - \frac{(\lambda\rho t^p)u}{\lambda\rho t^p(\eta-1)+1}\right)\frac{dR}{dt}, \qquad 0 < \eta < 1.\end{aligned} \tag{4.45}$$

Provided $p \geq 0$ all terms in the above expression tend to 0 as $t \to 0$ except for the second one on the right hand side of the equation. This results in

$$\frac{\partial^2 u}{\partial \eta^2} \approx 0\ . \tag{4.46}$$

Together with the boundary conditions for u given in (4.38) this leads to

$$u(\eta,t) \approx -\Gamma + \frac{(R_b - R)(\Lambda R_b^2 + \Lambda\Gamma R_b - \Gamma)}{\Lambda R_b^2 + R - \Lambda R_b R}\eta, \tag{4.47}$$

which is the temperature in the liquid at small times.

The melting is driven by the heat flowing through the liquid, consequently we may balance the left hand side of the Stefan condition (4.39) with the temperature gradient in the liquid (which may be calculated using (4.47)). Substituting for R, R_b and taking the Taylor series for $L_m(t) = L_m(0) + tL_m'(0) + \cdots$ and neglecting the terms involving t (since they tend to zero) we obtain

$$-\rho\beta\left[L_m(0) + \alpha\right]\lambda p t^{p-1} - \gamma\lambda^3 p^3 t^{3p-3} = -(\Lambda + \Lambda\Gamma - \Gamma)\ . \tag{4.48}$$

To balance with the right hand side, which is independent of t, requires $p = 1$. This confirms that the initial velocity $R_t \approx -\lambda$ is finite. We have already shown that the kinetic energy term is small, it was retained in [31] because of the initial infinite velocity, in our finite velocity case we may neglect kinetic energy and so determine

$$\lambda = \frac{(\Lambda + \Lambda\Gamma - \Gamma)}{\rho\beta\left[L_m(0) + \alpha\right]}\ . \tag{4.49}$$

Of course we could retain kinetic energy and then solve a cubic for λ, but this makes very little difference to the results.

4.6 Results

In this section we present the results of the model. In all cases we use data for tin, provided in Table 4.1, since we have already calculated an approximate exponential form for the latent heat variation in section §4.2. Thermophysical data for gold nanoparticles may be found in the papers [30, 31] (but without details of the latent heat variation). To permit comparison with a fixed boundary temperature model we also impose the maximum heat flux discussed earlier.

To verify the analytical solution we first compare it with predictions of the melt front position calculated using the numerical model. In Figure 4.3 we plot the variation of the radius $R(t)$ for Stefan numbers $\beta = 10, 100$ (corresponding to $\Delta T = 22$K, 2.2K), initial

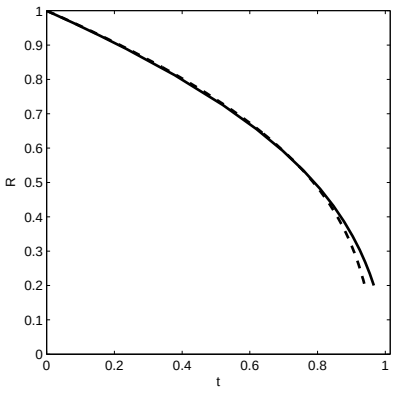

(a) $\beta = 10$, $R_0 = 10$ nm.

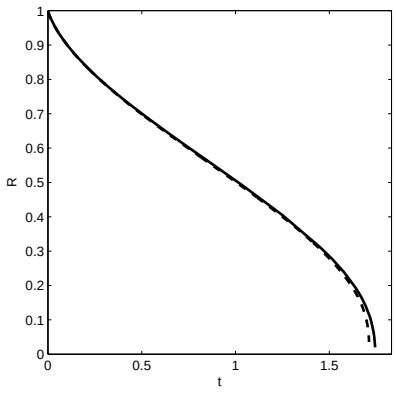

(b) $\beta = 10$, $R_0 = 100$ nm.

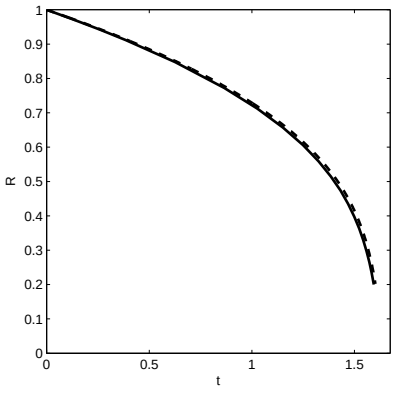

(c) $\beta = 100$, $R_0 = 10$ nm.

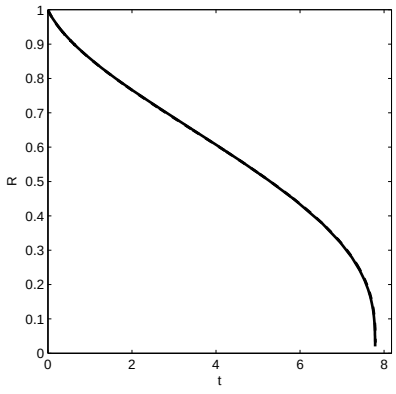

(d) $\beta = 100$, $R_0 = 100$ nm.

Figure 4.3: Melting front evolution of a tin nanoparticle for perturbation (solid line) and numerical (dashed line) solutions for various β and R_0. The time-scale is $k_l/(\rho_l c_l R_0^2$, so when $R_0 = 10$nm the dimensional time is obtained by dividing the non-dimensional value by 1.604×10^{11}s and when $R_0 = 100$nm by 1.604×10^9s.

radius $R_0 = 10, 100$ nm and a cooling condition with $h = h_{max} = 4.7 \times 10^9 \mathrm{W}/(\mathrm{m}^2\mathrm{K})$. The dashed lines represent the numerical solution described in Section 4.5. The solid lines come from the perturbation solution; calculated by solving the cubic equation (4.33) for R_τ and then integrating.

Note, we have plotted R down to the non-dimensional equivalent of 2 nm (i.e. when $R_0 = 10$ nm the final value $R = 0.2$, for $R_0 = 100$ nm the final value is $R = 0.02$). The perturbation solution is based on an expansion in terms of $\epsilon = 1/\beta$, and terms of order ϵ^2

have been neglected. We therefore expect the greatest accuracy for the large β solutions. This is clearly the case: the two curves with $\beta = 10$ are clearly less accurate than those with $\beta = 100$. However all sets of curves show good agreement, the worst being that of Figure 4.3 a) where at the final time calculated there is a difference of 3% between the numerical and analytical results. For the best case, with $\beta = 100$, $R_0 = 100$ nm the final difference is around 0.1%. The four graphs demonstrate that for a range of R_0 and β the evolution of the radius $R(t)$ is accurately predicted by the perturbation solution. The radius is calculated by integrating the Stefan condition, which shows $R_t \propto -T_r(R,t)$, so we can conclude that the perturbation solution for $T_r(R,t)$ is also accurate (and in fact our numerical results demonstrate that $T(r,t)$ is also well-approximated).

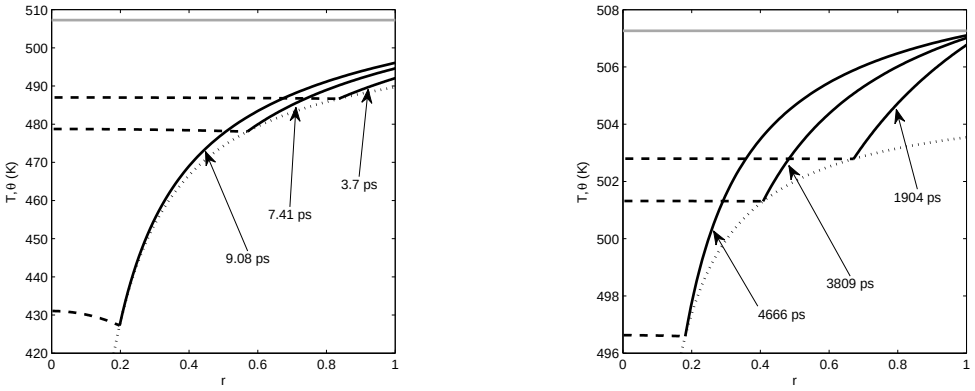

(a) $R_0 = 10$ nm. **(b)** $R_0 = 100$ nm.

Figure 4.4: Temperature profile of a tin nanoparticle. The solid and dashed lines represent the temperatures in the liquid and solid, respectively. The dotted line is the melting temperature given by the generalised Gibbs-Thomson equation (4.14). Black horizontal line denotes $T_H = 507.6$ K, $\beta = 100$.

In Figure 4.4 we show temperature profiles for different times as a function of r for $\beta = 100$ and $R_0 = 10, 100$ nm. Solid lines represent the temperature in the liquid, dashed lines that in the solid and the dotted line is the melt temperature variation. The solid-liquid interface follows the dotted line. For the 10 nm particle, shown in Figure 4.4 a), the initial melt temperature is close to 490 K. The boundary of the liquid layer does not exceed this temperature by a great amount, rising to a maximum of approximately 496 K. However, by

the time the boundary has reached 496K the melt temperature has decreased to less than 430 K. This verifies our previous statement that only a slight temperature rise above the melt temperature is required for complete melting. The curves for $t = 9.08$ ps represent the temperature profile when we expect the continuum model to break down. Here it is clear that both the solid and liquid regions are above the melt temperature. In a bulk Stefan problem we would expect the solid to be below the melt temperature, thus while the liquid temperature drives the melting the solid acts to slow it down. In the present situation, due to the melting point depression, the solid temperature exceeds the melt temperature and so both the solid and the liquid drive the melting. This feature has been observed in previous studies of nanoparticle melting [30, 60]. The second figure shows temperature profiles for a particle with $R_0 = 100$ nm. Now the process takes much longer and the temperature rise at the boundary is greater.

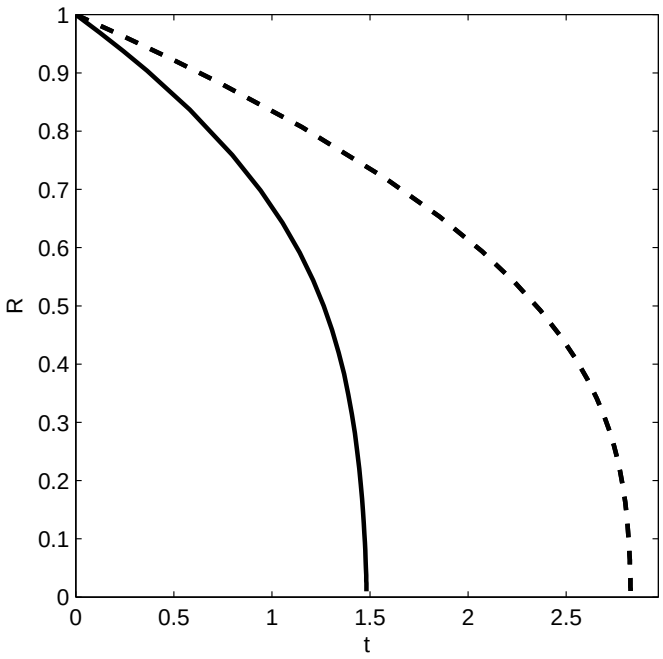

Figure 4.5: Melt front position for the new (solid line) and old (dashed line) Stefan conditions, $R_0 = 10$ nm, $\beta = 100$. Dimensional times are obtained by dividing the non-dimensional value by 1.604×10^{11}s.

In Figure 4.5 we compare the evolution of the radius using the Stefan condition (4.19)

(in dimensional form equation (4.10)) (solid line) with that of the standard Stefan condition from the literature, as described in §4.3, (dashed line). For an initial particle size $R_0 = 10$ nm the current model predicts melting at almost twice the rate of the previous model. Looking at the effective latent heat definitions from the two models shows that they both have the same kinetic energy terms, so the difference must lie in the (dimensional) terms $L_m(t) + 2\sigma^*_{sl}/(\rho_s R)$ and $L^*_m + (c_l - c_s)(T_m - T^*_m)$. From Table 4.1 we obtain $2\sigma^*_{sl}/(\rho_s R) \approx 1.8 \times 10^{-5}/R$. This is equal to the bulk latent heat only when $R \approx 0.3$ nm, so for most of the melt process we can assume the current model predicts a melt rate of the order $R_t \propto 1/L_m(t)$. The previous model has $(c_l - c_s)(T_m - T^*_m) \approx 2000$ (if we assume a maximum temperature change of order 50K, as shown in Figure 4.4 a). This is always significantly smaller than L^*_m and so the previous model predicts (approximately) $R_t \propto 1/L^*_m$. Given that the value of latent heat decreases by a large amount during melting, so making it easier for molecules to leave the surface, it is clear that the true melting rate must be much faster than predicted by any previous model where $R_t \propto 1/L^*_m$. Note, since $L_m(t) \to L^*_m$ as the radius increases the difference in results will decrease with an increase in initial particle size. For example, if we carry out the same calculation as shown in Figure 4.5 but set $R_0 = 100$ nm then the difference in final melt times reduces to around 2%. So perhaps the key point to take from this figure is that for small nanoparticles (below the size where the actual latent heat differs significantly from the bulk value) latent heat variation must be accounted for in theoretical modelling of nanoparticle melting.

In previous mathematical models the boundary condition imposed was $T(R_b, t) = T_H$ instead of the Newton cooling condition employed in this paper. In Figure 4.6 we show the difference in melting for the perturbation solution subject to the Newton cooling condition (4.11) (solid line) and a fixed temperature boundary condition (dashed line), both with $T_H = 507.6$K. For the 10 nm particle the change in boundary condition results in melting almost three times slower than with a fixed temperature. When $R_0 = 100$ nm the melting time increases by only 13.5%. The discrepancies may be attributed to the energy transfer to the particle. The fixed temperature boundary condition is equivalent to specifying perfectly efficient heat transfer from the surrounding material, that is the heat transfer coefficient is infinite. Initially the particle is at some temperature below the melt temperature. At $t = 0$ the infinite heat transfer instantaneously raises the boundary temperature to T_H,

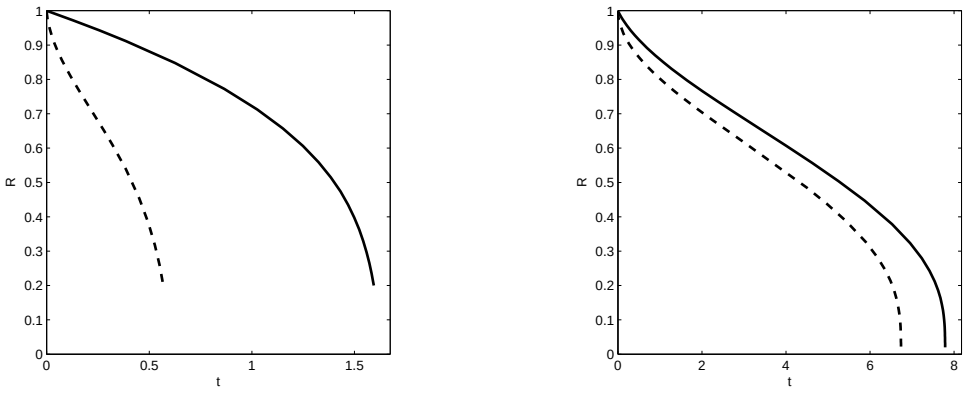

(a) $R_0 = 10$ nm. **(b)** $R_0 = 100$ nm.

Figure 4.6: Melt front position with a Newton cooling boundary condition (solid line) and fixed temperature boundary condition (dashed line), $\beta = 100$. Dimensional times are obtained by dividing the non-dimensional value by 1.604×10^{11}s when $R_0 = 10$nm and by 1.604×10^{9}s when $R_0 = 100$nm.

this results in an infinite temperature gradient and so, according to the Stefan condition, an infinite boundary velocity. In the figure we see that the curve at $t = 0$ is vertical. Consequently the fixed boundary temperature model must predict faster melting than in reality. The cooling condition, even with the maximum allowable heat flux, exhibits a finite melt rate and overall slower melting.

There are further consequences of the previously employed infinite heat transfer. The liquid velocity $v(R,t) = (1-\rho)R_t$, if $R_t(0)$ is infinite then so is $v(R,0)$ and hence the initial kinetic energy. Let us consider the effect of the kinetic energy term on the Stefan condition (4.20). It is represented by $\gamma\epsilon^3 R_\tau^3$, where $\gamma \propto (1 - \rho_s/\rho_l)$ (time has been rescaled with the Stefan number). In a standard perturbation we would neglect this term due to the small factor ϵ^3. It was retained in the current model since at least for part of the process we anticipated large R_τ. In places where the velocity is small its contribution will be negligible and so its retention does not affect the results. If the velocity is large then the kinetic energy term represents a considerable energy sink, resulting in slower melting. This was observed in the solutions presented in [31] with a fixed temperature boundary condition and gold nanoparticles. In the present study we have shown that the initial infinite velocity does not occur and so the initial kinetic energy is negligible. The question is then, does the

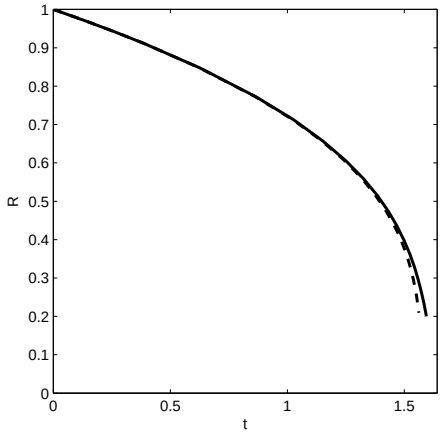

Figure 4.7: Comparison of $R(t)$ for $R_0 = 10$ nm, $\beta = 100$, with and without the kinetic energy terms in the Stefan condition. Dimensional times are obtained by dividing the non-dimensional value by 1.604×10^{11}s.

high melting rate in the final stages lead to a non-negligible kinetic energy contribution? In Figure 4.7 we compare results with and without the kinetic energy term for a 10 nm particle and $\beta = 100$. Clearly the difference is very small, resulting in only a 2% change in the final melting time. We do not show the corresponding result for $R_0 = 100$ nm since the two curves are indistinguishable. This seems to indicate that the contribution of kinetic energy to the Stefan condition is negligible, which would then result in a simpler mathematical model, given that the cubic term in R_t could be removed. However, we note that for tin $\rho = \rho_s/\rho_l = 1.028$ whereas for gold $\rho = 1.116$. In Font and Myers [31] it was stated that the inclusion of kinetic energy and density change had a significant impact on the melting process and this was so strong that it carried through to macroscale melting. From the present study it seems their conclusion should be toned down since

1. the effect of kinetic energy is magnified by the use of a fixed temperature boundary condition;

2. the effect also depends on the solid to liquid density ratio, the higher the ratio the greater the effect.

4.7 Conclusions

The work in this paper describes a model for the melting of a spherically symmetric nanoparticle. It has various novel features which appear to have important consequences for modelling at the nanoscale. Specifically it is the first mathematical model of nanoparticle melting

1. to include latent heat depression;

2. to employ the new Stefan condition developed in [70];

3. to use a Newton cooling condition.

Experimental observation and MD simulations on nanoparticle melting have made it clear that latent heat depression is significant, even more so than the well-documented melting point depression. To date mathematical models of nanoparticle melting have accounted for the latter effect, but not the latent heat variation. In §4.2 we proposed an exponential model to describe published data on the latent heat variation of tin. This contained a single fitting parameter, and provided much better agreement with the data than previous models in the literature, particularly when the nanoparticle size was greater than 20 nm.

Previous mathematical analyses of nanoparticle melting have imposed a fixed boundary temperature. This condition is equivalent to specifying an infinite heat transfer coefficient, which then leads to melt rates greater than occurs in practice. The present study uses a cooling condition at the boundary, this is more physically realistic and leads to slower, finite melt rates. The decreased melt rates impact on the kinetic energy contribution. The only previous mathematical analyses of nanoparticle melting with density change employed the fixed temperature condition and concluded that the density change was very important, since the resultant kinetic energy provides an energy sink which then reduces the energy available to drive the phase change. This effect was so strong that it carried through even to the macroscale. Their study used data for gold, which has a large difference between liquid and solid density. Our work, which uses data for tin (with a density ratio close to unity) and a heat flux of the order of the maximum possible value for thermodynamic stability

indicated a much smaller influence of kinetic energy. This is attributed primarily to the new boundary condition, which removes the initial infinite melt rate (and corresponding infinite kinetic energy). The choice of maximum possible heat flux was to permit comparison with results from the literature, in practice one would use a smaller value and so, in general, kinetic energy would be even lower than in our calculations. Consequently, our results indicate that provided the density difference is not large and the boundary condition is physically realistic then the contribution of kinetic energy to the Stefan condition may be neglected. This will then considerably simplify the formulation, allowing the removal of the cubic velocity term.

The mathematical model contained two other novel features, namely the latent heat variation and the new Stefan condition. Both of these play a role in the melting behaviour, although since latent heat is the dominant term for most of the process it is the latent heat variation that appears to be the most important.

One final point to note is that in previous studies of nanoparticle melting, the speed of melting of small particles was close to the relaxation time for the material. When we include latent heat variation this melting time decreases even further (the cooling condition has some effect in slowing down melting, but is not as strong as the latent heat effect). This indicates that in future models it would be sensible to investigate non-classical heat equations which hold over very short time-scales.

5 | Application of the TIM to one-phase nanoparticle melting

In this chapter we briefly show how the techniques developed in Chapter 3 may be used on phase change problems such as the one described in the previous chapter. The purpose being to highlight the simplicity of the technique using a model for which numerical and perturbation solutions already exist. To make the mathematical exposition clear we work with a reduced form of the model of Chapter 4, where the density remains the same in either phase, hence the outer boundary is fixed. Further, we consider the one-phase case, that is, where one of the phases is neglected, in this case by setting the solid temperature to the phase change temperature.

5.1 One-phase reduction

To obtain the one-phase reduction of (4.16)-(4.19) we set the solid temperature to $T_m(t)$ throughout the whole process [75] and take $\rho = 1$. This transforms the problem to

$$\frac{\partial T}{\partial t} = \frac{1}{r^2}\frac{\partial}{\partial r}\left(r^2\frac{\partial T}{\partial r}\right), \qquad R(t) < \ r < 1, \tag{5.1}$$

with $R(0) = 1$. Boundary conditions are

$$\text{(a) } T(1,t) = 1 \quad \text{or} \quad \text{(b) } \left.\frac{\partial T}{\partial r}\right|_{r=1} = \mathrm{Nu}(1 - T(1,t)), \qquad \text{(c) } T(R,t) = T_m(t) = -\frac{\Gamma}{R}, \tag{5.2}$$

where $\mathrm{Nu} = (R_0 h)/k$. Note that in the equation above we use the Nusselt number Nu but in equation (4.18) we use Λ. They are equivalent but Λ specifically denotes the Nusselt

number with the maximum heat transfer coefficient that the system allows before directly vapourising the nanoparticle. The one-phase Stefan condition is

$$\beta \left[L_m(t) + \frac{\alpha}{R} \right] \frac{\mathrm{d}R}{\mathrm{d}t} = -\left. \frac{\partial T}{\partial r} \right|_{r=R}. \tag{5.3}$$

5.2 OpTimal Integral Method (TIM)

In this section we will solve the one-phase problem (5.1)-(5.3) using the opTimal Integral Method (TIM). The exponents for the polynomial approximate solution were presented in Chapter 3. For the fixed temperature boundary condition (5.2a), we will use $n = 1.6$ for all cases. For the Newton cooling boundary condition (5.2b), $n \in [1.63, 1.95]$, see Table 3.1.

In Chapter 3 we showed that the transformation $u = rT$ led to more accurate results for the melting of spherical particles, than those obtained in the original geometry. Consequently, we now adopt this transformation. The governing equation (5.1) becomes

$$\frac{\partial u}{\partial t} = \frac{\partial^2 u}{\partial r^2}, \qquad R(t) < \ r < 1. \tag{5.4}$$

The boundary conditions are

$$\text{(a) } u(1,t) = 1 \quad \text{or} \quad \text{(b) } \left. \frac{\partial u}{\partial r} \right|_{r=1} = u(1,t)(1 - \mathrm{Nu}) + \mathrm{Nu}, \qquad \text{(c) } u(R,t) = -\Gamma, \tag{5.5}$$

and the Stefan condition is

$$R\rho\beta \left[RL_m(t) + \alpha \right] \frac{\mathrm{d}R}{\mathrm{d}t} = -R \left. \frac{\partial u}{\partial r} \right|_{r=R} - \Gamma. \tag{5.6}$$

To be able to employ the TIM, we need to choose an approximating function over a finite region for the temperature [63]. We choose the standard form of equation (3.8),

$$u(r,t) = a \left(\frac{r-R}{1-R} \right) + b \left(\frac{r-R}{1-R} \right)^n + c. \tag{5.7}$$

5.2.1 Fixed temperature

Upon substituting (5.7) into the boundary conditions (5.5a) and (5.5c) we obtain

$$a = 1 + \Gamma - b, \qquad c = -\Gamma. \tag{5.8}$$

As demonstrated in Chapter 3 the appropriate value of n in equation (5.7) is $n = 1.6$. This leaves us with the two unknowns $b(t)$ and $R(t)$. The first of the two equations to determine

the unknowns is found by substitution of u into the Stefan condition (5.6). This leads to an ordinary differential equation

$$R\beta[RL_m + \alpha]\frac{\mathrm{d}R}{\mathrm{d}t} = -\frac{aR}{1-R} - \Gamma, \tag{5.9}$$

where a is given in terms of b by (5.8).

The second equation comes from integrating the heat equation (5.4), yielding the Heat Balance Integral,

$$\int_R^1 \frac{\partial u}{\partial t}\,\mathrm{d}r = \int_R^1 ur\,\mathrm{d}r \quad \Rightarrow \quad \frac{\mathrm{d}}{\mathrm{d}t}\int_R^1 u(r,t)\,\mathrm{d}r - \Gamma\frac{\mathrm{d}R}{\mathrm{d}t} = \left.\frac{\partial u}{\partial r}\right|_{r=1} - \left.\frac{\partial u}{\partial r}\right|_{r=R}. \tag{5.10}$$

Upon substituting the approximating function (5.7) into (5.10) we obtain an ODE for $b(t)$,

$$\frac{\mathrm{d}b}{\mathrm{d}t} = \frac{(1-R)[(n+1)a + 2b]R_t + 2bn(n+1)}{(1-R)^2[1-n]}. \tag{5.11}$$

The initial condition for the position of the melt front is $R(0) = 1$. The initial condition for b is not yet known. To determine this we note that at small times $R = 1 - 2\lambda t^{1/2}$, see §3.3.1 in Chapter 3, where λ is an unknown constant. The value for λ is only needed for the numerical solution. For more details on the numerical scheme, see Chapter 3, §3.3.1 *Numerical solution*. Substituting this small time expression for R into (5.9) gives

$$b(t) = -\frac{2[(1-2\lambda t^{1/2})\beta[(1-2\lambda t^{1/2})L_m + \alpha]\lambda - \Gamma t^{1/2}]\lambda}{1-2\lambda t^{1/2}} + \Gamma + 1, \tag{5.12}$$

which leads to $b(0) = -2\beta(L_m(0) + \alpha)\lambda^2 + 1 + \Gamma$ in the limit $t \to 0$.

Hence the fixed temperature one-phase Stefan problem has reduced to solving two first order ODEs (5.9), (5.11) subject to the initial conditions $R(0) = 1$, $b(0) = -2\beta(L_m(0) + \alpha)\lambda^2 + 1 + \Gamma$.

5.2.2 Newton cooling

Now we consider condition (5.5b) at the outer boundary. This indicates

$$a = \frac{(1-R)[\mathrm{Nu} + (1-\mathrm{Nu})(b-\Gamma)] - nb}{\mathrm{Nu} + R(1-\mathrm{Nu})}, \qquad c = -\Gamma. \tag{5.13}$$

The exponent n required in equations (5.7), (5.13) will be taken from Table 3.1, depending on the parameters β and Nu chosen.

The first equation to determine the unknowns $R(t)$ and $b(t)$ is given by (5.9), but now a is given by (5.13). The second equation needed to close the system is given by the Heat Balance Integral (5.10), which in this case leads to

$$\frac{\mathrm{d}b}{\mathrm{d}t} = \frac{(1-R)[(n+1)a+2b]R_t + (n+1)[2bn-(1-R)^2F_1(t)]}{(1-R)^2[2+(n+1)F_2(t)]}, \tag{5.14}$$

where

$$\begin{aligned} F_1(t) &= \left[-\frac{\mathrm{Nu}+(1-\mathrm{Nu})(b-\Gamma)}{1-(1-R)(1-\mathrm{Nu})} - \frac{[(1-R)(\mathrm{Nu}+(1-\mathrm{Nu})(b-\Gamma))-bn](1-\mathrm{Nu})}{[1-(1-R)(1-\mathrm{Nu})]^2}\right]\frac{\mathrm{d}R}{\mathrm{d}t}, \\ F_2(t) &= \frac{(1-R)(1-\mathrm{Nu})-n}{1-(1-R)(1-\mathrm{Nu})}. \end{aligned} \tag{5.15}$$

In the limit $\mathrm{Nu}\to\infty$, $F_1\to 0$, $F_2\to -1$, and equation (5.11) is retrieved.

To find the initial condition for b we approximate $R = 1-\lambda t$ for small times (see §4.5.1 in Chapter 4), where λ is an unknown constant. Substituting this expression R for small times into (5.9) gives

$$b(t) = \frac{[(1-\lambda t)\rho\beta((1-\lambda t)L_m(t)+\alpha)\lambda-\Gamma](1-\lambda t(1-\Gamma))\lambda t + \lambda t(1-\lambda t)(\Gamma-\Lambda-\Gamma\Lambda)}{n(1-\lambda t)(\lambda t\lambda t-1)}, \tag{5.16}$$

which leads to $b(0)=0$ in the limit $t\to 0$.

So for the Newton cooling condition the one-phase Stefan problem reduces to the solution of (5.9), (5.14) subject to $R(0)=1$, $b(0)=0$.

5.2.3 Perturbation solution

In this section we present the perturbation solution for the one-phase Stefan problem of equations (5.1)-(5.3). The perturbation solution will be based on a large Stefan number $\beta \gg 1$. We approximate the temperature $T \approx T_0 + \epsilon T_1$, where $\epsilon = 1/\beta$ and rescale time such that $\tau = \epsilon t$. Equation (5.1) leads to

$$0 = \frac{1}{r^2}\frac{\partial}{\partial r}\left(r^2\frac{\partial^2 T_0}{\partial r^2}\right), \tag{5.17}$$

$$\frac{\partial T_0}{\partial \tau} = \frac{1}{r^2}\frac{\partial}{\partial r}\left(r^2\frac{\partial^2 T_1}{\partial r^2}\right). \tag{5.18}$$

Boundary conditions (5.2a) and (5.2b) result in

$$T_0(1,\tau) = 1, \qquad T_1(1,\tau) = 0, \tag{5.19}$$

$$\left.\frac{\partial T_0}{\partial r}\right|_{r=R} = \mathrm{Nu}(1 - T_0(1,\tau)), \qquad \left.\frac{\partial T_1}{\partial r}\right|_{r=R} = -\mathrm{Nu}\, T_1(1,\tau), \tag{5.20}$$

respectively. Boundary condition (5.2c) leads to

$$T_0(R,\tau) = -\frac{\Gamma}{R}, \qquad T_1(R,\tau) = 0. \tag{5.21}$$

Finally, the Stefan condition (5.3) is

$$\left[L_m(t) + \frac{\alpha}{R}\right]\frac{\mathrm{d}R}{\mathrm{d}\tau} = -\left.\frac{\partial T_0}{\partial r}\right|_{r=R} - \epsilon\left.\frac{\partial T_1}{\partial r}\right|_{r=R}. \tag{5.22}$$

The general solution of (5.17)-(5.18) is

$$T_0(r,\tau) = G_1(\tau) + \frac{G_2(\tau)}{r}, \tag{5.23}$$

$$T_1(r,\tau) = \frac{r^2}{6}\frac{\mathrm{d}G_1}{\mathrm{d}\tau} + \frac{r}{2}\frac{\mathrm{d}G_1}{\mathrm{d}\tau} - \frac{G_3(\tau)}{r} + G_4(\tau). \tag{5.24}$$

Applying boundary conditions (5.19) and (5.21) we obtain

$$G_1(\tau) = \frac{1+\Gamma}{1-R(t)}, \tag{5.25}$$

$$G_2(\tau) = -\left(\frac{\Gamma}{R} + G_1\right)R, \tag{5.26}$$

$$G_3(\tau) = \frac{R}{6}\frac{(1+\Gamma)(2-R)}{(1-R)^2}\frac{\mathrm{d}R}{\mathrm{d}\tau}, \tag{5.27}$$

$$G_4(\tau) = -\frac{R^2}{6}\frac{1+\Gamma}{(1-R)^2}\frac{\mathrm{d}R}{\mathrm{d}\tau} - \frac{R^2}{2}\left(\frac{\Gamma}{R^2} - \frac{1+\Gamma}{(1-R)^2}\right)\frac{\mathrm{d}R}{\mathrm{d}\tau} - \frac{R}{2}\left(\frac{\Gamma}{R} - \frac{1+\Gamma}{1-R}\right)\frac{\mathrm{d}R}{\mathrm{d}\tau} + \frac{G_3}{R}. \tag{5.28}$$

Substituting the solution given by (5.23) and (5.24), using the coefficients G_i given by (5.25)-(5.28), into the Stefan condition (5.22) we obtain an ODE for $\mathrm{d}R/\,\mathrm{d}\tau$. This is easily solved via MATLAB's routine `ode45` with initial condition $R(0) = 1$, thus obtaining the perturbation solution for the melt front for the case of a fixed temperature boundary condition.

Alternatively, if we apply the Newton cooling boundary conditions (5.20) and (5.21) we find

$$G_1(\tau) = -\frac{\Gamma - \Lambda(1+\Gamma)}{R + \Lambda(1-R)}, \tag{5.29}$$

$$G_2(\tau) = -\left(\frac{\Gamma}{R} + G_1\right)R, \tag{5.30}$$

$$G_3(\tau) = \frac{R}{6}\frac{(\Lambda^2(R^2-3R+2)+\Lambda(2-R^2)+2)[(\Gamma+1)\Lambda-\Gamma]}{[(\Lambda-1)R-\Lambda]^3}\frac{\mathrm{d}R}{\mathrm{d}\tau}, \tag{5.31}$$

$$\begin{aligned} G_4(\tau) = &-\frac{R^2}{6}\frac{(\Lambda(1+\Gamma)-\Gamma)(\Lambda-1)}{(R+\Lambda(1-R))^2}\frac{\mathrm{d}R}{\mathrm{d}\tau} - \frac{R^2}{2}\left(\frac{\Gamma}{R^2} - \frac{\Lambda(1+\Gamma)-\Gamma)(\Lambda-1)}{(R+\Lambda(1-R))^2}\right)\frac{\mathrm{d}R}{\mathrm{d}\tau} \\ &- \frac{R}{2}\left(\frac{\Gamma}{R} - \frac{\Lambda(1+\Gamma)-\Gamma)(\Lambda-1)}{(R+\Lambda(1-R))^2}\right)\frac{\mathrm{d}R}{\mathrm{d}\tau} + \frac{G_3}{R}. \end{aligned} \tag{5.32}$$

Upon substitution of (5.29)-(5.32) into (5.23) and (5.24) we obtain the perturbation solution for the liquid temperature in the case of a Newton cooling boundary condition. Now, substituting this solution into the Stefan condition (5.22) gives an ODE for $\mathrm{d}R/\,\mathrm{d}\tau$. Again, we solve it via MATLAB's routine `ode45` with initial condition $R(0) = 1$.

5.3 Results

In Figure 5.1 we show the evolution of the melt front with a fixed boundary temperature. Four cases are shown, corresponding to $\beta = 1$, 10 and $R_0 = 10$, 100 nm. Each graph contains three curves: the solid line is the TIM solution, the dashed line is the numerical solution and the dash-dot line the perturbation solution. The results in Figures 5.1(b), 5.1(c) and 5.1(d) show excellent agreement between the TIM and numerical solutions. In the final figure the curves are virtually indistinguishable, except for in the very final stages of melting. Figure 5.1(a) shows the greatest discrepancy, resulting in a difference of approximately 11% between the final melt time predicted by the numerical and TIM solutions. This may be attributed to the use of an average exponent from Chapter 3, where in general $R_0 \gg 10$ nm. Taking a higher value of n reduces the error; for example with $n = 1.8$ the final difference is approximately 2%. In the first three figures, Figure 5.1(a)-(c), the perturbation solution is by far the worst approximation. This should be expected when $\beta = 1$ however it is clearly worse in Figure 5.1(b) where $\beta = 10$. Only in Figure 5.1(d) the perturbation solution and the TIM become nearly undistinguishable. Both approximate solutions are highly accurate so the choice is rather irrelevant.

In Figure 5.2 we show the evolution of the melt front for the one-phase Stefan problem, employing the Newton cooling boundary condition. We show the results for different parameter sets: $\beta = 1$, 10 and $\mathrm{Nu} = 1.5$, 15 (corresponding to $R_0 = 10$, 100 nm, respectively). In solid lines we show the solution given by the TIM. The optimal exponents in this case depend on the parameter values picked and are taken from Table 3.1. In dashed lines we

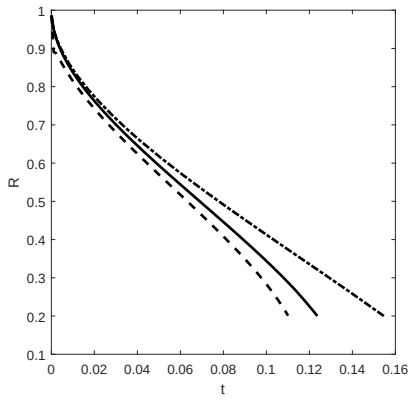

(a) $\beta = 1$, $R_0 = 10$ nm.

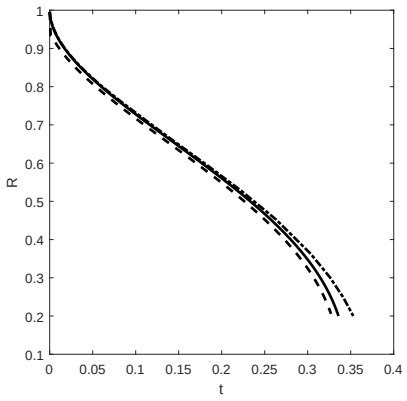

(b) $\beta = 10$, $R_0 = 10$ nm.

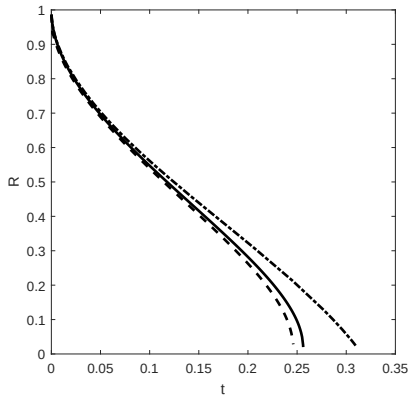

(c) $\beta = 1$, $R_0 = 100$ nm.

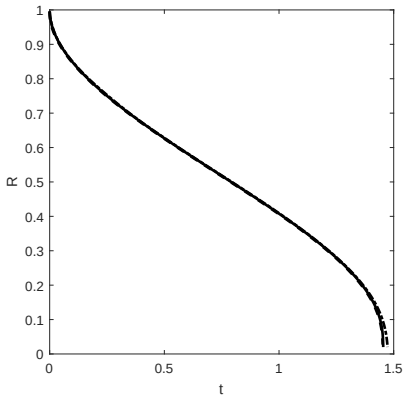

(d) $\beta = 10$, $R_0 = 100$ nm.

Figure 5.1: Melting front evolution of a spherical particle given by the TIM solution of the one-phase problem using the optimal exponents $n = 1.6$ (solid), by the numerical solution of the one-phase problem (dashed) and by the perturbation solution (dash-dotted) for various β and R_0.

show the numerical solution. In dash-dot lines, we show the perturbation solution. All results in Figure 5.2 show excellent agreement between the TIM and numerical solutions. In Figure 5.2(b) and 5.2(d) the curves are virtually indistinguishable, except for in the very final stages of melting. Figure 5.2(c) shows the greatest discrepancy, resulting in a difference of less than 3% between the final melt time predicted by the numerical and TIM solutions. In all cases the TIM is more accurate than the perturbation solution. This is not surprising when $\beta = 1$, but it is interesting to see that the perturbation solution is less accurate even when $\beta = 10$, although in the case shown in Figure 5.2(d) both solutions are

highly accurate.

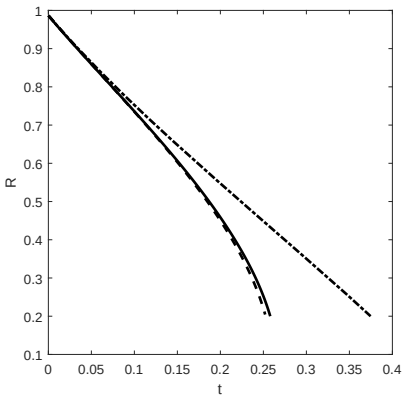

(a) $\beta = 1$, $\mathrm{Nu} = 1.5$, $n = 1.95$.

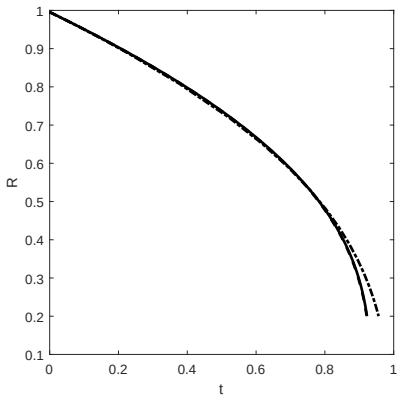

(b) $\beta = 10$, $\mathrm{Nu} = 1.5$, $n = 1.89$.

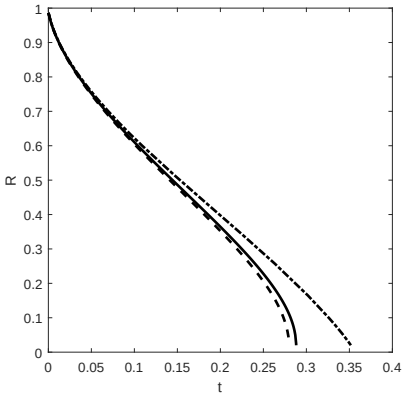

(c) $\beta = 1$, $\mathrm{Nu} = 15$, $n = 1.68$.

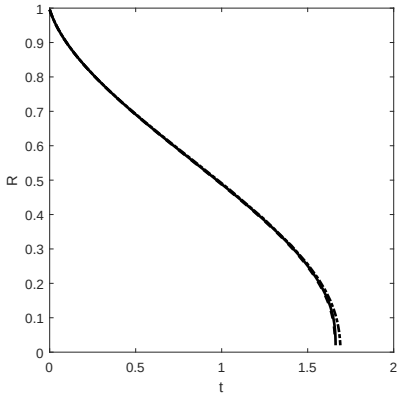

(d) $\beta = 10$, $\mathrm{Nu} = 15$, $n = 1.63$.

Figure 5.2: Melting front evolution of a spherical particle given by the TIM solution of the one-phase problem using the optimal exponents found in Table 3.1 (solid), by the numerical solution of the one-phase problem (dashed) and by the perturbation solution (dash-dotted) for various β and Nu.

The main reason behind the HBIM's popularity is the ease of use. For the current problem when applying a Newton cooling condition we have only studied the two Nu values where the optimal n is provided in Table 3.1. For different Nu we would have to determine the n to minimise the error as specified in Chapter 3 so adding to the complexity of this method. For this reason, in Figure 5.3 we show the evolution of the melt front for the one-phase Stefan problem with a Newton cooling boundary condition using the TIM solution

but now keeping n fixed at the average value of Table 3.1, that is $n = 1.79$ (solid lines). Numerical and perturbation solution are shown in dashed and dash-dot lines, respectively. We find that the agreement between the TIM and numerical solutions is excellent in all four cases. In Figure 5.3(b)-(d) the TIM and numerical solutions are virtually indistinguishable. Again, in all cases the TIM is the most accurate. From this we may conclude that the TIM with $n = 1.79$ is an accurate approximation solution method for spherical melting subject to Newton cooling.

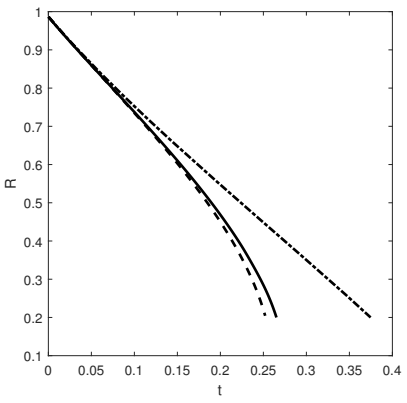

(a) $\beta = 1$, Nu $= 1.5$.

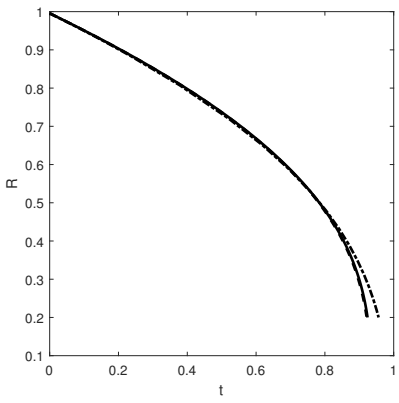

(b) $\beta = 10$, Nu $= 1.5$.

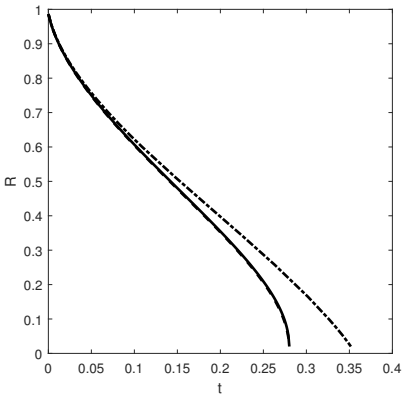

(c) $\beta = 1$, Nu $= 15$.

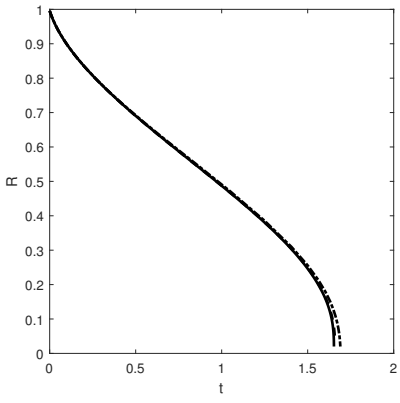

(d) $\beta = 10$, Nu $= 15$.

Figure 5.3: Melting front evolution of a spherical particle given by the TIM solution of the one-phase problem using the optimal average exponent $n = 1.79$ (solid), by the numerical solution of the one-phase problem (dashed) for various β and Nu, and by the perturbation solution (dash-dotted).

5.4 Conclusions

In this chapter we analysed a reduced form of the model of Chapter 4 in which the density in the two phases is the same. By setting the solid temperature to the phase change one, we obtained a one-phase reduction of the Stefan problem for spherical melting. Our goal was to determine whether the techniques developed in Chapter 3 could help in the study of spherical melting under realistic conditions. The results were compared against a numerical solution as well as a perturbation solution, which is the standard choice of approximate solution method.

First we studied the case for the fixed temperature boundary condition. Chapter 3 suggests the use of the average optimal exponent $n = 1.6$ in the TIM approximation. This choice showed excellent results, except for the case when $\beta = 1$ and $R_0 = 10$ nm, for which the error was 11%. We attributed this discrepancy to the choice of an average optimal exponent. Picking a slightly higher value of n reduced the error to 2%. In all cases, even when the error was 11% the perturbation solution was less accurate than the TIM.

We then studied the case of Newton cooling at the outer boundary. In Chapter 3 we dealt with two values of the Nusselt number and determined the optimal exponent n for both values. Solutions with these two Nusselt numbers were obtained. As with the fixed temperature case the TIM was the most accurate in all cases, even when the Stefan number was large.

A problem with the results of Chapter 3 is that the exponent was only provided for two Nusselt numbers, for other values n must be recalculated which complicates the calculations. For this reason we presented results using an average n, rather than the specific value for a given Nu. This still produced highly accurate results and again these were more accurate than the corresponding perturbation solutions.

In summary then the work of this chapter makes clear that the TIM can provide highly accurate solutions for nanoparticle melting by setting $n = 1.6$ for the fixed boundary temperature problem and $n = 1.79$ with Newton cooling. The work involved in calculating the TIM solution is similar to that of the perturbation method, which was less accurate for all cases examined. Consequently the TIM should be preferred over the more popular perturbation method.

Part II

The Kirkendall Effect

6 | Mathematical model for substitutional binary diffusion in solids

---

H. Ribera, B. Wetton, T. G. Myers

Mathematical model for substitutional binary diffusion in solids

Submitted to Applied Mathematical Modelling

Impact factor: 2.35

Abstract

In this paper we detail the mechanisms that drive substitutional binary diffusion and derive appropriate governing equations. We focus on the one-dimensional case with insulated boundary conditions. Asymptotic expansions are used in order to simplify the problem. We are able to obtain approximate analytical solutions in two distinct cases: the two species diffuse at similar rates, and the two species have largely different diffusion rates. A numerical solution for the full problem is also described.

6.1 Introduction

The first systematic study on solid state diffusion was carried out by Roberts [89, Part II] in 1896, in which he studied diffusion of gold into solid lead at different temperatures, and

that of gold into solid silver. At the time it was believed that in binary diffusion both species had the same diffusion rate. Pfeil [82] noticed some strange behaviour in iron/steel oxidation in which muffle pieces would fall into the surface of the oxidising iron and were slowly buried until they disappeared beneath the surface. By breaking up the oxidised layer these muffle pieces could be recovered. This seemed to indicate that the diffusion rate of iron and oxygen were not the same. Motivated by this observation Smigelskas and Kirkendall [99] designed an experiment in which a rectangular block of brass (Cu-Zn alloy) was wound with molybdenum (Mo) wires, since Mo is inert to the system and moves only depending on the transferred material volume. This block was then electroplated with pure Cu, and afterwards the resulting block was annealed at 1058 K. They found that the Mo wires had moved from their original position, which could only mean that Cu and Zn had different diffusion rates. Moreover, this changed the way solid diffusion was understood, since, the now called *Kirkendall effect* showed evidence of a vacancy diffusion mechanism instead of substitutional or ring mechanism, which were the ones believed to be driving binary diffusion in alloys at the time.

Vacancy sites are defects in the lattice, and are basically lattice sites which should be occupied by an atom if the crystal structure was perfect. Atoms use these empty lattice spaces to diffuse. A consequence of the Kirkendall effect is the fact that voids may form and in metals this implies deterioration in their mechanical, thermal and electrical properties. It should be noted that Huntington and Seitz [43], five years before Kirkendall's contribution, argued that indeed, it is the vacancy mechanism that drives diffusion, but because of WWII their work was overlooked.

In recent years the Kirkendall effect has been used to create hollow nanostructures, although the first example of using the Kirkendall effect to create hollow structures was by Aldinger [2]. Hollow nanocrystals were first produced by Yin *et al.* [115]. Gonzalez *et al.* [37] were able to synthesise different shapes of nanostructures such as spheres, cubes and tubes at room temperature. This type of structure has many possible applications. In biomedicine, they can be used for simultaneous diagnosis and therapy, and the hollow inside can be used to transport drugs and biomolecules and then release them in a controlled manner [4]. Piao *et al.* [83] used hollow nanocapsules of magnetite that not only were used as a drug delivery vehicle but as a T_2 magnetic resonance imaging contrast (MRI) agent.

A full review on the nanostructures and MRI can be found in [80]. In the lithium-ion batteries context they have been proposed to be included in the electrodes to enhance rate capability and cycling stability [106]. Hollow nanoparticles have also been reported to be good catalysts [48, 52]. A review on synthesis and applications of hollow nanostructures can be found in [55].

Mathematical models have been proposed to explain the Kirkendall effect. Fan *et al.* [26] describe a theory of the physics behind the Kirkendall effect, consisting of two stages: the first one involves the creation of small voids in the compound interface via bulk diffusion, and the second one which strongly relies on surface diffusion of the core material. They say that this model works for both nanospheres and nanotubes. Yu *et al.* [116] present a model with vacancy sources and sinks and solve it numerically. Jana *et al.* [44] create hollow nanoparticles and present a mathematical model that aims to capture the observed phenomena. The results of the model match the experimental data, but in it there is a free parameter chosen for that purpose. Furthermore, the boundary conditions do not seem to match the physical description of the problem.

In this paper we rigorously derive the governing equations for a substitutional binary diffusion problem and make sensible assumptions to reduce them in order to have an analytically tractable problem. We will pose a 1D problem, the simplest scenario possible in order to gain insight into the physics behind the Kirkendall effect, with the future goal in mind of being able to model the creation of hollow nanostructures.

In the following section we will derive expressions for the fluxes of the two species in a binary diffusion problem. In doing so, we obtain expressions for the concentration dependent diffusion coefficients. We will then derive the fluxes in terms of the fast diffuser and vacancies, since keeping track of the latter is crucial for our goal. After obtaining the governing equations for the problem we will use them in the development of a one dimensional test case in Section 6.3. In two limiting cases we can use asymptotic expansions to simplify the problem and give analytical solutions. These cases correspond to assuming that one species is much faster than the other or that they both diffuse at almost the same rate. We also provide a numerical solution to the full problem. In the results section we demonstrate that the analytical reduction of the diffusion coefficients is valid and thus the reduced governing equations can be used to treat this problem.

6.2 Substitutional diffusion

Consider a binary crystalline solid composed of three species: atomic species A, atomic species B, and vacancies V. We label the fast diffuser as species A, and the slow one B. The driving forces for the diffusion of species are the gradients of the chemical potentials μ_i, so the concentration fluxes of the components of the system are [57]

$$J_A = -L_{AA}\nabla\mu_A - L_{AB}\nabla\mu_B - L_{AV}\nabla\mu_V, \tag{6.1}$$

$$J_B = -L_{BA}\nabla\mu_A - L_{BB}\nabla\mu_B - L_{BV}\nabla\mu_V, \tag{6.2}$$

$$J_V = -L_{VA}\nabla\mu_A - L_{VB}\nabla\mu_B - L_{VV}\nabla\mu_V, \tag{6.3}$$

where L_{ij} are the kinetic transport coefficients. It holds that $L_{AB} = L_{BA}$, $L_{AV} = L_{VA}$, and $L_{BV} = L_{VB}$ [81]. In a perfect lattice region (free of dislocations, grain boundaries and surfaces) lattice sites are conserved, so

$$J_A + J_B + J_V = 0. \tag{6.4}$$

Substituting for the fluxes from (6.1)-(6.3) and equating the coefficients of the different chemical potentials leads to relations $L_{VA} = -(L_{AA} + L_{AB})$, $L_{VB} = -(L_{AB} + L_{BB})$ and $L_{VV} = -(L_{AV} + L_{BV})$. It also means that we only need two of the fluxes to fully define the system,

$$J_A = -L_{AA}\nabla(\mu_A - \mu_V) - L_{AB}\nabla(\mu_B - \mu_V), \tag{6.5}$$

$$J_B = -L_{AB}\nabla(\mu_A - \mu_V) - L_{BB}\nabla(\mu_B - \mu_V). \tag{6.6}$$

We write in terms of the fluxes of A and B to illustrate the fact that substitutional diffusion of an atom in a perfect lattice structure occurs via positional exchange with a neighbouring site.

The kinetic transport coefficients L_{ij} are defined as [58, 66]

$$L_{AA} = X_V X_A \Gamma_A \frac{\rho\lambda a^2}{k_B T}\left(1 - \frac{2X_B\Gamma_A}{\Lambda}\right), \tag{6.7}$$

$$L_{AB} = L_{BA} = \Gamma_A\Gamma_B X_A X_B X_V \frac{2\rho\lambda a^2}{k_B T\Lambda}, \tag{6.8}$$

$$L_{BB} = X_V X_B \Gamma_B \frac{\rho\lambda a^2}{k_B T}\left(1 - \frac{2X_A\Gamma_B}{\Lambda}\right), \tag{6.9}$$

where X_i are the mole fractions corresponding to the i-th species (and, by the definition of mole fraction, $X_A + X_B + X_V = 1$), ρ is the lattice site density, λ is a geometric factor that depends on crystal structure, a is the atomic hop distance, k_B is the Boltzmann constant, T is the temperature of the system, and Γ_A and Γ_B are the jump frequencies of species A and B, respectively. The jump frequency is the rate at which atoms jump to an adjacent available site. We denote $\Gamma = \Gamma_A/\Gamma_B > 1$, since A is the fast diffuser. A list of typical values of these parameters is given in Table 6.1. If species i is absent then the coefficients L_{ij} are such that $J_i = 0$. The parameter Λ is defined as [66]

$$\begin{aligned}\Lambda =&\frac{1}{2}(F_0+2)(X_A\Gamma_A + X_B\Gamma_B) - \Gamma_A - \Gamma_B + 2(X_A\Gamma_B + X_B\Gamma_A)+\\ &\sqrt{\left(\frac{1}{2}(F_0+2)(X_A\Gamma_A + X_B\Gamma_B) - \Gamma_A - \Gamma_B\right)^2 + 2F_0\Gamma_A\Gamma_B},\end{aligned} \tag{6.10}$$

where $F_0 = \frac{2f_0}{1-f_0}$, and f_0 is the correlation factor for a single component solid with the crystal structure of the A-B alloy. The fluxes are now well defined.

In order to derive explicit expressions for the fluxes involving the mole fractions of the atomic species, we define the new chemical potentials $\tilde{\mu}_A = \mu_A - \mu_V$ and $\tilde{\mu}_B = \mu_B - \mu_V$ which may be written as [116]

$$\tilde{\mu}_i = \frac{\partial G(X_A, X_B)}{\partial X_i}, \tag{6.11}$$

where G is the Gibbs free energy. According to the ideal mixing condition, the free Gibbs energy per lattice site in the A-B alloy with vacancies is

$$G(X_A, X_B) = k_B T \left[X_A \ln(X_A) + X_B \ln(X_B) + X_V \ln(X_V)\right]. \tag{6.12}$$

We can rewrite equations (6.5) and (6.6) as

$$J_A = -\rho\left(L_{AA}\frac{1}{\rho}\frac{\partial\tilde{\mu}_A}{\partial X_A} + L_{AB}\frac{1}{\rho}\frac{\partial\tilde{\mu}_B}{\partial X_A}\right)\nabla X_A - \rho\left(L_{AA}\frac{1}{\rho}\frac{\partial\tilde{\mu}_A}{\partial X_B} + L_{AB}\frac{1}{\rho}\frac{\partial\tilde{\mu}_B}{\partial X_B}\right)\nabla X_B, \tag{6.13}$$

$$J_B = -\rho\left(L_{BA}\frac{1}{\rho}\frac{\partial\tilde{\mu}_A}{\partial X_A} + L_{BB}\frac{1}{\rho}\frac{\partial\tilde{\mu}_B}{\partial X_A}\right)\nabla X_A - \rho\left(L_{BA}\frac{1}{\rho}\frac{\partial\tilde{\mu}_A}{\partial X_B} + L_{BB}\frac{1}{\rho}\frac{\partial\tilde{\mu}_B}{\partial X_B}\right)\nabla X_B. \tag{6.14}$$

The reason for keeping the ρ factor in this form will become apparent later.

If we define the diffusion coefficients as

$$\begin{pmatrix} D_{AA} & D_{AB} \\ D_{BA} & D_{BB} \end{pmatrix} = \begin{pmatrix} L_{AA} & L_{AB} \\ L_{BA} & L_{BB} \end{pmatrix} \begin{pmatrix} \frac{1}{\rho}\frac{\partial \tilde{\mu}_A}{\partial X_A} & \frac{1}{\rho}\frac{\partial \tilde{\mu}_A}{\partial X_B} \\ \frac{1}{\rho}\frac{\partial \tilde{\mu}_B}{\partial X_A} & \frac{1}{\rho}\frac{\partial \tilde{\mu}_B}{\partial X_B} \end{pmatrix}, \tag{6.15}$$

then the fluxes (6.13), (6.14) may be written in terms of the mole fractions

$$J_A = -\rho D_{AA}\nabla X_A - \rho D_{AB}\nabla X_B, \tag{6.16}$$

$$J_B = -\rho D_{BA}\nabla X_A - \rho D_{BB}\nabla X_B. \tag{6.17}$$

6.2.1 Fluxes in terms of the fast diffuser and vacancies

In binary diffusion it is the concentration of A and B that are of practical interest. However, the process is only possible due to the presence of vacancies. The vacancy concentration is typically 6 orders of magnitude smaller than X_A or X_B, so the details of the evolution of X_V are easily lost in a numerical solution. For this reason, from now on we will work with the fast diffuser A and the vacancies. This means working with the two fluxes J_A and J_V. Since lattice sites are conserved, $\sum_i X_i = 1$, we may write

$$\nabla X_A + \nabla X_B + \nabla X_V = 0. \tag{6.18}$$

Using equations (6.4), (6.16), (6.17) and (6.18), we then obtain

$$J_A = -\rho D^V_{AA}\nabla X_A + \rho D_{AV}\nabla X_V, \tag{6.19}$$

$$J_V = \rho D_{VA}\nabla X_A - \rho D_{VV}\nabla X_V, \tag{6.20}$$

where the modified diffusion coefficients are

$$\begin{aligned} D^V_{AA} &= D_{AA} - D_{AB}, & D_{AV} &= D_{AB}, \\ D_{VA} &= D_{BA} + D_{AA} - D_{BB} - D_{AB}, & D_{VV} &= D_{BB} + D_{AB}. \end{aligned} \tag{6.21}$$

Fick's second law states that the rate of change of concentration in time is equal to the divergence of the flux. Noting that the concentration may be written in terms of the mole fraction, $C_i = \rho X_i$, we find diffusion equations for X_A and X_V,

$$\frac{\partial X_A}{\partial t} = -\frac{1}{\rho}\nabla \cdot J_A = \nabla \cdot \left(D^V_{AA}\nabla X_A\right) - \nabla \cdot \left(D_{AV}\nabla X_V\right), \tag{6.22}$$

$$\frac{\partial X_V}{\partial t} = -\frac{1}{\rho}\nabla \cdot J_V = -\nabla \cdot \left(D_{VA}\nabla X_A\right) + \nabla \cdot \left(D_{VV}\nabla X_V\right). \tag{6.23}$$

Note that the ρ term has now disappeared in the governing equations.

6.2.2 Diffusion coefficients

The diffusion coefficients defined by equations (6.15), (6.21) are very complex, making it difficult to identify the dominant mechanisms. Consequently we will now analyse the expressions for D_{AA}, D_{AB}, D_{BA} and D_{BB}. Starting with D_{AA} we note that it consists of two terms,

$$\begin{aligned} L_{AA}\frac{1}{\rho}\frac{\partial\tilde{\mu}_A}{\partial X_A} &= X_V X_A \Gamma_A \frac{\rho\lambda a^2}{k_B T}\left(1-\frac{2X_B\Gamma_A}{\Lambda}\right)\frac{1}{\rho}k_B T\left(\frac{1}{X_A}+\frac{1}{X_V}\right) \\ &= \Gamma_A\lambda a^2\left(1-\frac{2X_B\Gamma_A}{\Lambda}\right)(X_V+X_A), \end{aligned} \tag{6.24}$$

$$L_{AB}\frac{\partial\tilde{\mu}_B}{\partial X_A} = X_V X_A X_B \Gamma_A\Gamma_B\frac{2\rho\lambda a^2}{k_B T\Lambda}\frac{1}{\rho}\frac{k_B T}{X_V} = X_A X_B\Gamma_A\Gamma_B\frac{2\lambda a^2}{\Lambda}, \tag{6.25}$$

which leads to

$$D_{AA} = \lambda a^2\Gamma_A\left[\left(1-\frac{2X_B\Gamma_A}{\Lambda}\right)(X_V+X_A)+\frac{2X_A X_B\Gamma_B}{\Lambda}\right]. \tag{6.26}$$

By a similar process we obtain

$$D_{AB} = \lambda a^2\Gamma_A\left[X_A\left(1-\frac{2X_B\Gamma_A}{\Lambda}\right)+\frac{2X_A\Gamma_B}{\Lambda}(X_V+X_B)\right], \tag{6.27}$$

$$D_{BA} = \lambda a^2\Gamma_B\left[\frac{2X_B\Gamma_A}{\Lambda}(X_V+X_A)+X_B\left(1-\frac{2X_A\Gamma_B}{\Lambda}\right)\right], \tag{6.28}$$

$$D_{BB} = \lambda a^2\Gamma_B\left[\frac{2X_A X_B\Gamma_A}{\Lambda}+\left(1-\frac{2X_A\Gamma_B}{\Lambda}\right)(X_V+X_B)\right]. \tag{6.29}$$

Substituting (6.26)-(6.29) into (6.21) gives

$$D^V_{AA} = \lambda a^2\Gamma_A X_V\left[1-\frac{2}{\Lambda}\left(\Gamma_A(1-X_V)-X_A(\Gamma_A-\Gamma_B)\right)\right], \tag{6.30}$$

$$D_{AV} = \lambda a^2\Gamma_A X_A\left[1-\frac{2}{\Lambda}\left((1-X_A)(\Gamma_A-\Gamma_B)-\Gamma_A X_V\right)\right], \tag{6.31}$$

$$D_{VA} = \lambda a^2 X_V\left[(\Gamma_A-\Gamma_B)\left(1-\frac{2}{\Lambda}\left((1-X_A-X_V)\Gamma_A+\Gamma_B X_A\right)\right)\right], \tag{6.32}$$

$$D_{VV} = \lambda a^2\left[X_A(\Gamma_A-\Gamma_B)\left(1-\frac{2}{\Lambda}\left((1-X_A)(\Gamma_A-\Gamma_B)-X_V\Gamma_A\right)\right)+\Gamma_B\right]. \tag{6.33}$$

The governing equations (6.22)-(6.23) for the diffusion of species A and the vacancies are now well defined.

parameter	name	value	units
ρ	lattice site density	6.021×10^{28}	atoms/m^3
λ	geometric factor	$1/6$	-
f_0	geometric correlation factor	0.7815	-
F	$2f_0/(1-f_0)$	7.1533	-
a	lattice constant	4.05×10^{-10}	m
Γ_B	hopping frequency of slow diffuser	10^7	Hz
Γ	ratio of hop frequencies of slow and fast diffuser	-	-
Γ_A	hopping frequency of fast diffuser	$\Gamma\Gamma_B$	Hz
$X_{V,0}$	initial vacancy mole fraction	10^{-6}	-

Table 6.1: Typical parameter values. They are quite similar as the ones corresponding to aluminium being the slow diffuser. Data taken from [59, 116].

6.3 One dimensional case

Consider an insulated one-dimensional bar of length $2l$. At $t = 0$ the side $x \in [-l, 0]$ is made of material A (and a proportion of vacancies), and the side $x \in [0, l]$ is made of material B (and a proportion of vacancies). A sketch of the situation is shown in Figure 6.1.

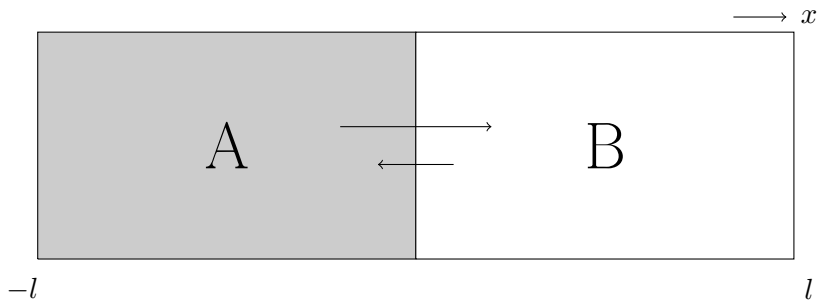

Figure 6.1: Sketch of the one dimensional bar case.

For $t > 0$ the diffusion of species is defined by the 1D forms of (6.22)-(6.23)

$$\frac{\partial X_A}{\partial t} = \frac{\partial}{\partial x}\left(D^V_{AA}\frac{\partial X_A}{\partial x}\right) - \frac{\partial}{\partial x}\left(D_{AV}\frac{\partial X_V}{\partial x}\right), \tag{6.34}$$

$$\frac{\partial X_V}{\partial t} = -\frac{\partial}{\partial x}\left(D_{VA}\frac{\partial X_A}{\partial x}\right) + \frac{\partial}{\partial x}\left(D_{VV}\frac{\partial X_V}{\partial x}\right), \tag{6.35}$$

with the diffusion coefficients given in (6.30)-(6.33), subject to boundary conditions

$$\left.\frac{\partial X_A}{\partial x}\right|_{x=\pm l} = \left.\frac{\partial X_V}{\partial x}\right|_{x=\pm l} = 0. \tag{6.36}$$

The boundary conditions confine the material to $x \in [-l, l]$. In practice the Kirkendall effect can cause the boundaries to move. We will not study this situation here. The initial conditions are

$$X_A(x,0) = \begin{cases} X_{A,\text{ini}} & \text{if} \quad -l < x < 0, \\ 0 & \text{if} \quad 0 < x < l, \end{cases} \qquad X_B(x,0) = \begin{cases} 0 & \text{if} \quad -l < x < 0, \\ X_{B,\text{ini}} & \text{if} \quad 0 < x < l, \end{cases}$$

$$X_V(x,0) = X_{V,\text{ini}}, \tag{6.37}$$

where $X_{A,\text{ini}}$, $X_{B,\text{ini}}$, and $X_{V,\text{ini}}$ denote the constant initial mole fractions of material A, B, and vacancies, respectively, and $X_{i,\text{ini}} = 1 - X_{V,\text{ini}}$, $i =$ A, B.

We now non-dimensionalise the variables

$$\hat{x} = \frac{x}{l}, \qquad \hat{t} = \frac{\bar{D}_{BB}}{l^2} t, \tag{6.38}$$

where $\bar{D}_{BB} = \lambda a^2 \Gamma_B$. We also rescale $\hat{\Gamma}_i = \Gamma_i / \Gamma_B$. Immediately dropping the hats the governing equations become

$$\frac{\partial X_A}{\partial t} = \frac{\partial}{\partial x}\left(D^V_{AA}\frac{\partial X_A}{\partial x}\right) - \frac{\partial}{\partial x}\left(D_{AV}\frac{\partial X_V}{\partial x}\right), \tag{6.39}$$

$$\frac{\partial X_V}{\partial t} = -\frac{\partial}{\partial x}\left(D_{VA}\frac{\partial X_A}{\partial x}\right) + \frac{\partial}{\partial x}\left(D_{VV}\frac{\partial X_V}{\partial x}\right), \tag{6.40}$$

where

$$D^V_{AA} = \Gamma X_V \left[1 - \frac{2}{\Lambda}\left(\Gamma(1 - X_V) - X_A(\Gamma - 1)\right)\right], \tag{6.41}$$

$$D_{AV} = \Gamma X_A \left[1 - \frac{2}{\Lambda}\left((1 - X_A)(\Gamma - 1) - \Gamma X_V\right)\right], \tag{6.42}$$

$$D_{VA} = X_V \left[(\Gamma - 1)\left(1 - \frac{2}{\Lambda}\left(\Gamma(1 - X_V) - X_A(\Gamma - 1)\right)\right)\right], \tag{6.43}$$

$$D_{VV} = X_A(\Gamma - 1)\left[1 - \frac{2}{\Lambda}\left((1 - X_A)(\Gamma - 1) - X_V\Gamma\right)\right] + 1. \tag{6.44}$$

The boundary conditions are unchanged (although now applied at $x = \pm 1$).

6.3.1 Approximate solutions

We wish to solve the problem defined by (6.39)-(6.40) and appropriate boundary conditions. In order to do so we try to simplify the problem. A sensible assumption to make is that $X_V = \mathcal{O}(\epsilon)$, where $\epsilon \ll 1$ is taken to be the initial vacancy mole fraction. We write $X_A = X_{A,0} + \epsilon X_{A,1}$ and $X_V = \epsilon X_{V,1}$. The governing equations (6.39)-(6.40) to first order in ϵ in a regular asymptotic expansion are

$$\frac{\partial X_{A,0}}{\partial t} + \epsilon \frac{\partial X_{A,1}}{\partial t} = \epsilon \frac{\partial}{\partial x}\left(D^V_{AA,1} \frac{\partial X_{A,0}}{\partial x} \right) - \epsilon \frac{\partial}{\partial x}\left(D_{AV,0} \frac{\partial X_{V,1}}{\partial x} \right), \tag{6.45}$$

$$\epsilon \frac{\partial X_{V,1}}{\partial t} = -\epsilon \frac{\partial}{\partial x}\left(D_{VA,1} \frac{\partial X_{A,0}}{\partial x} \right) + \epsilon \frac{\partial}{\partial x}\left(D_{VV,0} \frac{\partial X_{V,1}}{\partial x} \right). \tag{6.46}$$

The four diffusion coefficients come from the expansions

$$\begin{aligned} D^V_{AA} &= \epsilon D^V_{AA,1} + \mathcal{O}(\epsilon^2), & D_{AV} &= D_{AV,0} + \epsilon D_{AV,1} + \mathcal{O}(\epsilon^2), \\ D_{VA} &= \epsilon D_{VA,1} + \mathcal{O}(\epsilon^2), & D_{VV} &= D_{VV,0} + \epsilon D_{VV,1} + \mathcal{O}(\epsilon^2), \end{aligned} \tag{6.47}$$

where

$$D^V_{AA,1} = \Gamma X_{V,1}\left[1 - \frac{2}{\Lambda}\left(\Gamma(1 - X_{A,0}) + X_{A,0} \right) \right], \tag{6.48}$$

$$D_{AV,0} = \Gamma X_{A,0}\left[1 - \frac{2}{\Lambda}(1 - X_{A,0})(\Gamma - 1) \right], \tag{6.49}$$

$$D_{VA,1} = X_{V,1}(\Gamma - 1)\left[1 - \frac{2}{\Lambda}\left(\Gamma(1 - X_{A,0}) + X_{A,0} \right) \right], \tag{6.50}$$

$$D_{VV,0} = X_{A,0}(\Gamma - 1)\left[1 - \frac{2}{\Lambda}(1 - X_{A,0})(\Gamma - 1) \right] + 1. \tag{6.51}$$

The expression used for Λ in the equations above (6.48)-(6.51), to leading order, is

$$\begin{aligned} \Lambda =& \frac{1}{2}(F_0 + 2)(X_{A,0}\Gamma + 1 - X_{A,0}) - \Gamma - 1 + 2\left(X_{A,0} + \Gamma(1 - X_{A,0}) \right) + \\ & \sqrt{\left(\frac{1}{2}(F_0 + 2)(X_{A,0}\Gamma + 1 - X_{A,0}) - \Gamma - 1 \right)^2 + 2F_0\Gamma} \end{aligned} \tag{6.52}$$

To first order in ϵ the problem to solve is now

$$\frac{\partial X_{A,0}}{\partial t} = 0, \tag{6.53}$$

$$\frac{\partial X_{A,1}}{\partial t} = \frac{\partial}{\partial x}\left(D^V_{AA,1} \frac{\partial X_{A,0}}{\partial x} \right) - \frac{\partial}{\partial x}\left(D_{AV,0} \frac{\partial X_{V,1}}{\partial x} \right), \tag{6.54}$$

$$\frac{\partial X_{V,1}}{\partial t} = -\frac{\partial}{\partial x}\left(D_{VA,1} \frac{\partial X_{A,0}}{\partial x} \right) + \frac{\partial}{\partial x}\left(D_{VV,0} \frac{\partial X_{V,1}}{\partial x} \right), \tag{6.55}$$

with boundary conditions

$$\left.\frac{\partial X_{A,0}}{\partial x}\right|_{x=\pm 1} = \left.\frac{\partial X_{A,1}}{\partial x}\right|_{x=\pm 1} = \left.\frac{\partial X_{V,1}}{\partial x}\right|_{x=\pm 1} = 0. \tag{6.56}$$

Equation (6.53) tells us that in this time scale, $X_{A,0}$ is in steady state and so is defined by the initial condition, $X_{A,0} = f(x) = X_A(x,0)$. This indicates the need to study the slow time dynamics; since on the normal time scale we find that $X_{A,0}$ is constant in time we will not see any behaviour of interest. For this reason, we rescale time as $\tau = \epsilon t$. The problem then becomes, to first order in ϵ,

$$\frac{\partial X_{A,0}}{\partial \tau} = \frac{\partial}{\partial x}\left(D^V_{AA,1}\frac{\partial X_{A,0}}{\partial x}\right) - \frac{\partial}{\partial x}\left(D_{AV,0}\frac{\partial X_{V,1}}{\partial x}\right), \tag{6.57}$$

$$0 = -\frac{\partial}{\partial x}\left(D_{VA,1}\frac{\partial X_{A,0}}{\partial x}\right) + \frac{\partial}{\partial x}\left(D_{VV,0}\frac{\partial X_{V,1}}{\partial x}\right), \tag{6.58}$$

subject to boundary conditions (6.56).

Special cases

In the previous section although we could simplify the governing equations we were not able to provide any analytical solutions and thus not much insight into what drives this process. In the following we study two particular cases of the problem in which we are able to find analytical solutions.

Case $\Gamma \gg 1$

Assuming A diffuses much faster than B, that is, $\Gamma \gg 1$, (6.48)-(6.51) reduce to

$$\begin{aligned} D^V_{AA} &\sim \Gamma X_V, & D_{AV} &\sim \Gamma X_A, \\ D_{VA} &\sim (\Gamma - 1)\, X_V, & D_{VV} &\sim (\Gamma - 1)\, X_A + 1. \end{aligned} \tag{6.59}$$

These reductions hold provided $X_{A,0}$ is not close to zero. The problem becomes

$$\frac{\partial X_{A,0}}{\partial t} = 0, \tag{6.60}$$

$$\frac{\partial X_{A,1}}{\partial t} = \Gamma X_{V,1}\frac{\partial^2 X_{A,0}}{\partial x^2} - \Gamma X_{A,0}\frac{\partial^2 X_{V,1}}{\partial x^2}, \tag{6.61}$$

$$\frac{\partial X_{V,1}}{\partial t} = -(\Gamma - 1)X_{V,1}\frac{\partial^2 X_{A,0}}{\partial x^2} + [1 + (\Gamma - 1)X_{A,0}]\frac{\partial^2 X_{V,1}}{\partial x^2}, \tag{6.62}$$

with boundary conditions (6.56). The system above leads again to $X_{A,0} = X_A(x,0)$, which is the Heaviside function of $-x$. Although equation (6.58) can be integrated it does not give

a simple relation between $X_{A,0}$ and $X_{V,1}$ due to the nonlinear diffusion coefficients. Again analytical progress is difficult so we now focus on the slow time dynamics.

Slow time dynamics

Consider the system defined in (6.60)-(6.62) and rescale time so that $\tau = \epsilon t$. This leads to

$$\frac{\partial X_{A,0}}{\partial \tau} = \frac{\partial}{\partial x}\left(\Gamma X_{V,1}\frac{\partial X_{A,0}}{\partial x}\right) - \frac{\partial}{\partial x}\left(\Gamma X_{A,0}\frac{\partial X_{V,1}}{\partial x}\right), \tag{6.63}$$

$$0 = -\frac{\partial}{\partial x}\left((\Gamma-1)\,X_{V,1}\frac{\partial X_{A,0}}{\partial x}\right) + \frac{\partial}{\partial x}\left([1+(\Gamma-1)X_{A,0}]\,\frac{\partial X_{V,1}}{\partial x}\right). \tag{6.64}$$

Integrating (6.64) yields

$$-(\Gamma-1)\,X_{V,1}\frac{\partial X_{A,0}}{\partial x} + [1+(\Gamma-1)X_{A,0}]\,\frac{\partial X_{V,1}}{\partial x} = 0, \tag{6.65}$$

where the constant of integration is zero because of the boundary conditions (6.56). Rearranging and integrating by substitution yields

$$X_{V,1}(x) = X_{V,1}(-1)\left(\frac{1+(\Gamma-1)X_{A,0}(x)}{1+(\Gamma-1)X_{A,0}(-1)}\right), \tag{6.66}$$

where $X_{V,1}(-1)$ is picked such that $\int_{-1}^{1} X_{V,1}(x)\,\mathrm{d}x = 1$. Let $M_0 = \int_{-1}^{1} X_{A,0}(x)\,\mathrm{d}x$. Then equation (6.65) can be written as

$$X_{V,1}(x) = \frac{1+(\Gamma-1)X_{A,0}(x)}{2+(\Gamma-1)M_0}. \tag{6.67}$$

Substituting (6.67) into equation (6.63) gives

$$\frac{\partial X_{A,0}}{\partial \tau} = \frac{\Gamma}{2+(\Gamma-1)M_0}\frac{\partial^2 X_{A,0}}{\partial x^2}. \tag{6.68}$$

This indicates that on a slow time scale the vacancies will adapt to A as described in equation (6.67) and A will follow a simple diffusion process described by (6.68).

Let us define $\alpha = \Gamma/(2+(\Gamma-1)M_0)$. Solving equation (6.68) subject to (6.56) is a simple case of separation of variables,

$$X_{A,0}(x,\tau) = \frac{M_0}{2} + \sum_{k=1}^{\infty} C_k \cos\left(\frac{k\pi}{2}(x+1)\right) e^{-\left(\frac{k\pi}{2}\right)^2 \alpha\tau}, \tag{6.69}$$

where

$$C_k = \int_{-1}^{1} X_{A,0}(x,0)\cos\left(\frac{k\pi}{2}(x+1)\right)\mathrm{d}x. \tag{6.70}$$

The C_k values can be computed analytically for given initial data such as (6.37). In this case C_k are only nonzero when k is odd,

$$C_k = (-1)^{k+1}\frac{2X_{A,\text{ini}}}{(2k-1)\pi}. \tag{6.71}$$

Consequently, via equation (6.67), we obtain

$$X_{V,1}(x,\tau) = \frac{\alpha}{\Gamma}\left(1+(\Gamma-1)\left[\frac{M_0}{2}+\sum_{k=1}^{\infty}C_k\cos\left(\frac{(2k-1)\pi}{2}(x+1)\right)e^{-\left(\frac{(2k-1)\pi}{2}\right)^2\alpha\tau}\right]\right). \tag{6.72}$$

Case $\Gamma \sim 1$

Another limit where progress can be made is $\Gamma \sim 1$. This means that both species diffuse at similar rates (although A is still faster). This reduces the diffusion coefficients (6.48)-(6.51) to

$$\begin{aligned} D^V_{AA} &\sim \Gamma D_C X_V, & D_{AV} &\sim \Gamma X_A, \\ D_{VA} &\sim (\Gamma-1)\, D_C X_V, & D_{VV} &\sim (\Gamma-1)\, X_A + 1, \end{aligned} \tag{6.73}$$

where $D_C = 1 - 2/(F0+2)$ is constant. These reductions are valid for all X_A. We can no longer solve the problem analytically, but these expressions for the diffusion coefficients are much simpler than the original ones, and using them can further simplify the study of the Kirkendall effect.

However, it is possible to make analytical progress if we introduce a small error into the diffusion coefficients D_{AV} and D_{VV} so that

$$D_{AV} \sim \Gamma D_C X_A, \qquad D_{VV} \sim (\Gamma-1)\, D_C X_A + 1, \tag{6.74}$$

where using the parameter values of Table 6.1, $D_C = 0.7815$. As we will see later the errors resulting from this approximation are small. The concentration $X_{A,0}$ is now the same solution as in equation (6.69) but with $\alpha = D_C\Gamma/(2+(\Gamma-1)D_C M_0)$,

$$X_{A,0}(x,\tau) = \frac{M_0}{2}+\sum_{k=1}^{\infty}C_k\cos\left(\frac{(2k-1)\pi}{2}(x+1)\right)e^{-\left(\frac{(2k-1)\pi}{2}\right)^2\alpha\tau}. \tag{6.75}$$

For the concentration of vacancies $X_{V,1}$ we find

$$X_{V,1}(x,\tau) = \frac{\alpha}{\Gamma D_C}\left(1+(\Gamma-1)D_C\left[\frac{M_0}{2}+\sum_{k=1}^{\infty}C_k\cos\left(\frac{k\pi}{2}(x+1)\right)e^{-\left(\frac{k\pi}{2}\right)^2\alpha\tau}\right]\right). \tag{6.76}$$

6.3.2 Numerical solution of the slow time dynamics

Let u_i and v_i be the average values of mole fractions $X_{A,0}$ and $X_{V,1}$, respectively, over the interval $(x_{i-1/2}, x_{i+1/2})$ of length h, centered at x_i. We introduce the vectors $\mathbf{Y}$ and $\mathbf{Z}$ which represent the interpolated values of u and v falling on the subinterval end points. We have that

$$Y_i = u_{i+1/2} = \frac{u_i + u_{i+1}}{2}, \qquad i = 1, \ldots, I+1, \tag{6.77}$$

$$Z_i = v_{i+1/2} = \frac{v_i + v_{i+1}}{2}, \qquad i = 1, \ldots, I+1. \tag{6.78}$$

The right-hand side of equation (6.57) can be discretised as

$$f_i = \frac{1}{h}\left[(Q_i - q_i) - (Q_{i-1} - q_{i-1})\right], \tag{6.79}$$

where

$$Q_i = \Gamma Z_i \left[1 - \frac{2}{\Lambda(Y_i)}\left(\Gamma(1-Y_i) + Y_i\right)\right] \frac{u_{i+1} - u_i}{h}, \qquad i = 1, \ldots, I+1, \tag{6.80}$$

$$q_i = \Gamma Y_i \left[1 - \frac{2}{\Lambda(Y_i)}(1-Y_i)(\Gamma - 1)\right] \frac{v_{i+1} - v_i}{h}, \qquad i = 1, \ldots, I+1. \tag{6.81}$$

The function $\Lambda(Y_i)$ is approximated analytically from (6.10) as

$$\begin{aligned}\Lambda(Y_i) =& \frac{1}{2}(F_0+2)(Y_i\Gamma + (1-Y_i)) - \Gamma_A - 1 + 2(Y_i + (1-Y_i)\Gamma) \\ &+ \sqrt{\left(\frac{1}{2}(F_0+2)(Y_i\Gamma + (1-Y_i)) - \Gamma - 1\right)^2 + 2F_0\Gamma} \quad + \quad \mathcal{O}(\epsilon).\end{aligned} \tag{6.82}$$

The discretisation of the right-hand side of equation (6.58) is approximated similarly as

$$g_i = \frac{1}{h}\left[(-P_i + p_i) - (-P_{i-1} + p_{i-1})\right], \tag{6.83}$$

where

$$P_i = Z_i(\Gamma - 1)\left[1 - \frac{2}{\Lambda(Y_i)}\left(\Gamma_A(1-Y_i) + \Gamma_B Y_i\right)\right] \frac{u_{i+1} - u_i}{h}, \qquad i = 1, \ldots, I+1, \tag{6.84}$$

$$p_i = \left(Y_i(\Gamma - 1)\left[1 - \frac{2}{\Lambda(Y_i)}(1-Y_i)(\Gamma_A - \Gamma_B)\right] + 1\right) \frac{v_{i+1} - v_i}{h}, \quad i = 1, \ldots, I+1. \tag{6.85}$$

The boundary conditions (6.56) transform into

$$f_1 = \frac{u_2 - u_1}{h} = 0, \tag{6.86}$$

$$f_{I+2} = \frac{u_{I+2} - u_{I+1}}{h} = 0, \tag{6.87}$$

$$g_1 = \frac{v_2 - v_1}{h} = 0, \tag{6.88}$$

$$g_{I+2} = \frac{v_{I+2} - v_{I+1}}{h} = 0, \tag{6.89}$$

where ghost cells 1 and $I + 2$ are introduced outside the domain.

We define the mass matrix $\mathbf{M}$ as

$$\mathbf{M} = \begin{array}{c} \\ 1 \\ 2 \\ \\ I \\ I{+}1 \\ I{+}2 \\ \vdots \\ 2(I{+}2) \end{array} \begin{pmatrix} 1 & 0 & \cdots & 0 & 0 & \dots & 0 \\ 0 & 1 & \cdots & 0 & 0 & \dots & 0 \\ \vdots & \vdots & \ddots & \vdots & \vdots & \ddots & \vdots \\ 0 & 0 & \cdots & 1 & 0 & \cdots & 0 \\ 0 & 0 & \cdots & 0 & 0 & \dots & 0 \\ 0 & 0 & \cdots & 0 & 0 & \dots & 0 \\ \vdots & \ddots & \vdots & \vdots & \ddots & \vdots & \\ 0 & 0 & \cdots & 0 & 0 & \cdots & 0 \end{pmatrix},$$

$\mathbf{F} = (f_2, \dots, f_{I+1}, f_1, f_{I+2}, g_1, \dots, g_{I+2})$, and $\mathbf{U} = (\mathbf{u}, \mathbf{v})$. Then we can write the problem as

$$\mathbf{M}\frac{\partial \mathbf{U}}{\partial t} = \mathbf{F}(\mathbf{U}). \tag{6.90}$$

The unknowns are u_i, v_i, for $i = 1, \dots, I + 2$. Equation (6.90) can be solved easily via the ODE routines in MATLAB. We use the `ode15s` routine.

6.4 Results

In this section we present the results of the one-dimensional case. The parameter values used can be found in Table 6.1.

The fast time system is defined by equations (6.53)-(6.55). The initial conditions are $X_A(x, 0) = H(-x)$ and $X_V(x, 0) = 0.5$. The second time regime corresponds to $t \gg 1$, $\tau = \epsilon t$, and is described by equations (6.57)-(6.58). Figure 6.2 displays the steady-state (large time) solutions for (6.53)-(6.55), the two curves represent $X_{A,0}$ (solid) and $X_{V,1}$ (dashed). These provide the initial conditions, $\tau = 0$, for (6.57)-(6.58). Both solutions show

that distributions reflect the Heaviside initial condition for X_A. On this time-scale there is no noticeable movement of X_A, but there has been a significant shift in the vacancies (which indicates that there has been movement of X_A, X_B but, since they have a much larger volume fraction it cannot be observed in the figure). The amount of vacancies that move depends strongly on Γ. When $\Gamma = 1.5$, that is A diffuses only slightly faster than B the redistribution of vacancies is relatively small, from the initial value of 0.5 to 0.6 on the left hand side which is balanced by 0.4 on the right hand side. When A diffuses much faster than B, in this example $\Gamma = 100$, nearly all vacancies move to the left hand side. This is easily explained: A and B having a similar jump frequency means that more or less the number of exchanges between A and a vacancy, and B and a vacancy is the same, thus the increase of V on the left hand side of the bar is small. On the other hand, $\Gamma \gg 1$ means that a large number of A atoms are going to exchange position with vacancies for every B atom that is able to do this type of exchange. The only way to compensate this difference is via vacancy lattice spaces, that end up where A was at the beginning of the process.

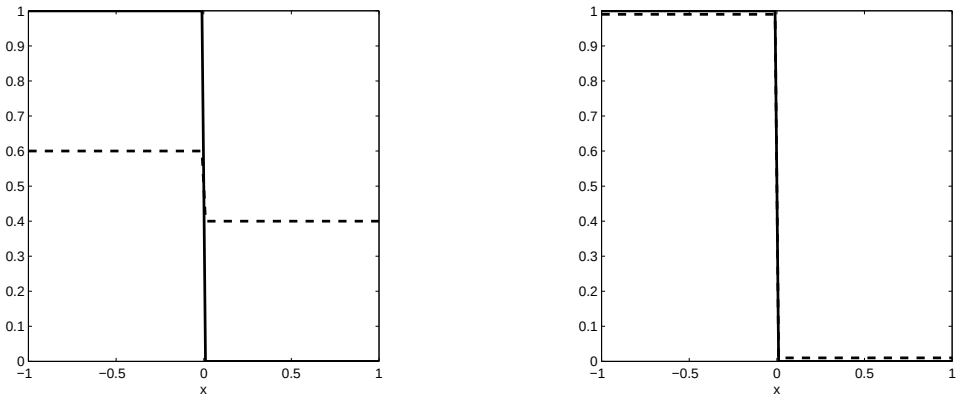

(a) $\Gamma = 1.5$. **(b)** $\Gamma = 100$.

Figure 6.2: Solution of equations (6.57)-(6.58). $X_{A,0}$ (solid) and $X_{V,1}$ (dashed) when $\tau \to 0$ for different Γ values.

In Figure 6.3 we compare the numerical solution (solid) of $X_{A,0}$ (left) and $X_{V,1}$ (right) as described in Section 6.3.2 to the large Γ approximate analytic solution (dashed) given by equations (6.69) and (6.72), respectively. We take 10 terms in the series to plot the solutions. We choose $\Gamma = 100$ (Figure 6.3(a), 6.3(b)), $\Gamma = 10$ (Figure 6.3(c), 6.3(d)), and

$\Gamma = 1.5$ (Figure 6.3(e), 6.3(f)). As expected, for $\Gamma = 100$, there is excellent agreement between the numerical and analytical solutions. The agreement deteriorates as Γ decreases, however, even when $\Gamma = 1.5$ the difference in X_A on the interval $x \in [-1, 0]$ is only around 7%. On the interval $[0, 1]$ the difference is larger, this is a result of the simplification of the diffusion coefficients under large Γ (equation (6.59)) which is valid provided $X_{A,0}$ is not close to zero. The error is most noticeable for small times and large Γ near $x = 1$. However, as time increases and so does X_A the error also decreases. So, despite the fact that the simplification requires the assumptions that $\Gamma \gg 1$ and $X_{A,0}$ is not close to zero, the errors for $\Gamma = 1.5,\ 10$ are reasonable (Figure 6.3(a), 6.3(b); 6.3(c), 6.3(d), respectively). In all cases for sufficiently large times the solutions tend to equilibrium, that is, $X_{A,0} = X_{V,1} = 0.5$. To give an idea of the process time-scale we note that when $l = 10$ nm in the figures $t_4 = 366$ s, when $10\,\mu$m, $t_4 = 3.66 \times 10^8$ s.

In Figure 6.4 we show a comparison of the full numerical solution (dashed), a numerical solution for the reduction where $\Gamma \sim 1$ (equation (6.73)) (dashed) and the analytical solution obtained using the approximation to D_{AV} and D_{VV} of equation (6.74) (dash-dotted) and taking 10 terms in the series. For the case where $\Gamma = 1.5$, Figure 6.4(a) and 6.4(b), the agreement between all three solutions is excellent although the analytical solution shows a slight error in the vacancy curves. It is interesting that the solution with an approximate diffusion coefficients is so accurate, since the error in D_{AV}, D_{VV} may be around 20%, so we must assume that these coefficients do not have a large effect on the solution. For larger $\Gamma = 10$ (Figure 6.4(c) and 6.4(d)), as expected, the discrepancy increases.

6.5 Conclusions

One of the main aims of this paper was to derive governing equations for substitutional binary diffusion, which may then be used in different geometries. Once derived we then reduced the equations to simulate substitutional diffusion in a one-dimensional bar. Our results indicated two distinct time-scales for the process: an initial fast time-scale where vacancies rapidly redistribute, followed by a slow redistribution to the constant steady-state.

The derived diffusion coefficients turned out to be quite complex, making the governing equations highly nonlinear. Useful reductions were only possible in a limited number of

cases. For $\Gamma \gg 1$, that is, one species diffuses much faster than the other we were able to obtain an analytical solution, via separation of variables. The reduction was based on the volume fraction of fast diffuser not being close to zero. In general results were excellent, except for at small times, near $x = 1$ where initially the volume fraction is zero. However, these errors decreased with time. For $\Gamma \sim 1$ analytical progress was made by slightly modifying two of the diffusion coefficients to give a system that could again be solved using separation of variables. Despite the fact that the error in diffusion coefficients could be close to 20% the errors arising from this modification were small.

Finally, we have developed a model which can be used readily to implement in other geometries or with different boundary conditions, opening the doors to model the creation of hollow nanostructures.

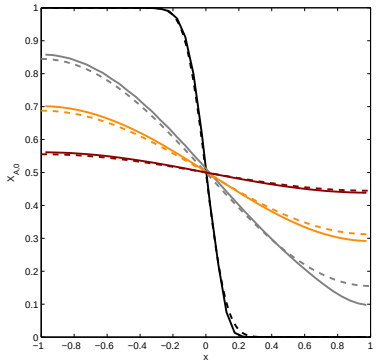

(a) $X_{A,0}$ for $\Gamma = 100$.

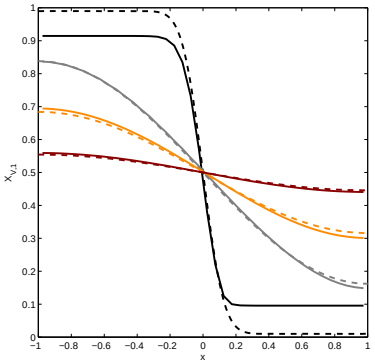

(b) $X_{V,1}$ for $\Gamma = 100$.

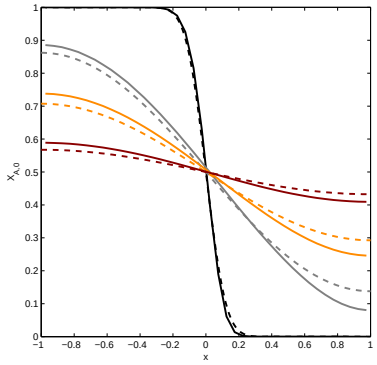

(c) $X_{A,0}$ for $\Gamma = 10$.

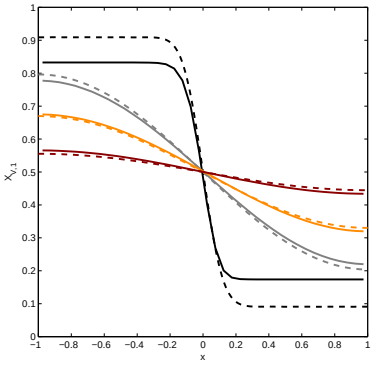

(d) $X_{V,1}$ for $\Gamma = 10$.

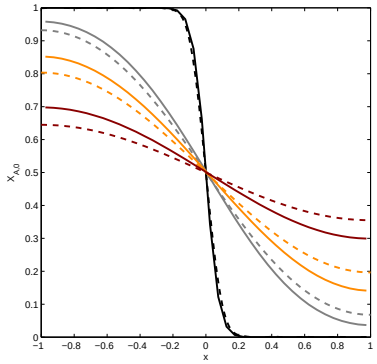

(e) $X_{A,0}$ for $\Gamma = 1.5$.

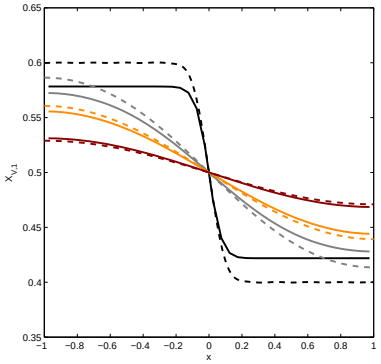

(f) $X_{V,1}$ for $\Gamma = 1.5$.

Figure 6.3: $X_{A,0}$ and $X_{V,1}$ as given by the numerical solution to the full problem (solid) and by the analytical solution to the reduced problem $\Gamma \gg 1$, equations (6.69) and (6.72) (dashed), for different Γ values. Different colours indicate different times: t_1 (black) $< t_2$ (gray) $< t_3$ (orange) $< t_4$ (dark red).

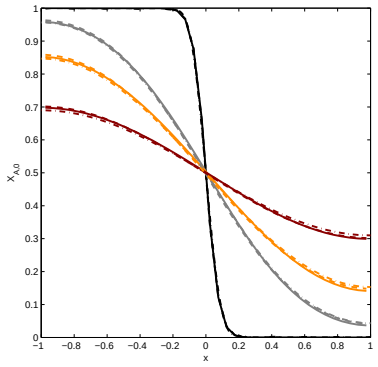

(a) $X_{A,0}$ for $\Gamma = 1.5$.

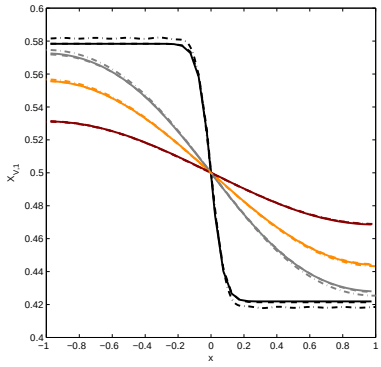

(b) $X_{V,1}$ for $\Gamma = 1.5$.

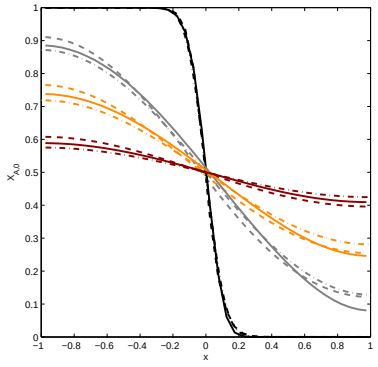

(c) $X_{A,0}$ for $\Gamma = 10$.

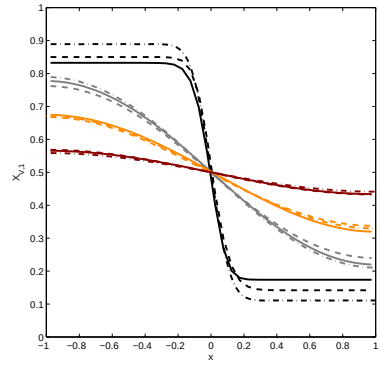

(d) $X_{V,1}$ for $\Gamma = 10$.

Figure 6.4: Numerical solution of $X_{A,0}$ and $X_{V,1}$ to the full problem (solid), numerical solution to the reduced problem $\Gamma \sim 1$ (dashed), and analytical solution to the reduced problem $\Gamma \sim 1$ using D_{AV} and D_{VV} in equations (6.75) and (6.76) (dash-dotted). Plots for different Γ values are presented. Different colours indicate different times: t_1 (black) $< t_2$ (gray) $< t_3$ (orange) $< t_4$ (dark red).

7 | Cellular automaton model for substitutional binary diffusion in solids

---

H. Ribera, B. Wetton, T. G. Myers

Cellular automaton model for substitutional binary diffusion in solids

Submitted to Journal of Cellular Automata

Impact factor: 0.698

Abstract

In this paper we use the cellular automaton (CA) approach to model one-dimensional binary diffusion in solids. Employing a very simple state change rule we define an asynchronous CA model and take its continuum limit to obtain the governing equations of the problem. We show that in the limit where the number of cells tends to infinity the CA model approaches a continuous model derived in previous work [88]. Thus, showing that the CA approach provides a new, simple method to study and model binary diffusion.

7.1 Introduction

A cellular automaton (CA) model consists of an n-th dimensional space partitioned into a discrete subset of n-dimensional volumes, which are called cells and are defined in a discrete

time. A finite list of possible states is defined for each cell, and each cell has one state. A local neighbourhood is defined for each cell at every time step. The state of a cell can be changed by a *state change rule*, which is a rule that allows the computation of the new state for the cell, and is dependent on other cells in the local neighbourhood [45]. Typically, this rule is fixed, that is, it is the same rule for all cells. It does not change over time and it is applied to all cells simultaneously. However, this rule can be stochastic, which means that the new states are chosen according to some probability distribution. This rule can also be applied to each individual cell independently and so the new state of a cell affects the calculation of states in neighbouring cells. Chopard *et al.* [19] presented the first application of cellular automaton to model diffusion on lattices. Subsequently many other CA approaches were applied to reaction-diffusion problems, see Boon *et al.* [11] and Weimar [107]. Then, it seems, there is a pause in the literature on using cellular automata approaches to work with the diffusion equation. Moreover, this type of modelling does not seem to have been applied to work with coupled, nonlinear diffusion problems, which are the focus of this paper.

The *Kirkendall effect* is the name given to the physical phenomenon whereby atomic diffusion occurs via a vacancy exchange mechanism instead of a substitutional or ring mechanism. Recently the Kirkendall effect has been used to create hollow nanostructures, which can be used in a variety of applications. In Aldinger [2] they present the first use of the Kirkendall effect to create hollow structures. The hollow permits their use in transporting drugs and biomolecules and then releasing them in a controlled manner [4]. Na *et al.* [80] present a review on nanostructrues and magnetic resonance imaging (MRI). These structures have also been proposed to enhance the rate capability and cycling stability in lithium-ion batteries [106]. Hollow nanoparticles have also been reported to be good catalysts [48, 52].

In an attempt to understand, and so better control the growth of hollow nanoparticles Ribera *et al.* [88] rigorously derived governing equations for the substitutional binary diffusion problem. Moreover, under sensible assumptions they reduce these governing equations in order to provide an analytically tractable problem. As a starting point they examine the one-dimensional problem of an insulated bar. In this paper we investigate the same problem but from the cellular automaton standpoint. This will help understand further the physical mechanisms behind the Kirkendall effect.

In the following section we present the model of Ribera *et al.* [88], which will be the starting point of the cellular automaton model, presented in Section 7.3. In the limit where the number of cells is large we prove that the CA model reduces to a special case of binary diffusion, where one species diffuses much faster than the other. In the Results section we verify this by showing that at large time and with a fast diffuser the CA model coincides with the continuum model. Further, since the computer speed reduces with N it is clear that the CA model is particularly useful at small scales, such as with nanostructures.

7.2 Continuum model for substitutional binary diffusion

Let us consider a binary crystalline solid composed of three species: atomic species A, atomic species B, and vacancies V. We label the fast diffuser as species A, and the slow one B. Since we are considering a perfect lattice, that means that the sum of all the fluxes is zero and then it is only necessary to work with the evolution of two species to fully define the problem.

Now consider an insulated one-dimensional bar of length $2l$. At $t = 0$ the side $x \in [-l, 0]$ is made of material A (and a proportion of vacancies), and the side $x \in [0, l]$ is made of material B (and a proportion of vacancies).

For $t > 0$ the diffusion of species is defined by

$$\frac{\partial X_A}{\partial t} = \frac{\partial}{\partial x}\left(D_{AA}^{V}\frac{\partial X_A}{\partial x}\right) - \frac{\partial}{\partial x}\left(D_{AV}\frac{\partial X_V}{\partial x}\right), \tag{7.1}$$

$$\frac{\partial X_V}{\partial t} = -\frac{\partial}{\partial x}\left(D_{VA}\frac{\partial X_A}{\partial x}\right) + \frac{\partial}{\partial x}\left(D_{VV}\frac{\partial X_V}{\partial x}\right), \tag{7.2}$$

where X_i are the mole fractions corresponding to the i-th species and the diffusion coefficients D_{AA}^{V}, D_{AV}, D_{VA} and D_{VV} vary nonlinearly with X_i [88]. In the limit where A diffuses much faster than B,

$$\begin{aligned} \hat{D}_{AA}^{V} &\sim \Gamma X_V, & \hat{D}_{AV} &\sim \Gamma X_A, \\ \hat{D}_{VA} &\sim (\Gamma - 1)\, X_V, & \hat{D}_{VV} &\sim [(\Gamma - 1)\, X_A + 1]\,. \end{aligned} \tag{7.3}$$

The boundary conditions are

$$\left.\frac{\partial X_A}{\partial x}\right|_{x=\pm l} = \left.\frac{\partial X_V}{\partial x}\right|_{x=\pm l} = 0, \tag{7.4}$$

and the initial conditions are

$$X_A(x,0) = \begin{cases} X_{A,\text{ini}} & \text{if } -1 < x < 0, \\ 0 & \text{if } 0 < x < 1, \end{cases} \qquad X_B(x,0) = \begin{cases} 0 & \text{if } -1 < x < 0, \\ X_{B,\text{ini}} & \text{if } 0 < x < 1, \end{cases}$$

$$X_V(x,0) = X_{V,\text{ini}}, \tag{7.5}$$

where $X_{A,\text{ini}}$, $X_{B,\text{ini}}$, and $X_{V,\text{ini}}$ denote the constant initial mole fractions of material A, B, and vacancies, respectively, and $X_{i,\text{ini}} = 1 - X_{V,\text{ini}}$, for $i =$ A, B.

In the following section we will show that the CA model reduces to (7.1), (7.2) in the appropriate limit.

7.3 Cellular automaton model

In order to define the cellular automaton model for the one-dimensional problem discussed in §7.2 we are going to define a two-dimensional space of size $N \times N$ that is partitioned into two-dimensional 1×1 cells. This would correspond to a two dimensional lattice of $N \times N$ atoms, in which each cell corresponds to one atomic site. Thus, the list of states for each cell in the CA model are "A atom", "B atom", and "vacancy V". The grid is considered to be periodic on the top/bottom edges. The model presented here will be asynchronous, that is, at each time step only one cell will be picked to apply the state change rule. Since physically atomic diffusion happens via vacancy exchange, it makes sense that the only cells in our CA grid that change state are those situated next to a vacancy cell and the vacancy cells themselves. For this reason, at each time step we only pick cells that represent vacancies to apply the change of state rule. Moreover, the choice of which vacancy cell is picked is done at random. We define the local neighbourhood of a cell as all the cells that surround it. Thus, each cell has eight neighbours, except the ones on the left and right columns on the grid, which can have five or three (corners) neighbours. We pick one of these neighbours at random and then apply the state change rule, which is defined as follows. If the neighbour cell picked is an A cell, we will proceed to exchange the states of the vacancy and A cell, and so A has moved. If the neighbour cell picked is a B cell, the probability of exchanging states with the vacancy cell is defined to be $1/\Gamma$. This will capture the physical feature

in the model of B being Γ times slower than A. Finally, if the neighbour cell picked is a vacancy, no change of states is applied.

Our interest now is to find the continuum limit of the asynchronous cellular automaton model we have described. Let us define the fraction of V cells, A cells, and B cells in the whole grid as

$$\bar{V} = \frac{N_V}{N^2}, \qquad \bar{A} = \frac{N_A}{N^2}, \qquad \bar{B} = \frac{N_B}{N^2}, \tag{7.6}$$

where N_i is the number of cells of state i. Let us pick a square subgrid of size $\sqrt{N} \times \sqrt{N}$, and name it the (i, j) subgrid (see Figure 7.1). Inside it, we define the following three functions,

- $\bar{V}_{i,\,j}$, the fraction of V cells in the (i, j) subgrid;
- $\bar{A}_{i,\,j}$, the fraction of A cells in the (i, j) subgrid;
- $\bar{B}_{i,\,j}$, the fraction of B cells in the (i, j) subgrid.

All three functions above are dependent on space and time. Note that the choice of $M = \sqrt{N}$ of the subgrid is arbitrary. We only need $\lim_{N\to\infty} M/N = 0$ in a suitable manner.

We wish to study the evolution in one time step of the fraction number of V cells, A cells and B cells inside the (i, j) subgrid. Let $\bar{A}^n_{i,\,j}$, $\bar{V}^n_{i,\,j}$, $\bar{B}^n_{i,\,j}$ be the fraction number of A cells, vacancies and B cells, respectively, in the (i, j) subgrid at time step n. The aim is to compute $\bar{A}^{n+1}_{i,\,j}$, $\bar{V}^{n+1}_{i,\,j}$ and $\bar{B}^{n+1}_{i,\,j}$. In the next two sections we will discuss the change of A cells and V cells in one time step inside the (i, j) subgrid, respectively. We will omit the case of B cells since by conservation it can be found from A and V.

7.3.1 A cells

There are two factors that can affect the amount of A cells in the (i, j) subgrid in one time step: either a vacancy of the subgrid is able to exchange places with an A cell of a neighbouring subgrid (that adds an A cell), or a vacancy from a neighbouring subgrid is able to exchange places with an A cell in the (i, j) subgrid (that removes an A cell). Thus, to add one A cell it is necessary that at the n-th time step

$\{1.1\}$ a vacancy V inside the (i, j) subgrid is picked;

$\{1.2\}$ said V is on one of the edges of the (i, j) subgrid;

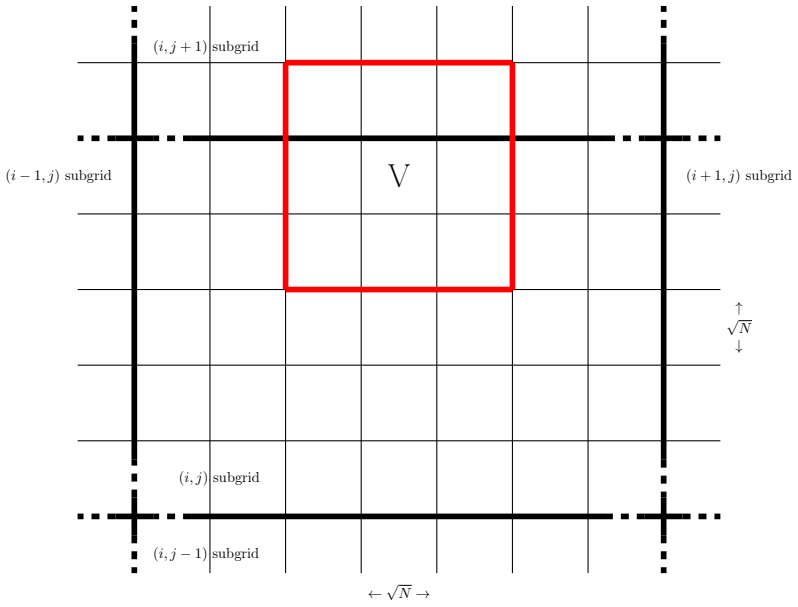

Figure 7.1: Sketch of the subgrid set-up. In red the local neighbourhood of a V cell is shown.

{1.3} the cell picked to do the exchange is an A cell and is in one of the neighbouring $(i+1, j)$, $(i-1, j)$, $(i, j+1)$, $(i, j-1)$ subgrids.

Similarly, to remove one A cell, it is necessary that at the n-th time step

{2.1} a vacancy V in one of the neighbouring $(i+1, j)$, $(i-1, j)$, $(i, j+1)$, $(i, j-1)$ subgrids is picked;

{2.2} said V is on one of the edges of the subgrid it is on (the one neighbouring the (i, j) subgrid);

{2.3} the cell picked to do the exchange is an A cell and is in the (i, j) subgrid.

The probabilites of the events mentioned above are obtained via standard probability theory under the assumption that A and V are uniformly distributed in the subdomain,

$$P(\{1.1\}) = \frac{N\bar{V}_{i,j}}{N^2\bar{V}}, \qquad P(\{1.2\}) = 4\frac{\sqrt{N}}{N}, \tag{7.7}$$

$$P(\{1.3\}) = \frac{1}{4}\left(\bar{A}_{i+1,j} + \bar{A}_{i-1,j} + \bar{A}_{i,j+1} + \bar{A}_{i,j-1}\right), \tag{7.8}$$

and

$$P(\{2.1\}) = \frac{N}{N^2\bar{V}}\left(\bar{V}_{i-1,j} + \bar{V}_{i+1,j} + \bar{V}_{i,j-1} + \bar{V}_{i,j+1}\right), \tag{7.9}$$

$$P(\{2.2\}) = \frac{\sqrt{N}}{N}, \qquad P(\{2.3\}) = \bar{A}_{i,j}. \tag{7.10}$$

Now, the fraction of A cells at the next time step $\bar{A}_{i,j}^{n+1}$ is just the fraction of A cells at the current time step $\bar{A}_{i,j}^{n}$ plus the probability of adding an A cell into the subgrid, P($\{1.1\}$) $\times$ P($\{1.2\}$) $\times$ P($\{1.3\}$), minus the probability of removing an A cell into the subgrid, P($\{2.1\}$) $\times$ P($\{2.2\}$) $\times$ P($\{2.3\}$),

$$\begin{aligned}\bar{A}_{i,j}^{n+1} =& \bar{A}_{i,j}^{n} + \frac{1}{N}\left(\frac{N\bar{V}_{i,j}^{n}}{N^2\bar{V}}\right)\left(4\frac{\sqrt{N}}{N}\right)\frac{1}{4}\left(\bar{A}_{i+1,j}^{n} + \bar{A}_{i-1,j}^{n} + \bar{A}_{i,j+1}^{n} + \bar{A}_{i,j-1}^{n}\right) \\ &- \frac{1}{N}\left(\frac{N}{N^2\bar{V}}\left(\bar{V}_{i-1,j}^{n} + \bar{V}_{i+1,j}^{n} + \bar{V}_{i,j-1}^{n} + \bar{V}_{i,j+1}^{n}\right)\right)\left(\frac{\sqrt{N}}{N}\right)\bar{A}_{i,j}^{n}.\end{aligned} \tag{7.11}$$

7.3.2 V cells

As in the previous case, there are two things can affect the amount of V cells in the (i,j) subgrid: either an A or B cell in the (i,j) subgrid is able to exchange places with a V cell in one of the neighbouring subgrids (that adds a V cell), or a vacancy from the (i,j) subgrid is able to exchange places with an A or B cell in one of the neighbouring subgrids (that removes a V cell). To add one vacancy, it is necessary that at the n-th time step

- $\{3.1\}$ a vacancy V in one of the neighbouring $(i+1,j)$, $(i-1,j)$, $(i,j+1)$, $(i,j-1)$ subgrids is picked;
- $\{3.2\}$ said V is on one of the edges of the subgrid it is on (the one neighbouring the (i,j) subgrid);
- $\{3.3\}$ the cell picked to do the exchange is on the (i,j) subgrid and an exchange actually occurs. Recall that if the exchange is with an A cell the probability of movement is 1 whereas if the exchange is with a B cell said probability is $1/\Gamma$.

Similarly, to remove a vacancy, it is necessary that at the n-th time step

- $\{4.1\}$ a vacancy V inside the (i,j) subgrid is picked;
- $\{4.2\}$ said V is on one of the edges of the (i,j) subgrid;
- $\{4.3\}$ the cell picked to do the exchange is on one of the neighbouring $(i+1,j)$, $(i-1,j)$, $(i,j+1)$, $(i,j-1)$ subgrids and an exchange actually occurs.

It is assumed that the vacancy concentration is low enough so that the probability of picking a vacancy to do the exchange is negligible. Consequently we only define the probabilities

$$P(\{3.3\}) = 1 - \bar{B}_{i,j}\frac{\Gamma - 1}{\Gamma}, \tag{7.12}$$

$$P(\{4.3\}) = 1 - \frac{1}{4}(\bar{B}_{i+1,\,j} + \bar{B}_{i-1,\,j} + \bar{B}_{i,\,j+1} + \bar{B}_{i,\,j+1})\frac{\Gamma - 1}{\Gamma}. \tag{7.13}$$

This allows us to write

$$\begin{aligned}\bar{V}_{i,\,j}^{n+1} =& \bar{V}_{i,\,j} + \frac{1}{N}\left(\frac{N}{N^2\bar{V}}\left(\bar{V}_{i-1,\,j}^{n} + \bar{V}_{i+1,\,j}^{n} + \bar{V}_{i,\,j-1}^{n} + \bar{V}_{i,\,j+1}^{n}\right)\right)\left(\frac{\sqrt{N}}{N}\right)\left(1 - \bar{B}_{i,j}^{n}\frac{\Gamma - 1}{\Gamma}\right) \\ &- \frac{1}{N}\left(\frac{N\bar{V}_{i,\,j}^{n}}{N^2\bar{V}}\right)\left(4\frac{\sqrt{N}}{N}\right)\left(1 - \frac{1}{4}(\bar{B}_{i+1,\,j}^{n} + \bar{B}_{i-1,\,j}^{n} + \bar{B}_{i,\,j+1}^{n} + \bar{B}_{i,\,j+1}^{n})\frac{\Gamma - 1}{\Gamma}\right).\end{aligned} \tag{7.14}$$

7.3.3 Limit $N \to \infty$

The objective of the present section is to determine whether in the limit $N \to \infty$ the CA model of the previous section reduces to the diffusion model in equations (7.1)-(7.2). Rearranging equation (7.11) leads to

$$\begin{aligned}\bar{A}_{i,\,j}^{n+1} =& \bar{A}_{i,\,j}^{n} + \frac{\sqrt{N}}{N^2\bar{V}}\left(\frac{\bar{V}_{i,\,j}^{n}\left(\bar{A}_{i-1,\,j}^{n} + \bar{A}_{i+1,\,j}^{n} + \bar{A}_{i,\,j-1}^{n} + \bar{A}_{i,\,j+1}^{n}\right)}{N}\right. \\ &\left. - \frac{\left(\bar{V}_{i-1,\,j}^{n} + \bar{V}_{i+1,\,j}^{n} + \bar{V}_{i,\,j-1}^{n} + \bar{V}_{i,\,j+1}^{n}\right)\bar{A}_{i,\,j}^{n}}{N}\right).\end{aligned} \tag{7.15}$$

We may equate this to a standard finite difference form by choosing $\sqrt{N} = \Delta x$ and $\Delta\hat{t} = \frac{1}{N^{3/2}\bar{V}}$,

$$\begin{aligned}\frac{\bar{A}_{i,\,j}^{n+1} - \bar{A}_{i,\,j}^{n}}{\Delta\hat{t}} =& \left(\frac{\bar{V}_{i,\,j}^{n}\left(\bar{A}_{i-1,\,j}^{n} + \bar{A}_{i+1,\,j}^{n} + \bar{A}_{i,\,j-1}^{n} + \bar{A}_{i,\,j+1}^{n}\right)}{\Delta x^2}\right. \\ &\left. - \frac{\left(\bar{V}_{i-1,\,j}^{n} + \bar{V}_{i+1,\,j}^{n} + \bar{V}_{i,\,j-1}^{n} + \bar{V}_{i,\,j+1}^{n}\right)\bar{A}_{i,\,j}^{n}}{\Delta x^2}\right).\end{aligned} \tag{7.16}$$

Note that $\Delta\hat{t}$ is not a time, rather we are just conforming to finite difference notation.

Similarly, equation (7.14) may be expressed as

$$\begin{aligned}\frac{\bar{V}_{i,j}^{n+1}-\bar{V}_{i,j}^{n}}{\Delta\hat{t}} =& \frac{\left(\bar{V}_{i-1,j}^{n}+\bar{V}_{i+1,j}^{n}+\bar{V}_{i,j-1}^{n}+\bar{V}_{i,j+1}^{n}\right)\left(1-\bar{B}_{i,j}^{n}\frac{\Gamma-1}{\Gamma}\right)}{\Delta x^2} \\ &- \frac{\bar{V}_{i,j}^{n}\left(4-(\bar{B}_{i+1,j}^{n}+\bar{B}_{i-1,j}^{n}+\bar{B}_{i,j+1}^{n}+\bar{B}_{i,j+1}^{n})\frac{\Gamma-1}{\Gamma}\right)}{\Delta x^2}.\end{aligned} \tag{7.17}$$

Taking the limit $N \to \infty$ in equations (7.16) and (7.17), changing the notation to $A_{i,j} \equiv X_A$, $B_{i,j} \equiv X_B$, $V_{i,j} \equiv X_V$, and substituting $X_B = 1 - X_A - X_V$ gives

$$\frac{\partial X_A}{\partial \hat{t}} = X_V \nabla^2 X_A - X_A \nabla^2 X_V, \tag{7.18}$$

$$\Gamma \frac{\partial X_V}{\partial \hat{t}} = -(\Gamma-1) X_V \nabla^2 X_A + (1+(\Gamma-1)X_A)\,\nabla^2 X_V. \tag{7.19}$$

Finally, setting $t = \hat{t}/\Gamma$, we recover equations (7.1)-(7.2) and the CA model does indeed reduce to the continuous diffusion model.

7.4 Results

In this section we present the results of the CA model. For the simulations we pick a square grid $N \times N$, where $N = 200$. At the first time step, the first 100 columns are A cells, and the remaining 100 columns are B cells. Then we randomly distribute 2000 vacancies (equivalent to 5% of the total number of cells) throughout the whole grid. A simulation is then run for 1.85×10^9 steps which is sufficient to allow for significant change in the distribution of cells.

Figures 7.2(a), 7.2(c), 7.2(e) show the distribution of material and vacancies when $\Gamma = 1.5$, that is, the diffusion rates between A and B are similar. Throughout the process vacancies are well distributed in the domain and, by the time $t = t_3$, the system appears close to equilibrium. Figures 7.2(b), 7.2(d), 7.2(f) show the corresponding evolution when A diffuses much faster than B. In Figure 7.2(b) we see a greater motion of A to the right than the one observed in Figure 7.2(a). However this also means that vacancies accumulate on the left. In Figure 7.2(d) it is clear that the vacancy concentration on the right is low, which acts to slow down the diffusion. This is clear from the final figure, Figure 7.2(f), which is far from equilibrium. This may seem counter-intuitive; A diffuses much faster here than in Figure 7.2(e) but it clearly ends up moving slower. This is a result of the initial rapid movement of A, bringing a high proportion of vacancies to the left and so hindering

further movement. A similar result was noticed in the continuum model of [88], where a very fast diffuser ends up redistributing more slowly.

In Figure 7.4 we compare the concentration of vacancies given by the CA model and that given by the continuum model in equations (7.1)-(7.2) at different times for two values of ratio between the diffusion rates; $\Gamma = 1.5$ (Figure 7.4(a) and 7.4(b)) and $\Gamma = 10$ (Figure 7.4(c) and 7.4(d)). The numerical solution of (7.1)-(7.2) is standard and defined in [88]. The CA results come from an average of simulations. To achieve this we define

$$V_j^n = \frac{\bar{V}}{I} \sum_{i=1}^{I} \left\{ N_V^i \right\}_j^n \tag{7.20}$$

where $\left\{ N_V^i \right\}_j^n$ is the number of vacancies at the j-th column on the n-th time step, the superscript i is used to distinguish different simulations, and I is the total number of CA simulations. The variable V_j^n denotes the average concentration of vacancies at the j-th column on the n-th time step. The results shown in Figure 7.4 correspond to $I = 10$.

To be able to compare the variable V_j^n and the numerical solution X_V of (7.1)-(7.2) we need to find a correspondence between the discrete time in the CA simulation and the continuous time in the PDE system. Let n be the time step that needs to be transformed to a continuum time t_n. Then

$$t_n = n \frac{\Delta \hat{t}}{\Gamma} t_s^{-1}, \tag{7.21}$$

where t_s is the time scale defined in [88]. It is defined as $t_s = \lambda a^2 \Gamma_B / (\epsilon l^2)$, where $\epsilon = 2X_{V,\text{ini}}$, λ is a geometric factor, a is the lattice constant and Γ_B is the hop frequency of species B. Finally, l is the length of the one-dimensional bar and it is found via the lattice site density ρ and the number of cells in our CA grid,

$$l = \left(\frac{N^3}{\rho} \right)^{1/3}, \tag{7.22}$$

which gives $l = 51$ nm for the case presented in Figure 7.4. Using the parameters values shown in [88, Table 1], we find that $t_s \approx 1.05 \times 10^8$. There is only one issue remaining to be treated before being able to compare the two solutions. When solving the continuum model, the initial condition for vacancies is given by [88]

$$X_{V,1}(x,0) = \frac{1 + (\Gamma - 1) X_A(x,0)}{2 + (\Gamma - 1) X_{A,\text{ini}}}, \tag{7.23}$$

where $X_{V,1} = X_V/\epsilon$. We do this rescaling to be able to keep track of the evolution of vacancies since this number is usually very small compared to the concentration of species A and B; numerically, this may cause problems. The initial condition for the CA model corresponds to $X_{V,1}(x,0) \approx 0.5$. This merely means that if n_0 is the initial time step in the CA model, the actual n_{t_0} that corresponds to the initial time t_0 is $n_{t_0} = rn_0$, where $r > 1$ (see Figure 7.3). To find this rescaling factor r we minimise the least-squares error between the continuum model and the discrete set of data $V_j^{n_f}$ at $n_f = 1.85 \times 10^9$. For $\Gamma = 10$, we find that $r = 26.171$; for $\Gamma = 1.5$, $r = 21.528$. The comparison of V_j^n, for $j = 1, \ldots, N$ and $X_{V,1}(t,x)$, with $x \in [-1, 1]$, is now well defined.

In Figure 7.4 we compare results for the vacancy concentration from the continuum model of equations (7.1)-(7.2) and the average result of 10 simulations via equation (7.20). First, we note what was observed in the previous figures, when $\Gamma = 1.5$ the vacancy concentration is relatively constant. When $\Gamma = 10$ vacancies concentrate on the left, thus slowing the movement of the fast diffuser. All figures show good agreement, even when $\Gamma = 1.5$. The most noticeable discrepancies occur at small times, near the ends $x = \pm 1$, where the continuum model indicates greater movement from the initial condition ($X_V = 0.5$). This is not surprising, continuum diffusion models typically allow for motion throughout the domain even though in reality extreme points may not be feeling any effect. Hence we expect that for small times the CA model is more realistic, and the agreement improves with time.

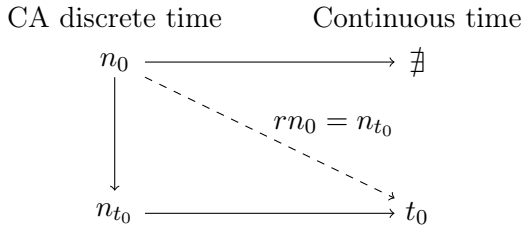

Figure 7.3: Time conversion sketch.

7.5 Conclusions

The goal of this paper was to develop a cellular automaton model to describe binary diffusion in solids. To do this we chose to employ an asynchronous model and used basic rule definitions to update the cell states, based on the physics that drive the process.

In the limit of large number of cells we showed that this CA model reduces to a particular

form of the continuum model developed in [88]. This was verified in the Results section by comparing the CA and the continuum model. This opens the possibility of designing various scenarios in a very simple fashion and then just take the limit to obtain the continuum model to do a more accurate analysis.

An interesting result to come out of this work is that when the system has a very fast diffuser it can lead, overall, to a slower diffusion process. This occurs because the initial fast diffusion acts to move nearly all vacancies to one side, so restricting further vacancy exchange and so movement. Also, at small times the nature of the continuum model permitted movement throughout the domain when in practice this may not occur. The CA model showed less movement near the extreme points at small times. This seems more physically realistic, hence in this case the CA model may be preferable.

Obviously the CA model becomes increasingly cumbersome as the number of cells increases. For sufficiently large numbers a continuum model is clearly preferable. However, when the number of cells is small, for example when modelling nanoscale diffusion, CA models provide a powerful tool which may be more accurate than the continuum models.

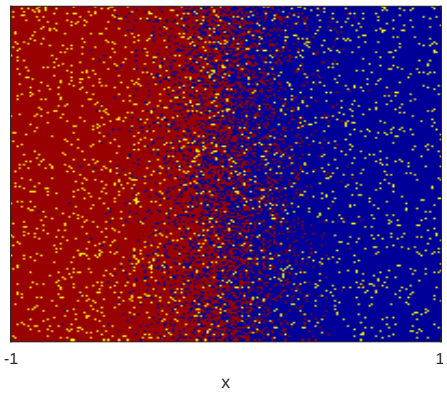

(a) $\Gamma = 1.5$, $t = t_1$.

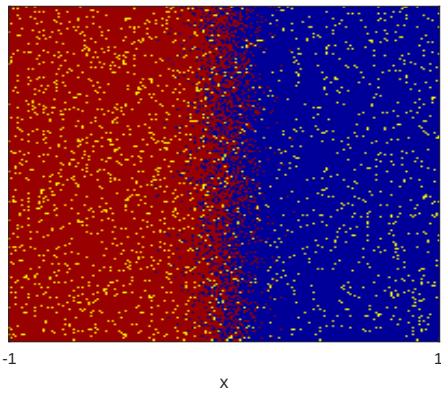

(b) $\Gamma = 10$, $t = t_1$.

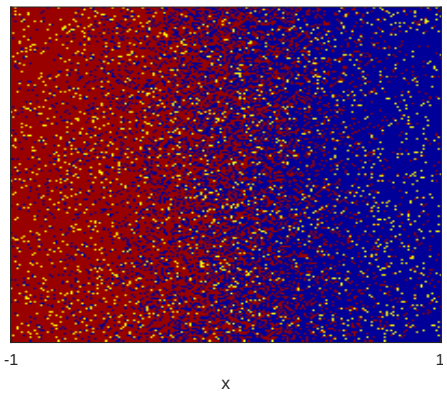

(c) $\Gamma = 1.5$, $t = t_2$.

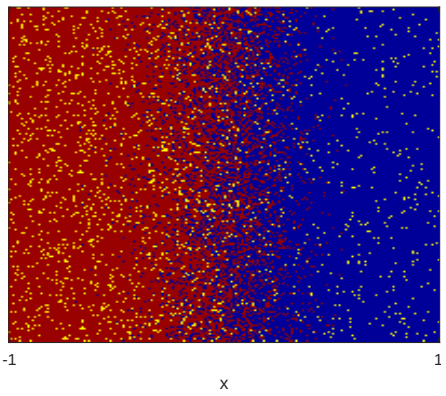

(d) $\Gamma = 10$, $t = t_2$.

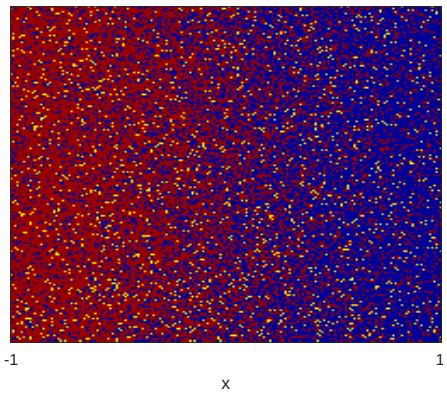

(e) $\Gamma = 1.5$, $t = t_3$.

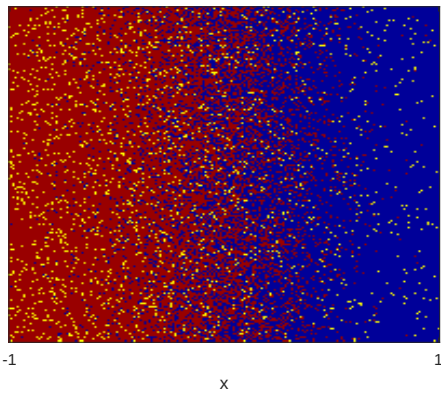

(f) $\Gamma = 10$, $t = t_3$.

Figure 7.2: Resulting grid 200×200 for different times obtained with the simulation of the CA model. Red denotes A atom cells. Blue denotes B atom cells. Yellow denotes vacancy cells. $t_1 < t_2 < t_3$.

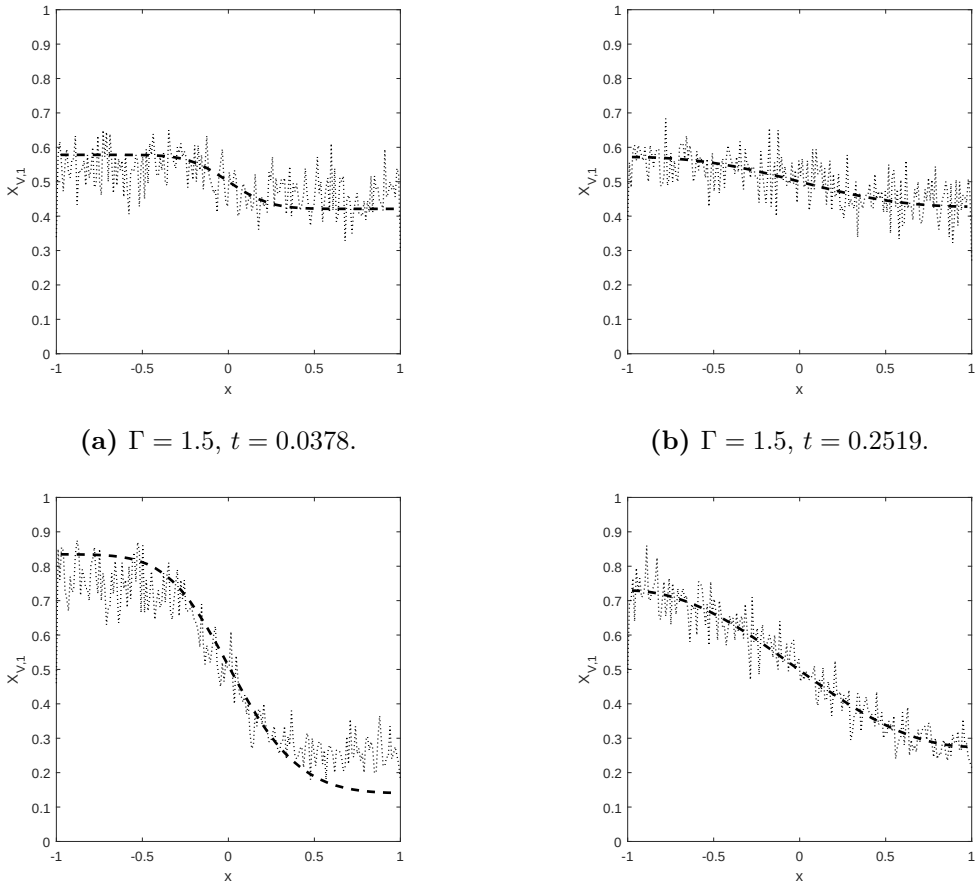

(a) $\Gamma = 1.5$, $t = 0.0378$.

(b) $\Gamma = 1.5$, $t = 0.2519$.

(c) $\Gamma = 10$, $t = 0.0574$.

(d) $\Gamma = 10$, $t = 0.3263$.

Figure 7.4: Dotted line is obtained by joining the discrete normalised vacancy average concentration V_j^n obtained via the CA model (equation (7.20)). Solid line represents the numerical solution of the continuum model described by equations (7.1)-(7.2).

8 | Conclusions

The goal of this thesis was to study and understand two diffusion processes at the nanoscale. In the first half, we focussed on the phase-change problem; in the second, we studied binary diffusion in solids, and in particular, the Kirkendall effect. The motivation for understanding these processes was to gain insight into the physical phenomena and thus be able to optimise the function of nanoparticles for particular industrial processes, in which the size and/or matter distribution of the particles affects their function.

In Chapter 3 we focussed on improving the accuracy of the HBIM applied to Stefan problems in both spherical and cylindrical geometries. This was done by analysing the standard form and the optimised form (TIM) in the original and transformed coordinate system, and we studied a fixed temperature and a Newton cooling boundary condition. The approximate solution via the perturbation method was also obtained, assuming a large Stefan number. The accuracy of the TIM and perturbation solution was judged by comparison of the predicted melt front position calculated by a numerical solution. We found that in spherical coordinates, if the melting is driven by a fixed boundary condition, the TIM yields accurate results if one first transforms the coordinate system. Consequently, when studying the spherical Stefan problem we recommend first transforming the temperature $T = u/r$, then with a fixed boundary boundary condition setting $n = 1.6$, and with a Newton cooling condition, $n = 1.79$. Note, in fact for Newton cooling the optimal exponent depends on Nu. However in Chapter 5 it was shown that this average value provides accurate results. For the cylindrical system we cannot make a conclusive statement. Due to having to use a boundary fixing transformation instead of a temperature transformation, the governing equations became complicated thus making the TIM too complex to be of practical use or appeal. When the Stefan number $\beta = 1$, we found that for the fixed temperature boundary

condition the TIM gives the best result in the original system. For the Newton cooling condition, the TIM gives the best result in the transformed system. For larger β, we should use a perturbation method. It is possible that a different transformation, on either the temperature or coordinates, could change this conclusion. However, it does not seem like a trivial task to solve immediately.

In Chapter 4 we described the first model for the melting of a spherically symmetric nanoparticle to include latent heat depression, to employ the new Stefan condition developed in [70], and to use a Newton cooling condition. All these novel features proved to have important consequences. With the aim of capturing latent heat depression, in §4.2 we proposed an exponential model to describe published data on the latent heat variation of tin. This contained a single fitting parameter, and provided much better agreement with the data than previous models in the literature. We also used a new Stefan condition. However, since latent heat is the dominant term for most of the process it is the latent heat variation that appears to be the most important between these two novel features. Using a fixed boundary condition is equivalent to imposing an infinite heat transfer coefficient, which will lead to faster melting rates than in reality. We proposed a Newton cooling condition instead, which leads to slower melt rates, which then has an impact on the kinetic energy contribution. Previous work in which a fixed temperature boundary condition was used concluded that the density change between phases was very important precisely because of the large resulting kinetic energy. The effect was so strong that it carried through even to the macroscale. Our work indicated a much smaller influence of the kinetic energy. To permit comparison with fixed temperature results from the literature for our study we used the maximum heat flux that the system allowed without vaporising the particle. In practice one would use a much smaller value and so, in general, kinetic energy would be even less important than in our calculations. Consequently, our study indicated that, provided the density difference is not large, and the boundary condition is physically realistic then the contribution of kinetic energy to the Stefan condition may be neglected. This will then considerably simplify the formulation, allowing the removal of the cubic velocity term.

The idea in Chapter 5 was to link the work of the previous two chapters. To do so, we presented a reduced form of the model of Chapter 4 in which the density in the different phases is the same and in which we neglected the solid phase by setting it to the phase change

temperature. We studied the problem for two boundary conditions: the more popular fixed temperature condition, and the more realistic Newton cooling condition. Our goal was to use the TIM method developed in Chapter 3 to solve the problem. In order to obtain the best approximating solution, we transformed the temperature via $u = rT$, since we showed in Chapter 3 that this led to more accurate results. To measure the performance of the method we compared the melt front position with a numerical solution. Further, we presented a perturbation solution in order to highlight the accuracy of the method when compared to the standard choice of approximate solution. Chapter 3 involved a standard Stefan problem in a spherical geometry. In Chapter 4 the case of a melting nanosphere was examined. This altered the previous formulation to include size-dependent paramters. Even so the conclusions of Chapter 3 still held: the TIM was always more accurate than the first order perturbation when setting $n = 1.6$ for the fixed temperature boundary condition and $n = 1.79$ for Newton cooling. Given that the effort in applying the TIM is comparable to that of the perturbation method it seems clear that the form of TIM developed in Chapter 3 should be preferred over the perturbation method.

The second part of the thesis was focussed on binary diffusion in solids. In Chapter 6 we derived governing equations for substitutional binary diffusion. To gain better insight into the physics behind the Kirkendall effect we focussed on a one-dimensional insulated bar. One of the more relevant results was finding two time-scales for the process: an initial fast time-scale where vacancies rapidly redistribute, followed by a slow redistribution to the constant steady-state. The expressions for the diffusion coefficients were cumbersome, making the governing equations highly nonlinear. Some limiting cases for the ratio between the diffusion rates Γ led to a simplification of the governing equations. For the limiting case $\Gamma \gg 1$ we were able to obtain analytical solutions to the problem via separation of variables. The simplification was also based on the volume fraction of fast diffuser not being close to zero. In general results were excellent, except for at small times, near the boundary where initially the volume fraction is zero. However, these errors decreased with time. For $\Gamma \sim 1$ analytical progress was made by slightly modifying two of the diffusion coefficients to give a system that could again be solved using separation of variables. Despite the fact that the error in diffusion coefficients could be close to 20% the errors arising from this modification were small. In summary, in this chapter we developed a novel model for substitutional

binary diffusion which may be readily applied to other geometries or with different boundary conditions, opening the doors to model the creation of hollow nanostructures.

In Chapter 7 we approached the same problem as in the previous chapter but from the cellular automata standpoint. We defined an asynchronous model with a simple state change rule to update the state of cells. This state change rule is defined based on the physics that drive the process. Since the fast diffuser is more likely to move, we assign a much higher probability to change state to those cells than those of the slow diffuser. Furthermore, we showed that the continuum limit of the cellular automata model we constructed leads to the same governing equations as in some particular cases presented in the previous chapter. We compared the results of our CA model to the numerical solution of the continuum equations, obtaining excellent agreement between both solutions. With this, we showed the possibility of describing various scenarios in binary diffusion in solids in a very simple fashion. Since the computational effort increases greatly with the number of cells this approach is ideal for small scale structures, such as nanoparticles. It could then provide an excellent novel approach to describe nanoscale diffusion and so help in the design of hollow structures at the nanoscale.

Bibliography

[1] F. Ahmad, A. K. Pandey, A. B. Herzog, J. B. Rose, C. P. Gerba, and S. A. Hashsham. Environmental applications and potential health implications of quantum dots. *Journal of Nanoparticle Research*, 14(8):1038, 2012.

[2] F. Aldinger. Controlled porosity by an extreme kirkendall effect. *Acta Metallurgica*, 22(7):923–928, 1974.

[3] V. Alexiades and A. D. Solomon. *Mathematical Modeling Of Melting And Freezing Processes*. Hemisphere, Washington DC, 1992.

[4] K. An and T. Hyeon. Synthesis and biomedical applications of hollow nanostructures. *Nano Today*, 4(4):359–373, 2009.

[5] T. Bachels, H.-J. Güntherodt, and R. Schäfer. Melting of isolated tin nanoparticles. *Physical Review Letters*, 85(6):1250–1253, 2000.

[6] J. Back, S. McCue, and M. Hsieh. The effect of surface tension and kinetic undercooling on a radially-symmetric melting problem. *Applied Mathematics and*, 2014.

[7] J. Back, S. McCue, and T. Moroney. Including nonequilibrium interface kinetics in a continuum model for melting nanoscaled particles. *Scientific reports*, 2014.

[8] J. M. Back. *Stefan problems for melting nanoscaled particles*. PhD thesis, University of Queensland, 2014.

[9] G. E. Bell. A refinement of the heat balance integral method applied to a melting problem. *International Journal of Heat and Mass Transfer*, 21(11):1357–1362, nov 1978.

[10] R. B. Bird, W. E. Stewart, and E. N. Lightfoot. *Transport Phenomena*. John Wiley & Sons Inc., New York, 1960.

[11] J. P. Boon, D. Dab, R. Kapral, and A. Lawniczak. Lattice gas automata for reactive systems. *Physics Reports*, 273(2):55–147, 1996.

[12] M. Bruchez, M. Moronne, P. Gin, and S. Weiss. Semiconductor nanocrystals as fluorescent biological labels. *Science*, 281(5385):2013–2016, 1998.

[13] P. Buffat and J.-P. Borel. Size effect on the melting temperature of gold particles. *Physical Review A*, 13(6):2287–2298, 1976.

[14] J. Caldwell and C.-C. Chan. Numerical solutions of the Stefan problem by the enthalpy method and the Heat Balance Integral Method. *Numerical Heat Transfer, Part B: Fundamentals*, 33(1):99–117, jan 1998.

[15] J. Caldwell and C.-C. Chan. Spherical solidification by the enthalpy method and the heat balance integral method. *Applied Mathematical Modelling*, 24(1):45–53, jan 2000.

[16] J. Caldwell and C. K. Chiu. Numerical solution of one-phase Stefan problems by the heat balance integral method, Part I - cylindrical and spherical geometries. *Communications in Numerical Methods in Engineering*, 16(8):569–583, aug 2000.

[17] X. Chen, C. Li, M. Grätzel, and R. Kostecki. Nanomaterials for renewable energy production and storage. *Chemical Society Reviews*, 2012.

[18] H. Ching-Lun and Y.-P. Shih. Perturbation solutions of planar diffusion-controlled moving-boundary problems. *International Journal of Heat and Mass Transfer*, 18(5):689–695, 1975.

[19] B. Chopard, M. Droz, and M. Kolb. Cellular automata approach to non-equilibrium diffusion and gradient percolation. *Journal of Physics A: Mathematical and General*, 22(10):1609–1619, 1989.

[20] T. B. David, Y. Lereah, G. Deutscher, R. Kofman, and P. Cheyssac. Solid-liquid transition in ultra-fine lead particles. *Philosophical Magazine A*, 71(5):1135–1143, 1995.

[21] S. H. Davis. *Theory of Solidification*. Cambridge University Press, Cambridge, 2001.

[22] F. Delogu. Structural and energetic properties of unsupported Cu nanoparticles from room temperature to the melting point: Molecular dynamics simulations. *Physical Review B*, 72(20):205418, 2005.

[23] J. A. Dieringer, A. D. McFarland, N. C. Shah, D. A. Stuart, A. V. Whitney, C. R. Yonzon, M. A. Young, X. Zhang, and R. P. Van Duyne. Introductory Lecture: Surface enhanced Raman spectroscopy: New materials, concepts, characterization tools, and applications. *Faraday Discuss.*, 132:9–26, 2006.

[24] F. I. Dragomirescu, K. Eisenschmidt, C. Rohde, and B. Weigand. Perturbation solutions for the finite radially symmetric Stefan problem. *International Journal of Thermal Sciences*, 104:386–395, jun 2016.

[25] F. Ercolessi, W. Andreoni, and E. Tosatti. Melting of small gold particles: Mechanism and size effects. *Physical Review Letters*, 66(7):911–914, 1991.

[26] H. J. Fan, M. Knez, R. Scholz, D. Messet, K. Nielsch, M. Zacharias, and U. Gosele. Influence of surface diffusion on the formation of hollow nanostructures induced by the Kirkendall effect: The basic concept. *Nano Letters*, 7(4):993–997, 2007.

[27] A. Fedorov and A. Shulgin. Mathematical modeling of melting of nano-sized metal particles. *Combustion, Explosion, and Shock Waves*, 2011.

[28] B. Florio and T. Myers. The melting and solidification of nanowires. *Journal of Nanoparticle Research*, 2016.

[29] F. Font, S. L. Mitchell, and T. G. Myers. One-dimensional solidification of supercooled melts. *International Journal of Heat and Mass Transfer*, 62:411–421, jul 2013.

[30] F. Font and T. G. Myers. Spherically symmetric nanoparticle melting with a variable phase change temperature. *Journal of Nanoparticle Research*, 15(12):2086, 2013.

[31] F. Font, T. G. Myers, and S. L. Mitchell. A mathematical model for nanoparticle melting with density change. *Microfluidics and Nanofluidics*, 18(2):233–243, 2014.

[32] A. C. Fowler. *Mathematical models in the applied sciences.* Cambridge University Press, 1997.

[33] J. Gao, B. Zhang, X. Zhang, and B. Xu. Magnetic-dipolar-interaction-induced self-assembly affords wires of hollow nanocrystals of cobalt selenide. *Angewandte Chemie*, 118(8):1242–1245, 2006.

[34] S. Garg, R. Bansal, and C. Ghosh. *Thermal Physics.* Tata McGraw-Hill Education, 1993.

[35] M. Garinot, V. Fiévez, V. Pourcelle, F. Stoffelbach, A. des Rieux, L. Plapied, I. Theate, H. Freichels, C. Jérôme, J. Marchand-Brynaert, Y.-J. Schneider, and V. Préat. PEGylated PLGA-based nanoparticles targeting M cells for oral vaccination. *Journal of Controlled Release*, 120(3):195–204, 2007.

[36] P. Ghosh, G. Han, M. De, C. K. Kim, and V. M. Rotello. Gold nanoparticles in delivery applications. *Advanced drug delivery reviews*, 60(11):1307–15, 2008.

[37] E. González, J. Arbiol, and V. F. Puntes. Carving at the nanoscale: sequential galvanic exchange and Kirkendall growth at room temperature. *Science (New York, N.Y.)*, 334(6061):1377–80, 2011.

[38] T. R. Goodman. The heat-balance integral and its application to problems involving a change of phase. *Transactions of the ASME*, 80(2):335–342, 1958.

[39] F. Gröhn, G. Kim, B. J. Bauer, and E. J. Amis. Nanoparticle formation within dendrimer-containing polymer networks: Route to new organic-inorganic hybrid materials. *Macromolecules*, 34(7):2179–2185, 2001.

[40] J. M. Hill. *One-dimensional Stefan problems: an introduction.* Longman Sc & Tech, 1987.

[41] J. Hristov. The heat-balance integral method by a parabolic profile with unspecified exponent: Analysis and Benchmark Exercises. *arXiv preprint arXiv:1012.2533*, dec 2010.

[42] C.-L. Huang and Y.-P. Shih. A perturbation method for spherical and cylindrical solidification. *Chemical Engineering Science*, 30(8):897–906, aug 1975.

[43] H. Huntington and F. Seitz. Mechanism for self-diffusion in metallic copper. *Physical Review*, 61(5-6):315–325, 1942.

[44] S. Jana, J. W. Chang, and R. M. Rioux. Synthesis and modeling of hollow intermetallic Ni-Zn nanoparticles formed by the Kirkendall effect. *Nano Letters*, 13(8):3618–3625, 2013.

[45] K. Janssens, D. Raabe, E. Kozeschnik, and M. Miodownik. *Computational materials engineering: an introduction to microstructure evolution*. 2010.

[46] H. Jiang, K.-s. Moon, H. Dong, F. Hua, and C. Wong. Size-dependent melting properties of tin nanoparticles. *Chemical Physics Letters*, 429(4-6):492–496, 2006.

[47] D. Jou, J. Casas-Vázquez, and G. Lebon. Extended irreversible thermodynamics. *Irreversible Thermodynamics*, 1996.

[48] S. Kim, M. Kim, W. Lee, and T. Hyeon. Fabrication of hollow palladium spheres and their successful application to the recyclable heterogeneous catalyst for Suzuki coupling reactions. *Journal of the American*, 124(26):7642–7643, 2002.

[49] A. Kumar and S. Roy. Melting of Steel Spherical Particle in Its Own Liquid: Application to Cladding. *Journal of Thermophysics and Heat Transfer*, 23(4):762–772, oct 2009.

[50] S. Lai, J. Guo, V. Petrova, G. Ramanath, and L. Allen. Size-dependent melting properties of small tin particles: nanocalorimetric measurements. *Physical Review Letters*, 77(1):99–102, 1996.

[51] Latent Heat of Melting of some common Materials. `http://www.engineeringtoolbox.com/latent-heat-melting-solids-d_96.html`. Accessed 19 Nov 2015.

[52] Y. Li, P. Zhou, Z. Dai, Z. Hu, P. Sun, and J. Bao. A facile synthesis of PdCo bimetallic hollow nanospheres and their application to Sonogashira reaction in aqueous media. *New Journal of Chemistry*, 30:832–837, 2006.

[53] H. S. Lim, C. K. Ong, and F. Ercolessi. Surface effects in vibrational and melting properties of Pb clusters. *Zeitschrift für Physik D Atoms, Molecules and Clusters*, 26(S1):45–47, 1993.

[54] X. Liu, P. Yang, and Q. Jiang. Size effect on melting temperature of nanostructured drugs. *Materials chemistry and physics*, 2007.

[55] X. W. D. Lou, L. A. Archer, and Z. Yang. Hollow micro-/nanostructures: Synthesis and applications. *Advanced Materials*, 20(21):3987–4019, 2008.

[56] M. M. MacDevette and T. G. Myers. Contact melting of a three-dimensional phase change material on a flat substrate. *International Journal of Heat and Mass Transfer*, 55(23-24):6798–6807, nov 2012.

[57] J. Manning. Diffusion in a chemical concentration gradient. *Physical Review*, 124(2):470, 1961.

[58] J. Manning. Diffusion and the Kirkendall shift in binary alloys. *Acta Metallurgica*, 15(5):817–826, 1967.

[59] J. Manning. Correlation factors for diffusion in nondilute alloys. *Physical Review B*, 4(4):1111, 1971.

[60] S. McCue, B. Wu, and J. Hill. Micro/nanoparticle melting with spherical symmetry and surface tension, 2009.

[61] S. L. Mitchell. An Accurate Nodal Heat Balance Integral Method with Spatial Subdivision. *Numerical Heat Transfer, Part B: Fundamentals*, 60(1):34–56, jul 2011.

[62] S. L. Mitchell and T. G. Myers. Approximate solution methods for one-dimensional solidification from an incoming fluid. *Applied Mathematics and Computation*, 202(1):311–326, 2008.

[63] S. L. Mitchell and T. G. Myers. Application of Standard and Refined Heat Balance Integral Methods to One-Dimensional Stefan Problems. *SIAM Review*, 52(1):57–86, jan 2010.

[64] S. L. Mitchell and T. G. Myers. Improving the accuracy of heat balance integral methods applied to thermal problems with time dependent boundary conditions. *International Journal of Heat and Mass Transfer*, 53(17-18):3540–3551, aug 2010.

[65] R. Molday and D. Mackenzie. Immunospecific ferromagnetic iron-dextran reagents for the labeling and magnetic separation of cells. *Journal of immunological methods*, 1982.

[66] L. K. Moleko, A. R. Allnatt, and E. L. Allnatt. A self-consistent theory of matter transport in a random lattice gas and some simulation results. *Philosophical Magazine A*, 59(1):141–160, 1989.

[67] S. Mornet, S. Vasseur, F. Grasset, and E. Duguet. Magnetic nanoparticle design for medical diagnosis and therapy. *Journal of Materials Chemistry*, 14(14):2161, 2004.

[68] F. Mosally, A. S. Wood, and A. Al-Fhaid. On the convergence of the heat balance integral method. *Applied Mathematical Modelling*, 29(10):903–912, oct 2005.

[69] T. Myers. Optimal exponent heat balance and refined integral methods applied to Stefan problems. *International Journal of Heat and Mass Transfer*, 2010.

[70] T. Myers. Mathematical modelling of phase change at the nanoscale. *International Communications in Heat and Mass Transfer*, 76:59–62, 2016.

[71] T. Myers and M. MacDevette. Continuum mathematics at the nanoscale. *Journal of Mathematics in ...*, 2014.

[72] T. Myers, S. Mitchell, and F. Font. Energy conservation in the one-phase supercooled Stefan problem. *International Communications in Heat and Mass Transfer*, 39(10):1522–1525, 2012.

[73] T. G. Myers. Optimizing the exponent in the heat balance and refined integral methods. *International Communications in Heat and Mass Transfer*, 36(2):143–147, feb 2009.

[74] T. G. Myers. Optimal exponent heat balance and refined integral methods applied to Stefan problems. *International Journal of Heat and Mass Transfer*, 53(5-6):1119–1127, feb 2010.

[75] T. G. Myers and F. Font. On the one-phase reduction of the Stefan problem with a variable phase change temperature. *International Communications in Heat and Mass Transfer*, 61:37–41, feb 2015.

[76] T. G. Myers and J. Low. An approximate mathematical model for solidification of a flowing liquid in a microchannel. *Microfluidics and Nanofluidics*, 11(4):417–428, oct 2011.

[77] T. G. Myers and J. Low. Modelling the solidification of a power-law fluid flowing through a narrow pipe. *International Journal of Thermal Sciences*, 70:127–131, aug 2013.

[78] T. G. Myers, M. M. MacDevette, and H. Ribera. A time-dependent model to determine the thermal conductivity of a nanofluid. *Journal of Nanoparticle Research*, 15(7):1775, 2013.

[79] T. G. Myers and S. L. Mitchell. Application of the combined integral method to Stefan problems. *Applied Mathematical Modelling*, 35(9):4281–4294, sep 2011.

[80] H. B. Na, I. C. Song, and T. Hyeon. Inorganic nanoparticles for MRI contrast agents. *Advanced Materials*, 21(21):2133–2148, 2009.

[81] L. Onsager. Reciprocal relations in irreversible processes. I. *Physical Review*, 37(4):405–426, 1931.

[82] L. B. Pfeil. The oxidation of iron and steel at high temperatures. *Journal of Iron and Steel Research*, 119:501–547, 1929.

[83] Y. Piao, J. Kim, H. B. Na, D. Kim, J. S. Baek, M. K. Ko, J. H. Lee, M. Shokouhimehr, and T. Hyeon. Wrap–bake–peel process for nanostructural transformation from β-FeOOH nanorods to biocompatible iron oxide nanocapsules. *Nature Materials*, 7(3):242–247, 2008.

[84] W. Qi. Size effect on melting temperature of nanosolids. *Physica B: Condensed Matter*, 368(1-4):46–50, nov 2005.

[85] S. Rana, A. Bajaj, R. Mout, and V. M. Rotello. Monolayer coated gold nanoparticles for delivery applications. *Advanced drug delivery reviews*, 64(2):200–16, 2012.

[86] H.-S. Ren. Application of the heat-balance integral to an inverse Stefan problem. *International Journal of Thermal Sciences*, 46(2):118–127, feb 2007.

[87] H. Ribera and T. G. Myers. A mathematical model for nanoparticle melting with size-dependent latent heat and melt temperature. *Microfluidics and Nanofluidics*, 20(11):147, 2016.

[88] H. Ribera, B. Wetton, and T. Myers. Mathematical model for substitutional binary diffusion in solids. *Submitted to Applied Mathematical Modelling*, 2017.

[89] W. C. Roberts-Austen. Bakerian Lecture: On the diffusion of metals. *Philosophical Transactions of the Royal Society of London. Series A, Containing Papers of a Mathematical or Physical Character*, 187:383–415, 1896.

[90] L. Rubinstein. *The Stefan Problem.* American Mathematical Society, 1971.

[91] N. Sadoun, E.-K. Si-Ahmed, and P. Colinet. On the refined integral method for the one-phase Stefan problem with time-dependent boundary conditions. *Applied Mathematical Modelling*, 30(6):531–544, jun 2006.

[92] S. Sahu, P. Das, and S. Bhattacharyya. A comprehensive analysis of conduction-controlled rewetting by the Heat Balance Integral Method. *International Journal of Heat and Mass Transfer*, 49(25-26):4978–4986, dec 2006.

[93] O. Salata. Applications of nanoparticles in biology and medicine. *Journal of nanobiotechnology*, 2(1):3, 2004.

[94] M. Shandiz, A. Safaei, S. Sanjabi, and Z. Barber. Modeling size dependence of melting temperature of metallic nanoparticles. *Journal of Physics and Chemistry of Solids*, 68(7):1396–1399, jul 2007.

[95] S. Sharafat and N. Ghoniem. Summary of thermo-physical properties of Sn, and compounds of Sn-H. *Sn-O, Sn-C, Sn-Li, and Sn-Si and Comparison of Properties of Sn, Sn-Li, and Pb-Li, Report: UCLA-UCMEP-00-31, University of California, Los Angeles*, 2000.

[96] A. Sharma, V. V. Tyagi, C. R. Chen, and D. Buddhi. Review on thermal energy storage with phase change materials and applications. *Renewable and Sustainable Energy Reviews*, 13(2):318–345, feb 2009.

[97] J.-H. Shim, B.-J. Lee, and Y. W. Cho. Thermal stability of unsupported gold nanoparticle: a molecular dynamics study. *Surface Science*, 512(3):262–268, 2002.

[98] J.-H. Shin and M. R. Deinert. A model for the latent heat of melting in free standing metal nanoparticles. *The Journal of Chemical Physics*, 140(16):164707, 2014.

[99] A. Smigelskas and E. Kirkendall. Diffusion of zinc in alpha brass. *Transactions of the Metallurgical Society of AIME*, 171:130–142, 1947.

[100] J. Stefan. Über die Theorie der Eisbildung, insbesondere über die Eisbildung im Polarmeere. *Annalen der Physik*, 1891.

[101] J. Sun and S. Simon. The melting behavior of aluminum nanoparticles. *Thermochimica Acta*, 463(1-2):32–40, 2007.

[102] K. Tanabe. Optical radiation efficiencies of metal nanoparticles for optoelectronic applications. *Materials Letters*, 61(23-24):4573–4575, 2007.

[103] Thermal Conductivity of Materials and Gases. `http://www.engineer-ingtoolbox.com/thermal-conductivity-d_429.html`. Accessed 19 Nov 2015.

[104] R. C. Tolman. The effect of droplet size on surface tension. *The Journal of Chemical Physics*, 17(3):333, 1949.

[105] E. Vázquez-Nava and C. J. Lawrence. Thermal Dissolution of a Spherical Particle with a Moving Boundary. *Heat Transfer Engineering*, 30(5):416–426, apr 2009.

[106] Z. Wang, L. Zhou, and X. W. D. Lou. Metal oxide hollow nanostructures for lithium-ion batteries. *Advanced Materials*, 24(14):1903–1911, 2012.

[107] J. R. Weimar. Cellular automata for reaction-diffusion systems. *Parallel Computing*, 23(11):1699–1715, 1997.

[108] A. S. Wood. A new look at the heat balance integral method. *Applied Mathematical Modelling*, 25(10):815–824, oct 2001.

[109] A. S. Wood, F. Mosally, and A. D. Al-Fhaid. On high-order polynomial Heat-Balance Integral implementations. *SCIENCE*, 161(2):536–354, 2009.

[110] B. Wu, S. W. McCue, P. Tillman, and J. M. Hill. Single phase limit for melting nanoparticles. *Applied Mathematical Modelling*, 33(5):2349–2367, may 2009.

[111] B. Wu, P. Tillman, S. W. McCue, and J. M. Hill. Nanoparticle melting as a Stefan moving boundary problem. *Journal of nanoscience and nanotechnology*, 2009.

[112] S. Xiong, W. Qi, Y. Cheng, B. Huang, M. Wang, and Y. Li. Universal relation for size dependent thermodynamic properties of metallic nanoparticles. *Physical Chemistry Chemical Physics*, 13(22):10652–60, 2011.

[113] S. H. Xu, G. T. Fei, Y. Zhang, X. F. Li, Z. Jin, and L. D. Zhang. Size-dependent melting behavior of indium nanowires. *Physics Letters A*, 375(16):1746–1750, apr 2011.

[114] T. C. Yih and M. Al-Fandi. Engineered nanoparticles as precise drug delivery systems. *Journal of cellular biochemistry*, 97(6):1184–90, 2006.

[115] Y. Yin, R. M. Rioux, C. K. Erdonmez, S. Hughes, G. A. Somorjai, and A. P. Alivisatos. Formation of hollow nanocrystals through the nanoscale Kirkendall effect. *Science (New York, N.Y.)*, 304(5671):711–4, 2004.

[116] H.-C. Yu, D.-H. Yeon, A. Van der Ven, and K. Thornton. Substitutional diffusion and Kirkendall effect in binary crystalline solids containing discrete vacancy sources and sinks. *Acta Materialia*, 55(20):6690–6704, 2007.

[117] M. Zhang, M. Efremov, F. Schiettekatte, E. Olson, A. Kwan, S. Lai, T. Wisleder, J. Greene, and L. Allen. Size-dependent melting point depression of nanostructures: Nanocalorimetric measurements. *Physical Review B*, 62(15):10548–10557, 2000.

[118] Y. Zhang, H. Zhang, J. Wu, and X. Wang. Enhanced thermal conductivity in copper matrix composites reinforced with titanium-coated diamond particles. *Scripta Materialia*, 65(12):1097–1100, 2011.